Computational Analysis of Circumferentially Grooved Seals Using Effective Film Thickness

---

A dissertation

presented to

the faculty of the Department of Mechanical & Aerospace Engineering

of the School of Engineering and Applied Science

University of Virginia

In partial fulfillment

of the requirements for the degree

Doctor of Philosophy (Mechanical and Aerospace Engineering)

by

Nathaniel P. Gibbons

May 2023

Approval Sheet

This dissertation is submitted in partial fulfillment of the requirements for the degree of

Doctor of Philosophy (Mechanical and Aerospace Engineering)

Nathaniel P. Gibbons

Nathaniel P. Gibbons

This dissertation has been read and approved by the Examining Committee:

Christopher Goyne

Christopher Goyne, Adviser (MAE)

Dan Quinn

Dan Quinn, Committee Chair (MAE)

Haibo Dong

Haibo Dong, (MAE)

Matthew Reidenbach

Matthew Reidenbach, (EVSC)

Neal Morgan

Neal Morgan, (MAE)

Accepted for the School of Engineering and Applied Science:

Jennifer L. West

Jennifer L. West, Dean, School of Engineering and Applied Science

May 2023

To my family

Acknowledgments

A special thank you to my advisor, Chris Goyne, for his continued mentorship, guidance, and support, especially through the transition and challenges of my final year.

Thank you to Cori Watson-Kassa for all of her assistance as my technical advisor and close collaborator and for helping make my ROMAC project possible. Thank you to Neal Morgan for his technical guidance and assistance in the final stages of my project, and for serving on my final defense committee.

To the remainder of my defense committee, Dan Quinn, Haibo Dong, and Matt Reidenbach, thank you for your willingness to serve on this committee and to devote time and energy to my progress as a graduate student.

To Lori Mohr Pedersen, thank you for sharing a few minutes of your mornings with me in the office and for being an invaluable resource for me, personally and professionally, during my time with ROMAC. You made each day a little brighter, and I cannot express how grateful I am for that.

I am lucky enough to be surrounded by people who help me find confidence when I need it the most and who encourage and allow me to be the best version of myself every day. To my family, thank you for your constant love and support. To my friends, from every phase of my life, thank you for helping me endure the lows and making sure I celebrate the highs. This graduate school journey truly takes a village, and I always knew that I had mine.

I would finally like to acknowledge the Mechanical and Aerospace Engineering Department and ROMAC industry consortium for their continued financial support throughout my tenure at UVA.

Contents

List of Tables

List of Figures

Abstract

Modern turbomachine analysis seeks designs that maximize efficiencies and push operational extremes, highlighting a continual need for accurate and efficient component level performance prediction methods. Annular seals are particular components found in a wide variety of turbomachinery applications that serve to reduce leakage flow across a region with a large pressure differential. Circumferentially grooved seals further reduce leakage through the use of grooved sections on the rotor or stator surfaces that serve to dissipate kinetic energy through the formation of vortices, though the addition of grooves adds significant complexity to the fluid dynamic response of the sealing component. Computational analysis of grooved seals includes simplified, one-dimensional bulk flow models and full Navier-Stokes computational fluid dynamics (CFD) studies. Bulk flow models, while efficient and easy to use, lack accuracy due to numerous assumptions, while full CFD studies display higher accuracy but are expert knowledge driven and computationally intensive.

This work seeks to address the limited accuracy of bulk flow models for circumferentially grooved seals through the use of a novel modeling approach based on an effective film thickness, a physical flow boundary that separates the jet flow in the seal clearance region from the recirculation flow within the seal grooves. A simplified, single groove CFD model is employed to establish the effective film thickness analysis framework, providing insight into the flow mechanisms dictating leakage performance and illustrating the potential for reduced empiricism in bulk flow modeling. This framework is then applied to shear stress modeling within the groove region, where the additional shear stress contribution is isolated and directly quantified as a correction to a traditional bulk flow shear stress definition. These shear stresses are termed here as form shear stresses (FSS) based on the close relationship between their behavior and the expansion and contraction of the effective film thickness. Models for the FSS are developed as functions of local Reynolds number and implemented into a simplified bulk flow method, demonstrating the ability of the novel modeling approach to capture physical flow behavior and eliminate the need for an empirical groove loss coefficient. Finally, a

rigorous sensitivity study examines the impact of the upstream and downstream regions, rotor centrifugal growth, and modeling whirl amplitude on the prediction of physical flow phenomena and rotordynamic coefficients from a quasi-steady full CFD method. The results highlight the careful consideration needed during model setup in order to realize the accuracy advantages assumed by the use of these higher fidelity methods. This work presents the first use of an effective film thickness in bulk flow analysis and shear stress modeling for grooved seals. The bulk flow developments of this dissertation set forth a new modeling approach that can be applied to many sealing scenarios for reduced empiricism and increased prediction accuracy, while the contributions to the knowledge base of full CFD rotordynamic prediction enable more widespread and appropriate use of higher fidelity methods for seal analysis.

Chapter 1

Introduction

1.1 Background and Motivation

Turbomachinery systems feature intricate networks of mechanical components and fluid domains and are recognized by the presence of components spinning with a high angular velocity in close proximity to other stationary ones. The successful use of many turbomachines, such as boiler feed pumps and electrical submersible pumps (ESP), in various industrial processes hinges on the treatment of a high pressure working fluid, leading to regions of high pressure differential across the machine. The question of overall efficiency becomes, in part, a function of the sealing capabilities at various locations, and the complexity of the fluid dynamic response within those sealing regions introduces the potential for prominent and adverse contributions to overall machine stability. The detailed analysis of the numerous sealing components thus becomes integral to the design of safe, reliable, and efficient turbomachines.

While a mechanical seal provides the best performance in terms of a reduction in undesired leakage flow, the contact between the rotating and stationary machine components creates friction and wears them down over time. This degrades performance, increases maintenance requirements, and potentially introduces unwanted physical material into the flow downstream of the seal if the components break down. As such, small radial gaps between the rotating (rotor) and stationary (stator) components of the machine are often configured along secondary, or leakage, flowpaths to inhibit fluid flow in these regions, as depicted in Fig. 1.1. These non-contacting annular seals offer a restriction of the leakage flow without the frictional downsides of their mechanical counterparts. A single turbomachine may include several types of annular seals at multiple locations. Such an example is shown in Fig. 1.1, where a multistage centrifugal pump features interstage

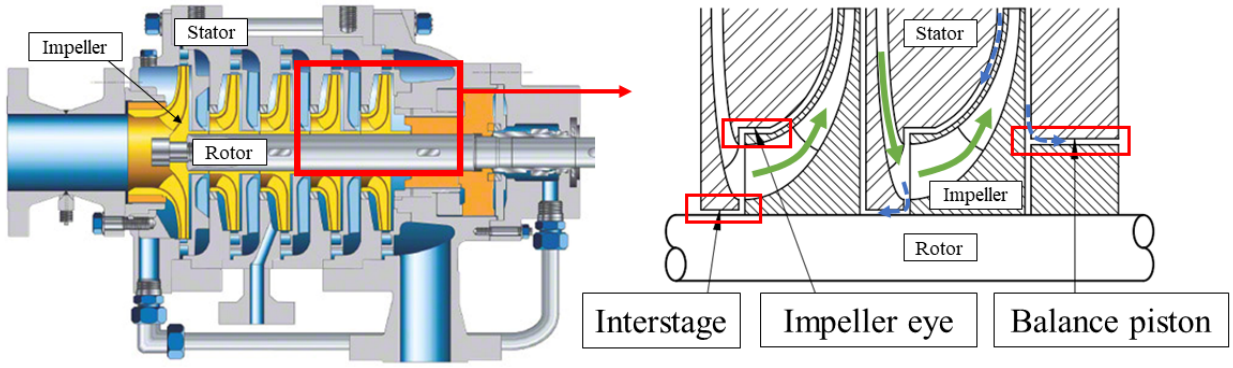

Figure 1.1: Left: Axial-radial cross-section view of a sample multistage centrifugal pump (adapted from [1]). Right: Diagram of the final two impeller stages, showing the type and location of major pump annular seals in red boxes (adapted from [2]). The primary flow path is given by solid green arrows and the leakage flow path by dashed blue arrows.

and impeller eye seals within a single stage and a balance piston seal after the final stage to equilibrate the full pressure rise across the pump. Typical annular seals have a radial gap, or clearance, between the rotor and stator surfaces on the order of 0.003 times the radius of the rotor [3]. This is slightly larger than the same clearance region for bearing components also frequently found in turbomachines. Varying geometry and operating conditions found in annular seals lead to flow Reynolds numbers as low as 100 [4] and up to 100,000 or higher [3], though the relatively larger clearances and high pressure ratios give rise to a majority of cases that fall in the turbulent regime [5].

Manufacturers will often machine circumferential grooves onto the rotor or stator surfaces within the seal, as shown on the left of Fig. 1.2. This further reduces leakage compared to a plain smooth seal by forcing the fluid through a more tortuous path that dissipates additional kinetic energy. The more complex flow path, depicted on the right of Fig. 1.2, now includes interactions between the recirculating flow within the groove and the jet-like flow in the clearance region, as well as sequential expansions and contractions at each transition between smooth (land) and groove seal sections. The high likelihood of turbulence and the complexity of the flow field in grooved seals creates a particularly difficult environment for analysis and performance prediction.

Steady-state performance of annular seals is often reported in terms of leakage and frictional power loss. While overall machine efficiency is dictated by the amount of leakage flow, the fluid flow within annular seals may also generate reaction forces that can have a pronounced effect on system stability [7]. These reaction forces develop as a result of the rotor being displaced to an eccentric position due to vibration

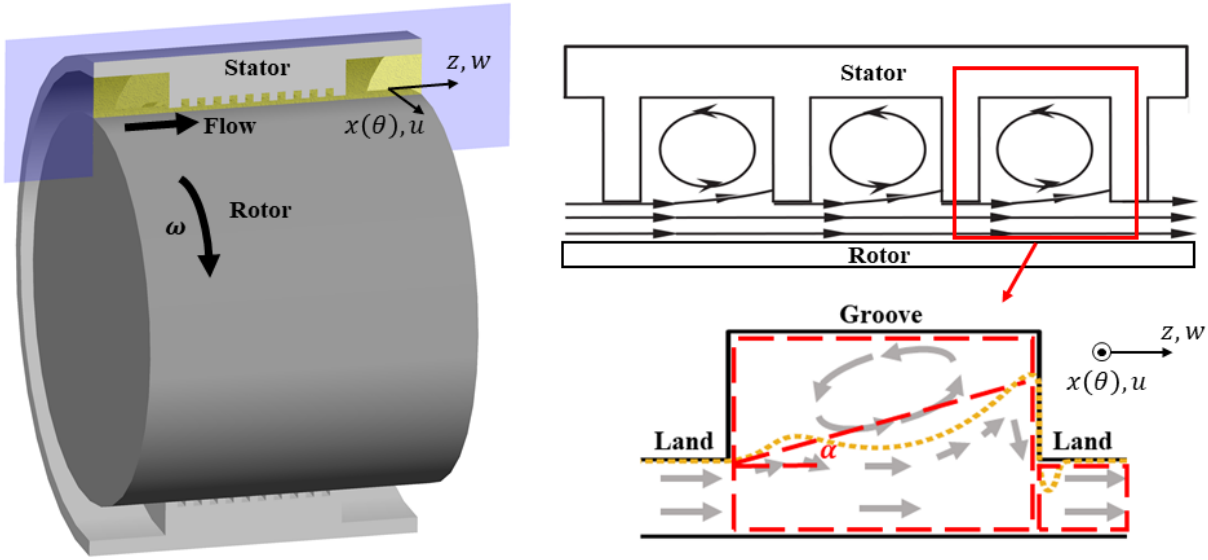

Figure 1.2: Left: Schematic view of a grooved annular seal. The axial-radial cross-section plane considered in much of this dissertation is given by the blue shaded region, while the fluid domain is given by the yellow shaded (textured) region. Right, top: Diagram of flow field in a grooved annular seal (adapted from [6]). Right, bottom: Flow features for a single groove, depicting the effective film thickness (yellow dotted line) and a typical three control volume definition (red dashed line) with a linear penetration angle α.

or other operational imbalances. Various viscous and inertial mechanisms determine the net effect of the reaction forces, with primary contributions originating from the circumferential variation of frictional loss, circumferential variation of velocity, and the wedge effect of converging and diverging films sections. The dynamic response of the seal resulting from the reaction forces is quantified through a set of rotordynamic coefficients that represent its stiffness and damping properties, loosely analogous to those of a mechanical system. These coefficients were formulated in the rotordynamics community to foster linear stability analysis of the overall turbomachines, where annular seals represent one of possibly many contributing components.

It is generally accepted that the addition of grooves in an annular seal causes a reduction in magnitude of the rotordynamic coefficients, but various studies in the literature have revealed systems with both increased and decreased stability properties when smooth seals are replaced with grooved ones [3]. Uncertainty in seal dynamic response predictions can lead to overestimated safety margins or, conversely, unchecked instabilities that lead to critical failure. Inaccurate static performance predictions can lead to designs with suboptimal efficiency. Rigorous and accurate modeling and analysis methods for annular seals, in particular circumferentially grooved seals, is thus of great importance to modern turbomachinery design as technological advancements seek to maximize efficiency and push operational extremes.

Traditionally, Darcy-Weisbach type friction factors were employed for annular seal modeling purposes (e.g. [8]) despite being originally formulated to describe pipe flow friction losses. A slightly different approach known as the ”bulk flow” method was developed a few decades later. In bulk flow methods, radial variation in pressure and velocity across the clearance are neglected, and the fluid domain is treated in a ”bulk” or radially averaged manner. Further averaging in the axial and circumferential directions over a geometric control volume (CV) serves to define the bulk flow variables as functions of a single axial dimension. The circumferential variations that lead to developing reaction forces are then captured using a perturbation analysis based on an assumed circular whirl of the rotor in the circumferential direction. The work of Black [7] and Hirs [9] serve as fundamental studies that established the foundation for bulk flow methods still employed today. In the case of grooved seals, additional CVs are often employed to capture the influence of the fluid within the groove. A sample breakdown for a typical three CV method is shown on the right side of Fig. 1.2, where the penetration of the clearance flow into the groove region is approximated by a linear expansion of the clearance flow CV. The result of these approximations and simplifications is a set of extremely efficient seal analysis tools that have been utilized for decades in industry and academia.

By necessity, one-dimensional CV bulk flow methods rely heavily on numerous empirical correlations to capture the effects of wall shear stresses and fluid-fluid CV interactions. This leads to limited prediction accuracy that is driven by the uncertainty in the fitted empirical coefficients. A tradeoff thus exists between the efficiency and accuracy of simplified bulk flow methods. This is illustrated by the results of Kocur et al. [10] who surveyed the industry to highlight major bulk flow prediction inconsistencies. The authors compiled rotordynamic predictions for a single seal case from industrialists, consultants, and academics that utilized prominent annular seal bulk flow codes. The rotordynamic coefficients reported by respondents, kept anonymous per survey standard, are shown in Fig. 1.3. The results differed by up to an order of magnitude, fueled mostly by the large discrepancy that exists in the definition and fitting of the empirical coefficients. While advancements in liquid and gas seal bulk flow rotordynamic prediction have been made since the publishing of that work (e.g. [11, 12]), the core bulk flow formulations used in the last decade, and thus the inherent challenges to their use, has remained primarily the same.

An increasingly prevalent alternative to the bulk flow approach is the use of full computational fluid dynamics (CFD) methods for higher fidelity seal analysis. In contrast to the extensive simplifications of bulk flow methods, full CFD methods make few, if any, assumptions regarding the nature of the fluid flow and directly solve the complete discretized Navier-Stokes equations within the entire fluid domain of the seal.

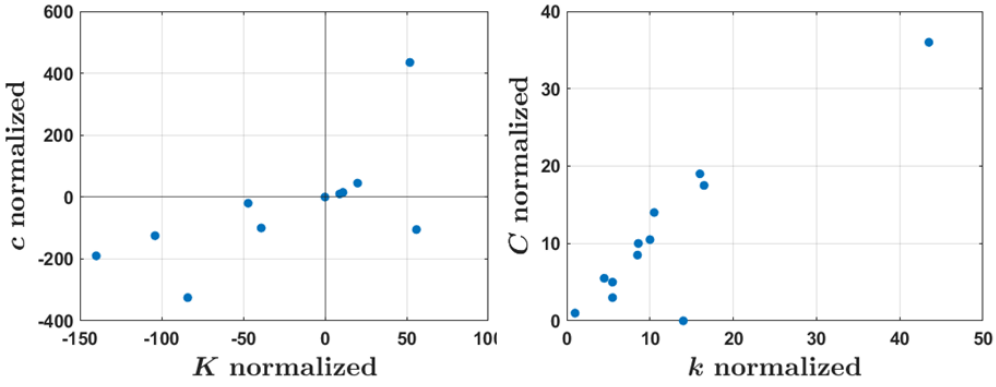

Figure 1.3: Reported bulk flow rotordynamic coefficient predictions (cross-coupled damping vs. direct stiffness on left, and direct damping vs. cross-coupled stiffness on right) for an impeller eye labyrinth seal, compiled by Kocur et al. [10].

Some assumptions must still be made, such as in the choice of turbulence model to achieve closure of the Reynolds Averaged Navier-Stokes (RANS) equations. Still, CFD methods are applicable to a wide array of sealing scenarios and have been shown to provide more accurate performance predictions than their simplified counterparts. Modern use of CFD methods for seal analysis focuses on applying multipurpose commercial CFD software to specific annular seal cases. Methods based on steady state analysis in a rotating coordinate frame or fully transient analysis exist with varying levels of maturity and computational requirements, though all CFD methods come at an exponentially higher computational cost than their bulk flow predecessors. While the use of full CFD methods is slowly becoming a more standard rotordynamic engineering practice, the computational expense and expert knowledge required to realize the accuracy benefits remains a challenge. This fuels continual research into both bulk flow and CFD seal analysis methods [12].

1.2 Objectives and Outline

This dissertation seeks to advance the use and accuracy of both bulk flow and full CFD methods for rotordynamic analysis of circumferentially grooved annular pressure seals. The heavy reliance of bulk flow methods on well fitting empirical coefficients warrants investigation into a more physical modeling approach. This allows for the underlying flow mechanisms to be explored and incorporated into updated bulk flow methods towards a more accurate prediction of steady state performance and dynamic response. In addition, the lack of systematic guidelines and regularity in reporting that currently exists for full CFD methods requires careful scrutiny. This will foster more widespread use of these methods for both fundamental

physics investigations and regular rotordynamic prediction for annular seals. Given the current status of circumferentially grooved seal performance prediction outlined above, this dissertation seeks to answer the following research questions, addressed in Chapters 2, 3, and 4 respectively:

1. Can a more physical effective film thickness be defined for bulk flow analysis of circumferentially grooved seals? Does its use provide additional insight into flow behavior and seal performance?

2. How can the use of a more physical film thickness shape change and improve shear stress modeling for bulk flow prediction of circumferentially grooved seals?

3. How do certain meshing and modeling choices in CFD rotordynamic analysis methods affect the results of seal performance prediction? Can this be quantified towards a more rigorous treatment of sensitivity and uncertainty?

In Chapter 2, a series of simulations using a simplified single groove CFD model are used to establish the concept of the effective film thickness, a physical control volume boundary separating the flow in the clearance region from that of the recirculation region within the groove that faithfully follows the expansion and contraction of the film. This effective film thickness is depicted by the yellow dotted line in the bottom right of Fig. 1.2. An analysis of the film thickness and associated flow metrics across a range of operating conditions and geometries provides valuable insight into the mechanisms dictating changes in performance. The primary objective of Chapter 2 is thus to quantify the effective film thickness and use it to establish a novel modeling framework for grooved seals that creates a foundation for a reduction in uncertainty and empiricism in bulk flow predictions.

Chapter 3 builds on the foundation of Chapter 2 by directly addressing the shear stresses within the groove region, a primary source of uncertainty in bulk flow predictions. Using effective film thickness based analysis, the additional shear stresses within the groove are isolated and quantified as a correction to traditional shear stress definitions. The term form shear stress (FSS) is adopted as a result of the close relationship in qualitative behavior between the additional groove shear stresses and the shape, or form, of the effective film thickness. Models for the FSS as functions of local Reynolds numbers are developed, and their predictive capability is assessed through additional single groove and full seal CFD simulation results. The influence of the FSS approach on bulk flow predictions is demonstrated through implementation of the FSS models into a simplified bulk flow method. The primary objective of Chapter 3 is to quantify and model

the form shear stress components and demonstrate the ability of the form shear stress approach to capture the physical flow behavior observed in grooved seals.

Full CFD rotordynamic prediction is the subject of Chapter 4, where a common quasi-steady (QS) method is utilized to generate leakage and rotordynamic coefficients for an array of setup and modeling choices. Variations in local mesh refinement, upstream and downstream regions, rotor centrifugal growth, and modeling whirl amplitude are considered in terms of their effect on rotordynamic coefficient prediction and the relationship to predicted flow fields and physics. The primary objective of Chapter 4 is to provide a more rigorous and comprehensive analysis of the influence of these prominent modeling features on a frequently used full CFD rotordynamic analysis method.

This work presents the first time that an effective film thickness has been quantified and used in bulk flow analysis for grooved seals, and the first time that an effective film thickness analysis framework has been utilized to quantify and model the additional shear stress contributions within the groove region. In addition, this dissertation includes the first work dedicated to a comprehensive study on the influence of certain modeling parameters on rotordynamic prediction for an incompressible grooved seal when using the quasi-steady method. The bulk flow modeling foundation established in this work creates a platform for reduced empiricism and significant improvements to prediction accuracy. The analysis of the full CFD results highlights modeling areas critical to prediction accuracy and provides suggestions for best practice when applying full CFD methods. In total, this dissertation advances the use of both simplified and higher fidelity rotordynamic analysis methods through improved understanding and modeling of grooved seal flow physics.

Chapters 2, 3, and 4 of this dissertation are each written as individual manuscripts capable of standing alone. Each chapter contains its own introduction, review of the literature, and concluding summary specific to the technical content within it. A final chapter with overall concluding remarks, statements on the significance and impact of the dissertation, and avenues for continuation of the present work close this dissertation.

Chapter 2

Grooved Seal Effective Film Thickness Analysis

This chapter has been published in the *ASME Journal of Engineering for Gas Turbines and Power*. The publication details are given by Ref. [13], which is referred to directly in subsequent chapters. The corresponding manuscript title is "Circumferentially Grooved Seal Flow Field Analysis Based on Effective Film Thickness to Improve Bulk Flow Models."

Nomenclature

u, w	Circumferential, axial velocity	Δp	Model pressure differential
x, z	Circumferential, axial direction	Δp_{gr}	Groove pressure drop
R	Rotor radius	ρ	Density
L	Single groove model length	μ	Viscosity
L_g	Groove length	$Re_{x,z,tot}$	Reynolds number (circumferential, axial, total)
D_g	Groove depth	AR	Groove aspect ratio
c	Clearance	A_{exp}	Expanded area
h	Film thickness	$\tau_{z,rz,sz}$	Shear stress (axial, rotor, stator)
p	Pressure		

2.1 Introduction

Annular seals are found in a wide range of turbomachinery applications for the purpose of reducing leakage flow across a region with a large pressure differential. A typical multistage centrifugal pump, for example, may employ annular seals at different stages, including as impeller neck ring seals, interstage seals, and as balance drums to equilibrate the full pressure rise across the pump. Circumferentially grooved seals offer a reduction in leakage by dissipating kinetic energy through the tortuous path the fluid must traverse as it transitions between land and groove sections. Such seals can have a significant impact on overall pump performance with respect to leakage and instability issues, making their analysis vital to pump design [3]. Current trends in turbomachinery seek to maximize efficiencies and push operational extremes, highlighting a continued need for improving the accuracy and extending the capabilities of current analysis methods.

Seal performance prediction is typically broken into the categories of simplified bulk flow models and full computational fluid dynamics (CFD) studies. Advances in computational capability and resources has lead to increases in CFD studies of seals, with various techniques, including quasi-steady [14, 15, 16] and transient [17, 18, 19] methods, being used and continuously developed. A persistent drawback of this approach is the large computational time required for single data points, rendering large parametric space or design optimization studies for full seals practically infeasible. This, along with the complexity of the setup and newness of many of the methods, makes widespread, regular use of CFD for seal design and analysis still a future prospect. Bulk flow models are thus an enticing and necessary alternative for the present due to their efficiency.

Grooved seal flow contains two distinct regions separated by a dividing streamline, as depicted in Fig. 2.1. Outside of the grooves is a jet flow (thin film) region representing the leakage flow, and inside the groove is a recirculating flow region. In land sections where no groove is present, flow behavior is dictated by shear stresses on the rotor and stator surfaces. In groove sections, shear stresses between the recirculating flow and the groove walls as well as interaction between the recirculating and jet flow regions are of importance. Groove geometry and flow region interaction dictate expansion and contraction of the thin film where additional losses can occur. In bulk flow models, the flow regions are sectioned into a series of control volumes (CV), where simplified physics and empirical correlations can be employed to solve a reduced, one-dimensional problem much more efficiently than full CFD, but with reduced accuracy. These reduced models require significant assumptions regarding the shape of the thin film and the frictional forces, leading to

numerous correlations and fitted parameters whose variation among in-use codes leads to high uncertainties. Kocur et al. [10] present a comprehensive review of bulk flow prediction for a compressible grooved seal case study, highlighting up to an order of magnitude difference among reported results. Similar variance exists among predictions for incompressible flow seals which were chosen for this study due to modeling simplifications, though the approach presented here can be applied to compressible flow seals in the future.

The steady state bulk flow equation for conservation of axial momentum in the jet flow region is given by

$$\frac{\partial p}{\partial z} = -\frac{1}{h}(\tau_{rz} + \tau_{sz}) + \frac{\rho w^2}{h}\frac{\partial h}{\partial z} \tag{2.1}$$

where continuity for an incompressible fluid has been substituted for the axial velocity gradient term. The prominence of the shear stresses τ in the bulk flow equations and the close relationship they share with the bulk velocities make them among the most important empirical correlations in bulk flow analysis. They are typically modeled following Hirs turbulent thin film theory [9] using Blasius type friction factors as functions of the Reynolds number of the form $\lambda = aRe^B$ for empirical coefficients a and B. An early model for liquid grooved seals by Nordmann et al. [20] employed a single CV and an average clearance with different friction factors on each surface to account for geometry changes due to grooved sections, yielding reasonable predictions that matched the general trends of their experimental results for an eight groove seal. To consider the flow within the groove, Iwatsubo and Sheng [21] added a second CV to differentiate between land and groove sections, including an additional empirical loss coefficient to capture the pressure changes between land and groove sections that are crucial to accurate prediction of grooved seal pressure behavior [22]. Again, trends in force coefficients were captured but their magnitude was overpredicted. A more detailed description of the flow within the groove was incorporated into three CV models (depicted in Fig. 2.1), first proposed by Florjancic [23] and adapted by Marquette and Childs [24], where the jet flow and recirculating flow within a groove section were separated by a linear penetration angle (α in Fig. 2.1) meant to approximate the dividing streamline. Marquette and Childs report very good leakage and slightly underpredicted stiffness and damping coefficients with their model. In general, modest but notable improvements were reported as more CVs were added, though the authors regularly noted the necessity of appropriately tuned empirical coefficients in shear stresses and CV boundary conditions in order to achieve such accuracy. More recent work by San Andres et al. [12], and subsequently by Wu and San Andres [25] for additional groove geometries, updated components of the three CV theory in [24], showing improved accuracy in dynamic predictions by using CFD-derived penetration angles and friction factor coefficients. To date, the mostly widely used bulk flow

codes for incompressible grooved seals still rely heavily on empirical quantities, such as friction factors and loss coefficients, and on assumptions regarding the shape of the thin film.

Fundamentally, grooved seal flow falls under the category of flow over a cavity, which is not new to the literature. Grooved, liquid seals represent a small subset in this space, characterized by incompressible fluids, combined Poiseuille and Couette type flows, small channel heights, and high Reynolds numbers despite small clearances due to high pressure differentials, typically resulting in turbulent flow. Rhode et al. [26] used a novel approach to alleviate numerical issues when simulating incompressible flow in groove-on-rotor configurations, comparing variable values across radial profiles and computing shear stresses along the groove walls and along a line connecting groove corners meant to approximate the location of the free shear layer. In further assessing the accuracy of numerical methods for grooved seal flow, Demko et al. [27] explored the influence of Taylor number on flow patterns, where high Taylor to Reynolds number ratios were found to cause the dividing streamline to extend outside of the cavity due to inertial forces directed away from the grooves on the rotor. Morrison et al. [28] expanded the experimental database for comparison by using laser doppler anemometry (LDA) to provide additional flow field measurements, confirming general flow features and presenting a full spatial description of the Reynolds stresses. Subsequent work has included flow field information as a qualitative method for discussion and explanation, though explicit quantification or use of the true physical film shape has yet to be investigated.

The present work seeks to quantify an effective film thickness that faithfully follows the behavior of the dividing streamline to more accurately capture localized behavior of the thin film and related flow quantities. Shifting to a control volume boundary based on this true physical film behavior in bulk flow analysis of circumferentially grooved seals will highlight the mechanisms dictating the flow changes and ultimately enable the reduction in uncertainty or elimination of traditionally used bulk flow coefficients. An axisymmetric, single groove numerical model is created and simulated for a range of operating conditions. Quantification of the effective film thickness allows for analysis of flow patterns, bulk shear stresses, and net film expansion into the groove for a deeper understanding of the groove flow behaviour and changes in leakage. Similar results are presented for simulations of grooves with varying aspect ratios, leading to suggestions for geometries to minimize leakage based on net film expansion. This is the first paper to explicitly quantify an effective film thickness for use in bulk flow analysis. The insights provided by this approach offer avenues for new model development based firmly in flow physics and behavior and the potential to eliminate particular empirical coefficients. Thus, with an effective film thickness as the foundation, substantial improvements in

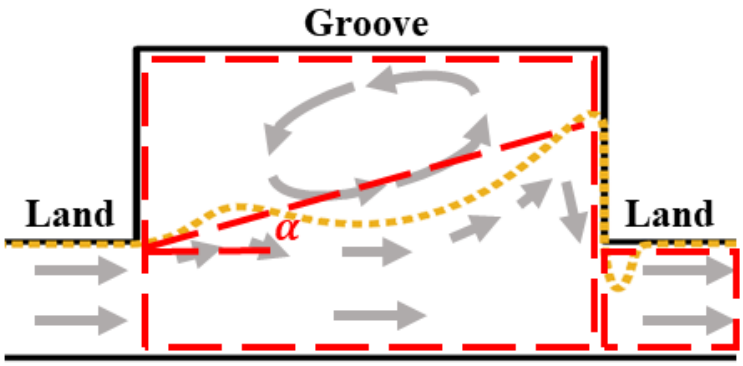

Figure 2.1: Grooved seal flow field diagram. Dividing streamline shown with yellow dotted line. Typical 3CV breakdown shown with red dashed line.

bulk flow prediction accuracy for grooved seals is now possible.

The remainder of this paper is structured as follows. The single groove CFD modeling setup is first outlined, followed by a brief description of the processing methods employed in this study. Results pertaining to flow patterns, shear stresses, and expanded area are then detailed. Finally, the effect of groove aspect ratio on the aforementioned quantities is examined, followed by concluding remarks.

2.2 Methodology

A simplified CFD model of a single groove was created to enable detailed exploration of the flow physics in grooved seals. Careful consideration and choice of geometry, mesh, boundary conditions, and modeling assumptions, outlined below, established a well grounded platform for the effective film thickness based analysis presented in this paper.

The base seal model chosen for this study follows the geometry of the experimental work by Marquette et al. [29] due to the availability of the data and its applicability to industry relevant pump applications. This study focused on a single, downstream groove to minimize computation time and simplify the analysis while retaining the core flow features important to full grooved seals. The model consisted of a groove section in between two land sections of length equal to half the land length of the experimental seal. The total length of the single groove model is $L = 3.174$ mm with a clearance $c = 0.1105$ mm and groove depth $D_g = 1.587$ mm. The use of a single groove model relies on an assumed equal pressure drop across each land-groove section in a full seal, a concept well established in the literature (see e.g. [14]) and that is used in other single

groove CFD studies (see e.g. [25]). Water is the working fluid with its density and viscosity specified (see Table 2.1) to match the properties of the experimental working fluid (water at 54.4C as in [29]).

Simulations were run using the computational software ANSYS CFX v. 2021 R1 that utilizes a finite volume based solver to evaluate the full discretized Reynolds Averaged Navier Stokes (RANS) equations. Isothermal conditions were used, and temperature dependent fluid properties were accounted for through properly specified density and viscosity. A quasi-two dimensional model was created using a 0.05 degree sector of the full seal circumference with three circumferential elements and rotationally periodic interfaces to leverage the axisymmetric geometry of the annular seal and reduce computation time. To avoid the need to directly specify an unknown velocity profile and direction at the model inlet, an axial interface is utilized that matches the velocity profiles at the model inlet and outlet and conserves mass flow, as shown in Fig. 2.2. Convergence to steady state under these conditions yields fully developed flow and represents a single groove sufficiently downstream of the seal inlet, where the flow profile entering a groove section is identical to the flow entering the previous groove section, further discussed below. As the fluid is incompressible, the net pressure drop across the single groove, independent of absolute pressure magnitude, is sufficient to determine the flow field and is specified in combination with the axial interface. Both interface sets were specified as flux conservative, and the rotor and stator surfaces were specified as smooth walls under the no-slip condition. The single groove pressure differential is considered to be the total seal pressure differential divided by the number of grooves, consistent with the assumption of equal pressure drop across each land-groove section described above, and is varied between 3-7 bar (not considering the pressure loss at the seal inlet plane). The rotor speed is varied between 0-24 krpm. The operating conditions were chosen to encompass the range studied in [29] and are representative of conditions relevant to industrial pump applications.

Turbulence closure of the RANS equations was achieved using the Shear Stress Transport (SST) turbulence model [30] based on its use in similar turbomachinery studies (e.g. [16]) and the ability to leverage the low-Re formulation using appropriate meshes at low computational cost given the relatively small computational domain in this study. Meshing was performed with the CFX Meshing utility, where a structured hexahedral mesh was created. Biasing element sizes near walls allowed for near wall refinement sufficient to achieve $y^+ < 5$ for all cases, placing the first node within the viscous sublayer, suitable for use with the SST turbulence model [30]. A final residual criteria of 1e-10 RMS was chosen after extensive testing, presented below, to ensure each simulation had reached steady state and the velocity profiles across the clearance and groove were independent of the grid or residual criteria chosen. See Table 2.1 for a summary of the geometry,

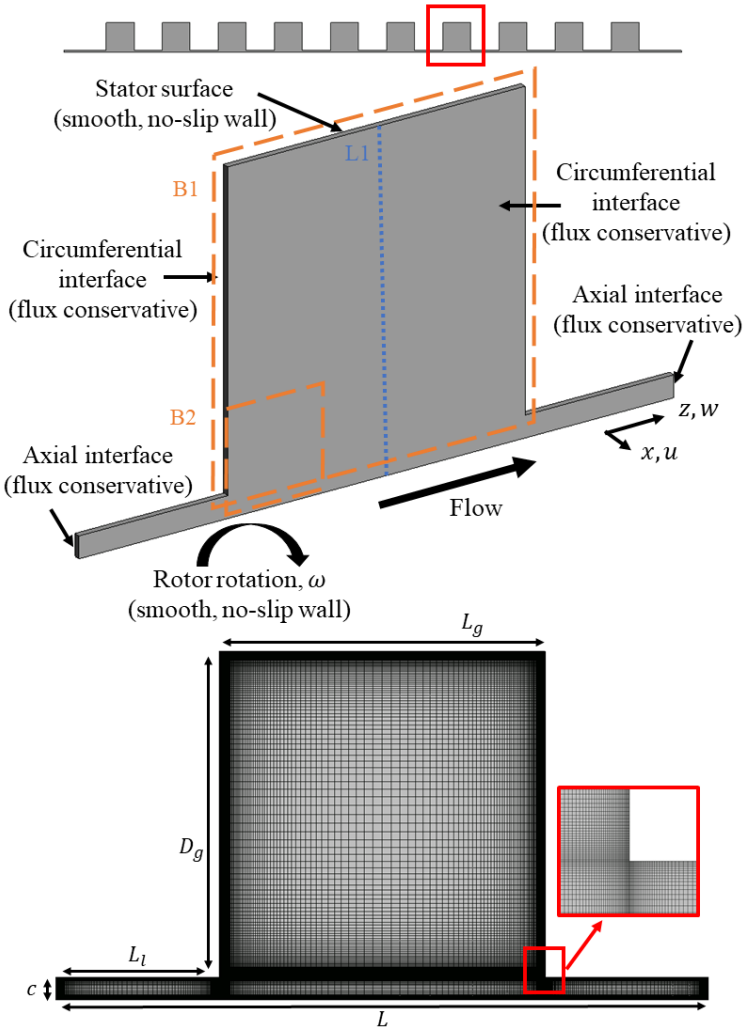

Figure 2.2: Modeling diagram and final mesh used.

operating conditions, and setup parameters used in this study.

A series of grids were chosen with various levels of refinement to investigate grid dependence, where $y+$ was kept approximately constant across the refined grids to isolate the effect of grid density. Total number of elements varied from 167k to 930k. Grid independence was verified for four sets of operating conditions at lower and upper bounds for the set of rotor speeds and pressure differentials examined in this study. Initially, simulations were run to a residual convergence criteria of 1e-6 RMS, a standard criteria, if not tighter, than is used for similar CFD studies of turbomachinery components (e.g. [31]). While leakage displayed mesh independence at this criteria, a comparison of film thicknesses and velocities across the seal clearance and groove showed systematic differences between grids, indicating more iterations were required for the

Table 2.1: Operating conditions and seal geometry.

Working fluid	Water
Density	984.5 kg/m^3
Dynamic viscosity	5e-4 kg/m s
Rotor speed, ω	0-24 krpm
Pressure differential, Δp	3-7 bar
Land length, L_l	0.7935 mm
Groove length, L_g	1.587 mm
Groove depth, D_g	1.587 mm
Clearance, c	0.1105 mm
Rotor radius, R	38.252 mm
Turbulence model	SST
Circumferential interface	Rotational periodicity
Axial interface	Translational periodicity with pressure change
Convergence criteria	1e-10 RMS
Conservation target	1%

simulation to reach steady state. Figure 2.3 gives one such example case. (See Secs. 2.3 and 2.3.1 for details on the effective film thickness.) Systematic convergence to full steady state was achieved by driving the RMS residuals below 1e-10, where film thicknesses and velocities then overlapped almost exactly. A grid with 167k elements (see Fig. 2.2) was then chosen as it was verified to be mesh independent through a visual comparison of film thickness and velocity profiles and by observing a $< 1\%$ difference in leakage across all grids at the tighter residual criteria.

Fully developed flow occurs when the flow field across a groove section no longer changes with axial location. Beyond the axial location where this occurs, the flow field within a groove section becomes axially repetitive and is nearly identical for successive groove sections. An accompanying CFD model of the full seal was used for comparison against the single groove model to verify the applicability of the fully developed assumption. No inlet region was included in the full seal model, so the full seal pressure differential and inlet velocity direction were adjusted to account for the pressure drop that would be present at the seal inlet plane transition and to match the leakage of the target experimental case (within 2%) at Δp = 55.2 bar and ω = 24600 rpm. This resulted in a single groove pressure drop of 3.7 bar. Figure 2.4 shows velocity contours for the 7th groove from the full seal model and the single groove model at 3.5 bar and 24000 rpm. Close agreement between the full seal groove, where the experimental leakage was matched, and single groove flow patterns serves to confirm the applicability of the single groove model for fully developed

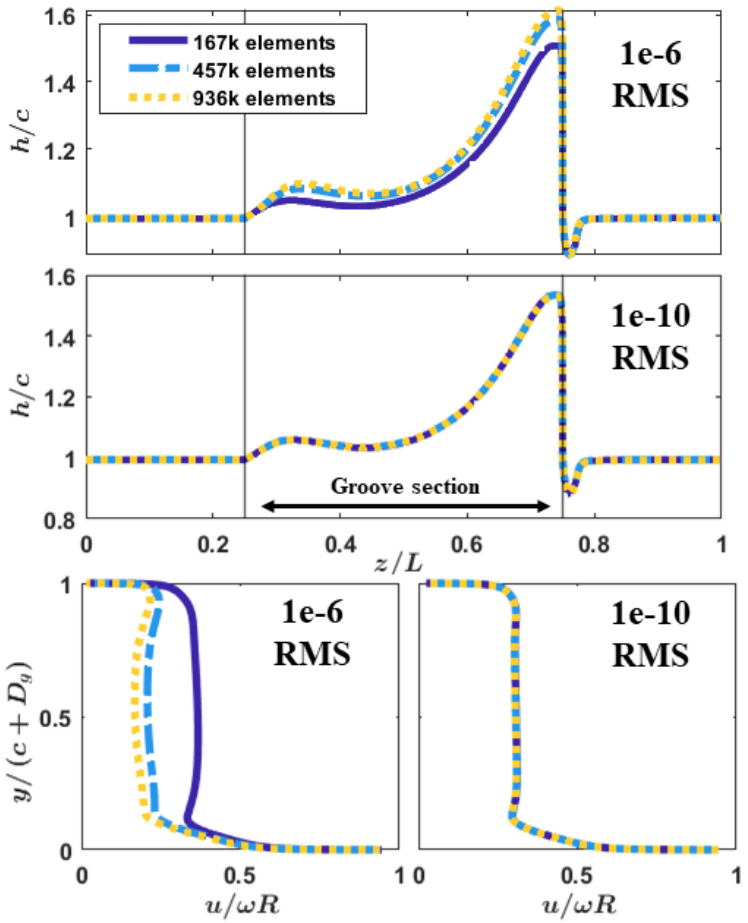

Figure 2.3: Mesh independence verification. Top: Film thickness. Bottom: Circumferential velocity along a radial line at the groove center (line L1 of Fig. 2.2).

flow. Examination of all grooves in the full seal model showed almost identical flow fields from the 7th groove onward, indicating that the assumption of fully developed flow is valid for grooves 7-10 in this particular case. This distinction will change based on seal geometry and operating conditions and depends predominantly on the axial development of the circumferential velocity. It is assumed that, given appropriate mesh independence, extrapolation around this set of operating conditions will also yield accurate results. Direct validation of the flow fields was not possible as no experimental flow field measurements were included in [29], a common trait among experimental results for grooved seals when rotordynamic coefficient results are included. The use of a well validated software (ANSYS CFX) and standard rotordynamic practice in modeling serves as justification for the present approach.

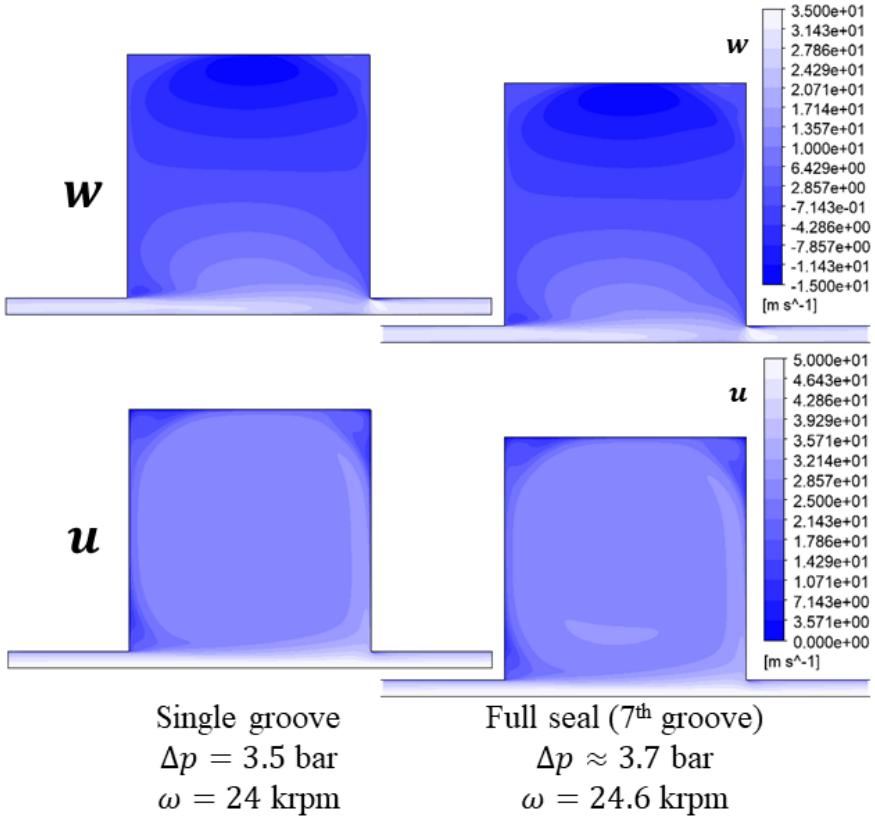

Figure 2.4: Comparison of single groove model to downstream groove of full seal model. Top: Axial velocity contours. Bottom: Circumferential velocity contours.

2.3 Analysis

In order to further understand the mechanisms dictating grooved seal flow behavior and highlight areas and avenues for improvement in bulk flow modeling, the following sections examine the flow patterns, film thickness, local effective shear stresses, and expanded areas within the current data set, followed by analysis of an additional data set with varying groove aspect ratio. This analysis hinges on the effective film thickness, a physical boundary between the jet flow and recirculating flow regions in a grooved seal, that faithfully follows the expansion and contraction of the fluid film as it traverses from land to groove and vice versa. The lower boundary of the effective film is the rotor surface. The upper boundary is defined using the dividing streamline, found as the radial-most streamline that traverses the entire axial length of the seal model starting from the model inlet, including both half land sections on either side of the groove, as depicted in the top of Fig. 2.5. Streamline computations are performed externally using raw data from an axial-radial plane exported from CFX results.

Bulk flow quantities are found using a local averaging procedure, where the local film thickness determines the radial extent of a cut line, across which the pressure and velocities are averaged. This procedure is depicted in Fig. 2.5, along with a sample set of bulk flow quantities and their local variation across the single groove model. Note the Bernoulli-like relationship between the film thickness and the pressure and velocities, where a film expansion corresponds to a local decrease in velocity and increase in pressure.

Much of the analysis is presented in terms of Reynolds numbers defined as $Re = 2c\rho V/\mu$, where V is the bulk flow velocity in the land section of the model, u or w for circumferential and axial directions respectively, or $\sqrt{u^2 + w^2}$ for the total or resultant Reynolds number. The characteristic length is chosen in accordance with standard seal analysis as the hydraulic diameter, defined as four times the flow area divided by the wetted perimeter, or $2c$ for an annulus. This allows relationships originally developed for circular pipes, such as turbulent flow Reynolds number thresholds and friction factor equations, to be applied to the non-circular duct flows found in annular seals. In this analysis, it is assumed that $u = 0.5\omega R$, half the rotor surface speed, for the Reynolds number calculations based on the Couette type circumferential velocity profile across the thin film in land sections of annular seals.

2.3.1 Effective Film Thickness and Flow Patterns

Definition and quantification of the effective film thickness serves as the basis for the bulk flow analysis in this study. The relationship between operational conditions, flow features, and the effective film thickness is first presented in this section.

The effective film thickness is examined across sets of operational parameter variations and is shown in Fig. 2.6. We first note the initial film expansion at the groove entrance, a slight depression at the groove center, the large expansion at the end of the groove, and the sharp contraction and vena contracta at the groove to land transition. Here, we make no assumptions on the shape of the film, and the physical nature of the effective film can now capture previously neglected effects, such as the groove to land transition vena contracta, that are important to seal behavior. These general characteristics of the film are persistent throughout the data set, with fluctuations in magnitude based on operating conditions. The effect of rotor speed on the film thickness is depicted in the top of Fig. 2.6 for the set of cases at $\Delta p = 3$ bar, where an increase in rotor speed tends to slightly decrease the magnitude of the initial expansion and increase the expansion height at the end of the groove. Similar but mitigated trends, and slightly lower peak values, are seen for the $\Delta p = 7$ bar set, indicating a film depression effect at higher pressures and axial velocities, likely due to a decrease in time

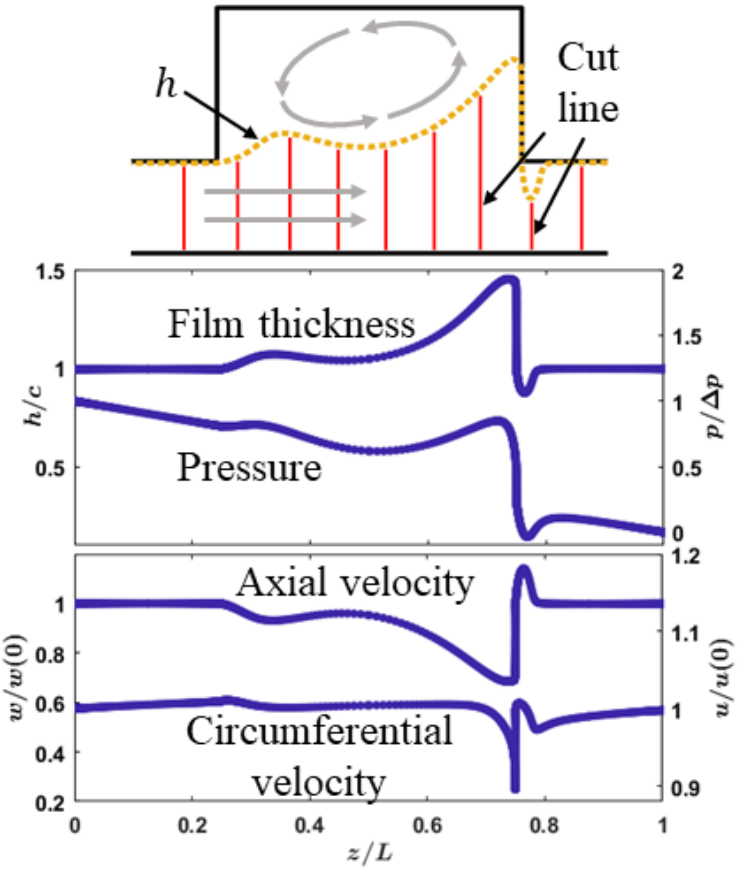

Figure 2.5: Bulk flow averaging procedure and sample results for the film thickness, pressure, and axial and circumferential velocity ($\Delta p = 3$ bar, $\omega = 24$ krpm).

to expand at higher axial velocities. The increase in film thickness with rotor speed can be attributed to centrifugal inertia, where higher circumferential velocities tend to force the fluid further radially outward and into the groove. Similar trends were observed in [27] for high Taylor numbers, where the film shape tended to shrink due to centrifugal forces pushing the fluid radially away from the groove (groove on rotor configuration), confirming the influence and importance of circumferential and centrifugal effects on film shape and flow patterns in grooved seals.

Figure 2.7 links the changes in film thickness shape to the flow structures of the grooved seal flow. The top row shows the magnitude of out of plane curl in the groove (window B1 in Fig. 2.2), a measure of the main recirculation vortex strength, for the $\Delta p = 3$ bar set at low and high rotor speeds. Higher rotor speeds show a decrease in recirculating vortex strength, an intuitive result corroborated by the decrease in jet flow axial velocity (leakage) that drives the recirculation. Comparing this to the film thickness of Fig. 2.6, we find

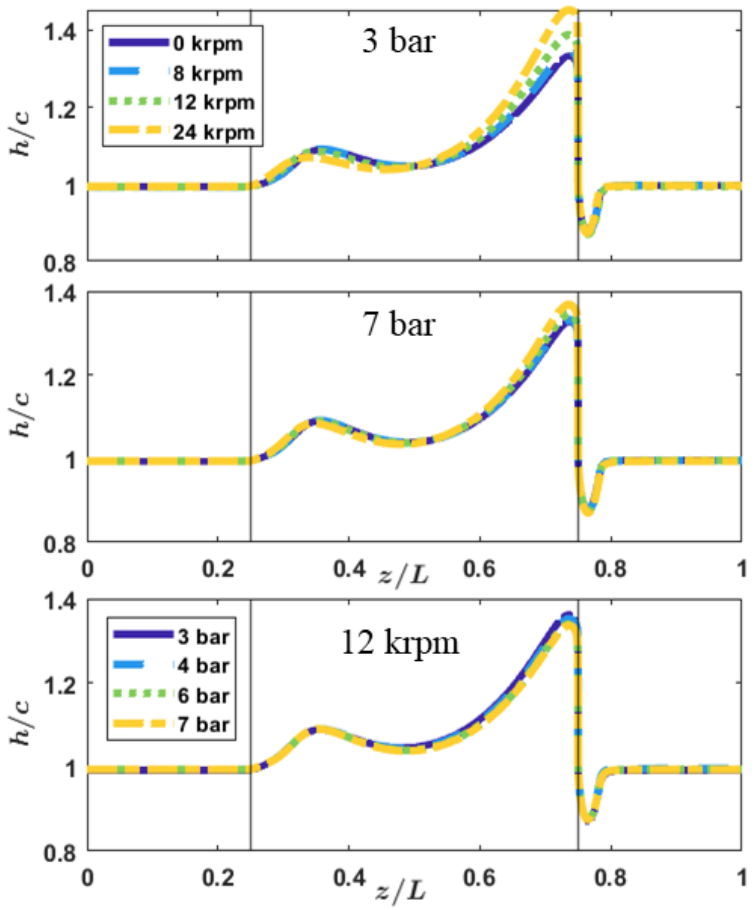

Figure 2.6: Comparison of film thicknesses for changes in operating conditions. Top: Varying rotor speed at 3 bar and 7 bar. Bottom: Varying pressure differential at 12 krpm.

that the increase in penetration of the film thickness into the groove is associated with the decrease in vortex strength. The bottom of Fig. 2.7 shows streamlines at the groove entrance (window B2 in Fig. 2.2), where increasing rotor speed decreases the size of the initial separated recirculating region. This is again reflected in the film thickness by the decrease in initial expansion, shown in the top of Fig. 2.6, due to reduced separation caused by a weaker main vortex.

A comparison of film thicknesses for a set of pressure differentials at constant rotor speed ω = 12 krpm is shown in the bottom of Fig. 2.6, showing a slight depression in the film with increasing pressure, though this effect is less significant than the changes in film with rotor speed.

The extent of the film penetration into the groove is found to be almost entirely determined by the Reynolds number ratio Re_x/Re_z. Note that this Reynolds number ratio is equivalent to the ratio of circumferential to axial velocity, since the density, viscosity, and characteristic length are the same for both Re_x/Re_z. As such,

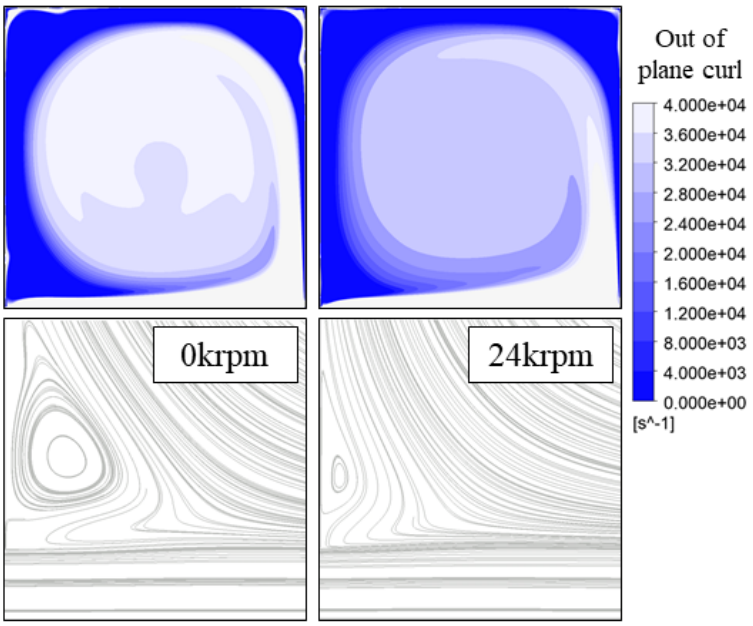

Figure 2.7: Flow field comparison at 3 bar. Top: Out of plane curl in the groove section (window B1 of Fig. 2.2). Bottom: Streamlines at the groove entrance (window B2 of Fig. 2.2).

it can alternatively be interpreted as a kinematic characteristic of the flow describing the flow direction in the axial-circumferential plane. Figure 2.8 depicts this relationship for the maximum film thickness, the highest radial point along the film, where a quadratic curve fit yields an R-square value above 0.99. This trend is consistent with the behaviour of the penetration angle α in [12] used to approximate the film thickness, where α increases with lower pressure/higher rotor speed, though no maximum penetration is observed for the range of operating conditions in this study.

The predictable behavior of the film as a function of the Reynolds number ratio demonstrated above can serve as a basis for the development of a functional model of the effective film thickness for use in bulk flow codes. Having linked the effective film thickness and flow patterns to operational changes on a physical level, the underlying mechanisms driving those changes can then be quantitatively explored through the shear stresses and expanded areas presented in the next sections.

2.3.2 Shear Stress

Steady state bulk flow behavior of grooved seals depends heavily on shear stress, and bulk flow predictions are dictated by their magnitude and distribution across the seal. Here, local quantification of an effective

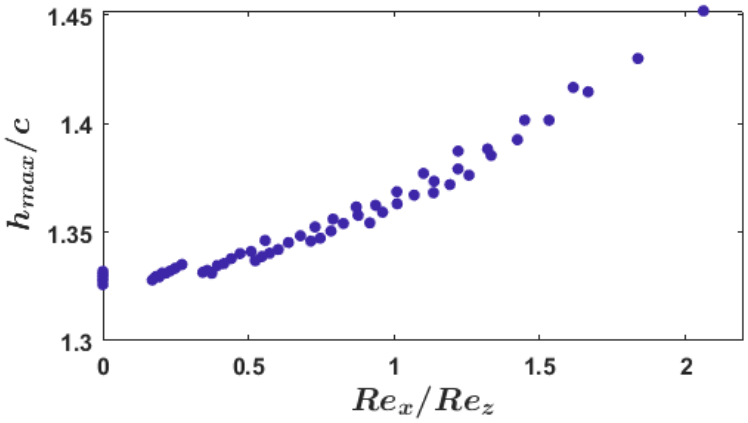

Figure 2.8: Maximum film thickness vs. Reynolds number ratio for all cases.

shear stress is presented so that the driving mechanisms behind the film thickness, flow pattern, and leakage variations with pressure differential and rotor speed can be examined.

The focus in this study is on the axial shear stresses which predominantly affect seal leakage in the steady state. By recognizing the second term on the right hand side of Eqn. 2.1 as an inertial term, the local pressure gradient can be decomposed into changes due to viscous effects from the shear stresses and inertial effects from the film expansion and contraction. Of particular interest to bulk flow models for grooved seals are the shear stresses, which represent a major source of uncertainty in the most widely used codes. With the film thickness and bulk flow pressure and axial velocity quantified, the viscous pressure gradient term can be isolated, and an effective shear stress can be defined as

$$\tau_z = \tau_{rz} + \tau_{sz} = -h\left(\frac{\partial p}{\partial z} - \frac{\partial p}{\partial z}_{iner}\right) = -h\left(\frac{\partial p}{\partial z} - \frac{\rho w^2}{h}\frac{\partial h}{\partial z}\right) \tag{2.2}$$

Note that in this effective definition, no distinction is made between the rotor and stator surfaces, and the net effect is considered. This is consistent with fully developed flow in a land section, where $\tau_{rz} \approx \tau_{sz}$. With this definition and the effective film thickness, local shear stresses can be quantified axially across the entire groove section, including at the groove to land transition region, where typical bulk flow models lump all viscous effects into a single loss coefficient.

Figure 2.9 shows the axial shear stress distribution for a sample case, here normalized by the shear stress magnitude in the land section, which remains approximately constant as expected. Apart from a slight increase in τ_z at the groove entrance, the shear stress remains approximately constant in both land sections and in the majority of the center of the groove. The interesting behavior occurs near the groove to land

transition, shown enlarged in the overlayed box. The horizontal dashed line represents $\tau_z = 0$, where any negative value for the effective shear stress indicates a local pressure recovery caused by viscous effects. A sharp increase occurs just before the end of the groove as the film begins to aggressively contract. As the film enters the land section, separates to form a vena contracta region, and recovers to the clearance level, there exists regions of positive and negative shear stress, indicating both pressure loss and recovery induced by viscous effects at different stages. While this general shape of the axial shear stress distribution remains the same throughout the data set, the magnitude and net contribution to pressure loss varies with both pressure differential and rotor speed. Analysis with an effective film thickness highlights and captures this variability that is typically approximated by a single coefficient.

Of importance, then, is the magnitude of the increase in shear stress at the transition point and the relationship between the land and groove shear stresses when operating conditions are varied. Figure 2.10 depicts the magnitudes of the land shear stress (i.e. at $z/L = 0$) and the maximum shear stress (occurring within the groove, seen as the peak of the shear stress distribution in Fig. 2.9) for a range of rotor speeds at 3 bar and 7 bar pressure differentials. Predictions based on Hirs bulk flow shear stress model [9], using empirical coefficients found suitable for rotating machinery applications [8], are also included for reference. First, note the discrepancy in magnitude when comparing the Hirs predicted values to the CFD results, highlighting the uncertainty in and sensitivity to current friction factor model coefficients and the need for shear stress modeling improvements. As rotor speed increases, land shear stress increases, a trend also seen in smooth seals and predicted by Hirs shear stress model. This is the result of the flow seeing a longer effective land length that includes the circumferential distance traveled, increasing the amount of pressure drop induced over the same physical axial length. An opposite trend occurs for the maximum shear stress, generally two orders of magnitude higher than the land shear stress, which decreases with rotor speed for both sets of results shown here. Physically, as the rotation speed imparts circumferential velocity to the flow, the expansion and contraction of the film is spread circumferentially, reducing the severity and increasing the effective length over which the film transition occurs despite the maximum penetration being higher due to centrifugal inertia effects. This inverse relationship between land and maximum groove shear stress indicates a reduction in the role of the groove at inducing a pressure drop for higher rotor speeds as the land sections shoulder more of the load.

An alternate examination of this concept can be seen when separating the pressure drop caused by the groove from that caused by the land sections, as depicted in the top of Fig. 2.11. If the model was completely

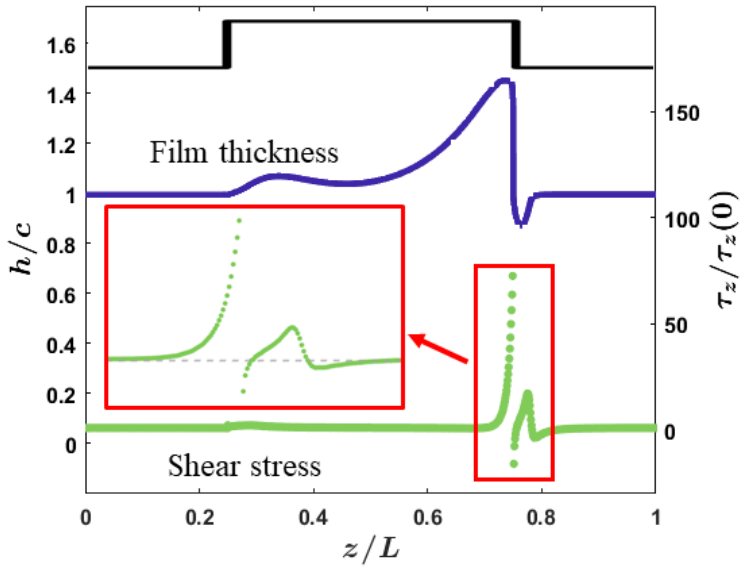

Figure 2.9: Sample shear stress distribution, with magnified view of groove to land transition region.

smooth, the pressure drop would be perfectly linear, so the vertical gap between the linear pressure profiles of the land sections represents the pressure drop induced by the presence of the groove, which includes the losses across the groove length and due to the groove to land transition described above. Lower values of $\Delta p_{gr}/\Delta p$ mean that the groove is responsible for a smaller fraction of the total pressure drop across the model.

The bottom of Fig. 2.11 shows the groove pressure drop, nondimensionalized by the prescribed single groove model pressure drop, against Re_x/Re_z and Re_{tot} for all cases, where color represents the groove pressure drop ratio value. The data appears in bands of constant rotor speed, e.g. the left most set of nine data points in a vertical line, or of constant pressure differential, e.g. the bottom most set of seven data points along a row. Groove pressure drop ratio, and the expanded area presented in the next section, are strong functions of Re_x/Re_z and Re_{tot}, with quadratic curve fits resulting in R-square values above 0.95 for both quantities. In addition to the standard Reynolds number interpretation, changes in Re_{tot} can be also considered as a change in the relative magnitude of the flow vector in the axial-circumferential plane, where the direction is described by Re_x/Re_z as discussed above. As Re_x/Re_z, or rotor speed, increases, the pressure drop ratio decreases, indicating a lesser role of the groove at inducing pressure drop and in agreement with the earlier observations of Fig. 2.10 where maximum groove shear stress decreased with rotor speed. For a constant Re_x/Re_z, an increase in Re_{tot} increases the pressure drop ratio, consistent with an increase in the maximum

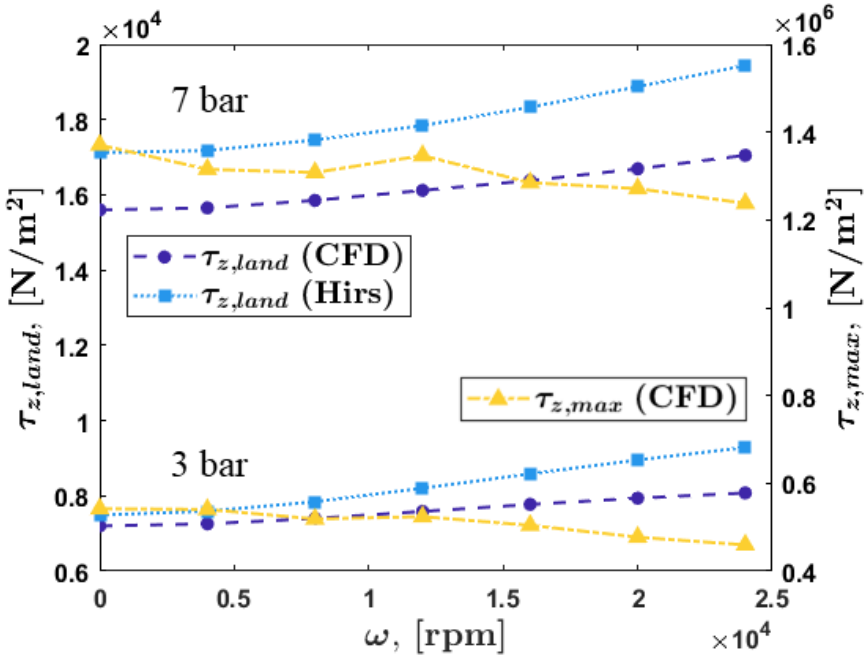

Figure 2.10: Land and maximum shear stress magnitudes for varying rotor speed at 3 bar and 7 bar.

groove shear stress as the higher axial velocity creates a sharper groove to land transition with higher shear stresses without additional circumferential smoothing.

By defining an effective film thickness, one can separate inertial effects from viscous effects in the bulk flow conservation of axial momentum, allowing for a local quantification of the viscous pressure drop caused by shear stresses. This explicitly highlights the location of maximum shear stress, namely at the groove to land transition where the effective film sharply contracts, and enables a direct comparison between the pressure drop caused by land and groove sections.

2.3.3 Expanded Area

With changes in film thickness and seal behavior explained physically by a local analysis of the shear stress, a quantitative metric for the net flow expansion into the groove is presented to create a full description of the seal flow and its relationship to leakage performance.

The net expansion of the film into the groove was quantified by defining the expanded area, A_{exp}, the integrated area under the effective film thickness that has penetrated into the groove, plus the area above the film thickness that represents the vena contracta effect at the groove to land transition point. The top of Fig. 2.12 depicts this quantity in the shaded green region. This definition includes the effects of both the

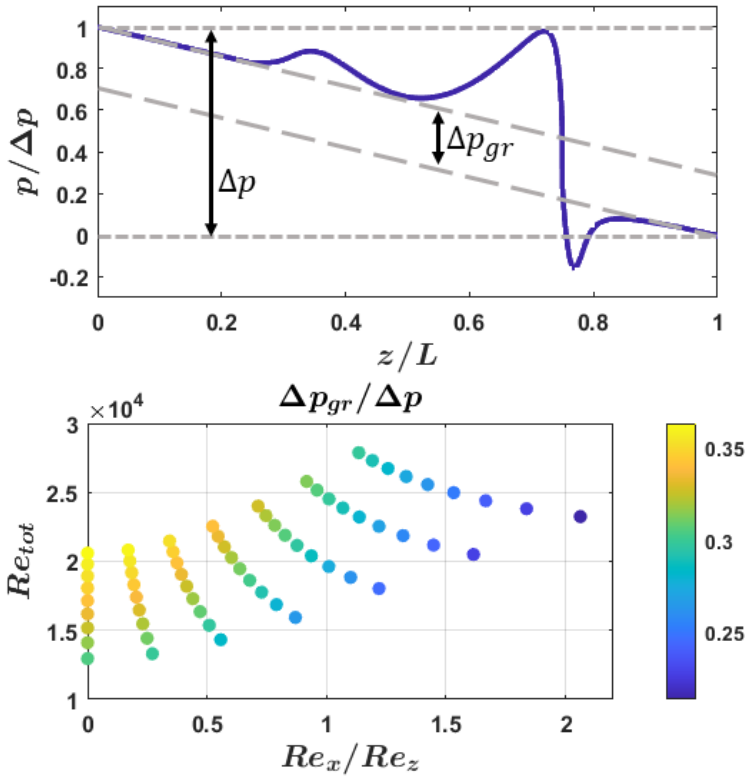

Figure 2.11: Top: Depiction of groove pressure drop, Δp_{gr}. Bottom: Groove pressure drop ratio vs. Re_x/Re_z and Re_{tot} for all cases.

expansion into the groove over the groove length and the groove to land transition vena contracta, which has previously been shown (see Fig. 2.9) to be an area of importance in terms of viscous pressure drop. The bottom of Fig. 2.12 shows the expanded area, nondimensionalized by the area of the groove ($L_g \times D_g$), for all cases. With this explicit quantification of the expansion, note the correspondence to the film thickness trends presented in Section 2.3.1, namely the increase in expanded area with Re_x/Re_z due to centrifugal inertia and circumferential spreading.

Figure 2.13 shows the model leakage, a major quantity of interest in bulk flow modeling of seals, as a function Re_x/Re_z and Re_{tot} for all cases. Note that an appropriate factor was applied to transform the sector model leakage into its full circumference equivalent. As expected, leakage increases with Re_{tot} (pressure differential) and decreases with Re_x/Re_z (rotor speed). Comparison between Figs. 2.11 - 2.13 describes the mechanisms by which leakage changes and its relationship to the shape and behavior of the film thickness. When Re_x/Re_z increases, the film expands further into the groove, but this expansion is spread circumferentially leading to less groove induced pressure loss. The corresponding increase in land shear

stress at higher Re_x/Re_z is thus the driving mechanism behind leakage reduction at higher rotor speeds, overcoming the loss in pressure drop caused by the groove. When Re_{tot} increases, the change in expanded area is minimal but the transition is sharper, increasing pressure drop caused by the groove, though leakage still increases because of the higher pressure differential.

The choice of the expanded area as a metric to quantify net changes in film thickness is in clear physical agreement with the results presented for the flow patterns and shear stress. Its use helps bridge the gap between the observance of qualitative flow changes and performance changes at different operational conditions, demonstrating its importance as a quantity of interest in bulk flow analysis using an effective film thickness.

2.3.4 Groove Aspect Ratio

Geometric considerations play an important role in seal performance and design. Using the same analysis tools that were presented in Sections 2.3.1, 2.3.2, and 2.3.3 as the foundation, the effect of groove geometry on seal behavior is now examined, including a suggested aspect ratio range based on flow expansion considerations.

An additional set of single groove simulations were run with constant operating conditions, $\omega = 10.2$ krpm and $\Delta p = 4.14$ bar, where the groove depth was modified to adjust the groove aspect ratio, defined as $AR = D_g/L_g$. The groove length was held constant at $L_g = 1.587$ mm to match the experimental geometry consisting of square grooves. Aspect ratios between 0.01 and 3 were examined. Film thickness, shear stress, groove pressure drop ratio, and expanded area were quantified as in previous sections and their analysis is the subject of this section.

Figure 2.14 shows the effective film thickness for grooves with AR ranging from $AR = 0.07$ (where $D_g = c$) to a square groove with $AR = 1$. The net film expansion is the highest for the groove with $AR = 0.07$, initially expanding fast and encompassing most of the groove area (note that when $AR = 0.07$ and $D_g = c$, a value of $h/c = 2$ is the full radial extent of the groove). As the groove gets deeper, the film begins to squeeze towards the downstream groove wall as a recirculating region begins to form. A minimum expansion is observed when $AR = 0.76$, where the groove vortex has sufficient strength and size to extend partially outside of the groove and actually depress the film. Further increasing the AR sees the vortex retreat into the continually expanding groove area, accompanied by a final minor increase in the expansion. Film thicknesses at $AR > 1$ show minor fluctuations about the film at $AR = 1$ as multiple vortices begin to form in the deeper grooves in a cyclic pattern. Film thicknesses for the shallowest grooves ($AR < 0.07$) show a shape similar to

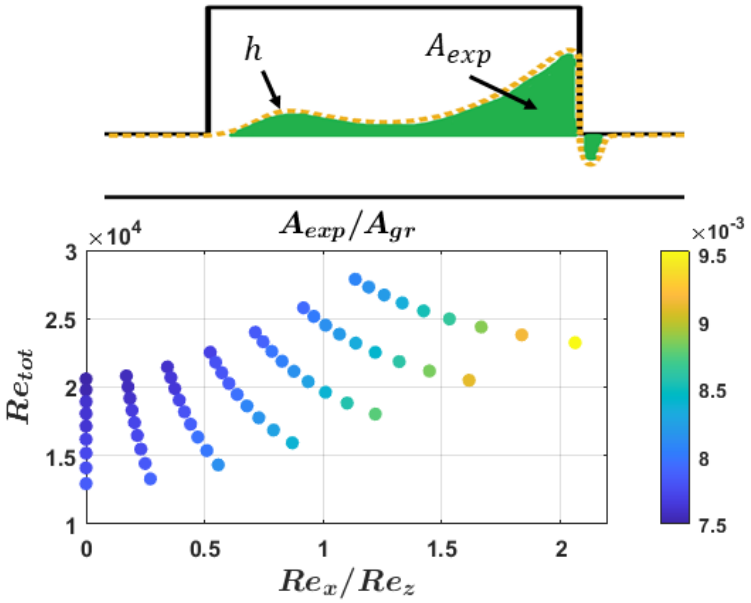

Figure 2.12: Top: Depiction of expanded area, A_{exp}. Bottom: Nondimensional expanded area vs. Re_x/Re_z and Re_{tot} for all cases.

the $AR = 0.07$ case, where initial expansion is early and reaches the full groove depth, encompassing the majority of the groove area.

A comparison of leakage (full circumference equivalent), groove pressure drop ratio, and expanded area (dimensional) for $AR = 0.01$ - 2 is shown in Fig. 2.15. All three quantities are approximately constant for $AR > 2$ and are not shown here. For extremely shallow grooves, or small AR, the leakage rises above that of a smooth seal without any groove, with the small increase in area acting as an effective increase in clearance. Grooves with any appreciable depth are seen to decrease the leakage in relation to the smooth seal, as expected.

The groove pressure drop ratio is almost perfectly inversely related to leakage. Since operating conditions are held constant, this indicates that in order to minimize leakage, the primary goal should be to maximize the pressure drop caused by the groove, as seen by the minimum leakage AR data point corresponding to the region of maximum groove pressure drop ratio. This also means that the pressure drop induced by the land sections should be minimized, an intuitive result since lower land shear stresses correspond to lower axial velocities, as in smooth seals.

A comparison to the expanded area shows that net film expansion is a driving force behind leakage reduction when groove geometry is changed. For $AR > 0.15$, expanded area is directly proportional to

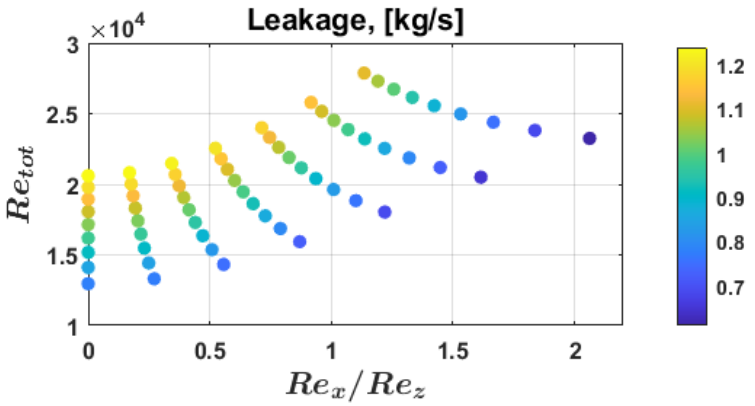

Figure 2.13: Leakage (full circumference equivalent) vs. Re_x/Re_z and Re_{tot} for all cases.

groove pressure drop ratio, and thus inversely proportional to leakage. Since operating conditions are held constant, increased film penetration means sharper transitions from groove to land and thus higher groove shear stresses without the circumferential smoothing effect and increased land shear stresses that occur with increased rotor speed. Interesting behavior occurs for $AR < 0.15$. First, note that the decrease in expanded area with decreasing AR for the shallowest grooves is due to geometric constraints. As mentioned above, the shallowest grooves have a film that encompasses the majority of the groove and will eventually have a decreasing dimensional expanded area once the film expands to the full groove depth. We also note that the minimum leakage point, where $AR = 0.13$, does not directly correspond to the maximum expanded area, where $AR = 0.07$. A physical explanation lies in a comparison of the film thicknesses for these two data points in Fig. 2.14. When $AR = 0.07$, the film expansion takes up so much of the groove area that there is minimal room for a recirculating region to also be present. When $AR = 0.13$, the film expands almost as deep, leading to a similar severity of contraction at the land to groove transition, but the area left in the groove is enough to anchor a larger recirculation region. This larger recirculation region increases the viscous pressure losses earlier in the groove section while maintaining large losses at the groove to land transition, leading to a minimum leakage result. This suggests a potential design criteria when optimizing grooved seal geometry to minimize leakage, namely to choose a geometry that maximizes expanded area while still allowing for the presence of a recirculation region. The current data suggests this occurs when the groove aspect ratio is between 0.07 and 0.19. A design of experiments presented by Morgan et al. [31] sought an optimal groove geometry by performing regression on leakage results from simulations with varying complex groove shape features. Flow fields for the optimal groove geometries, with aspect ratios between 0.085 and

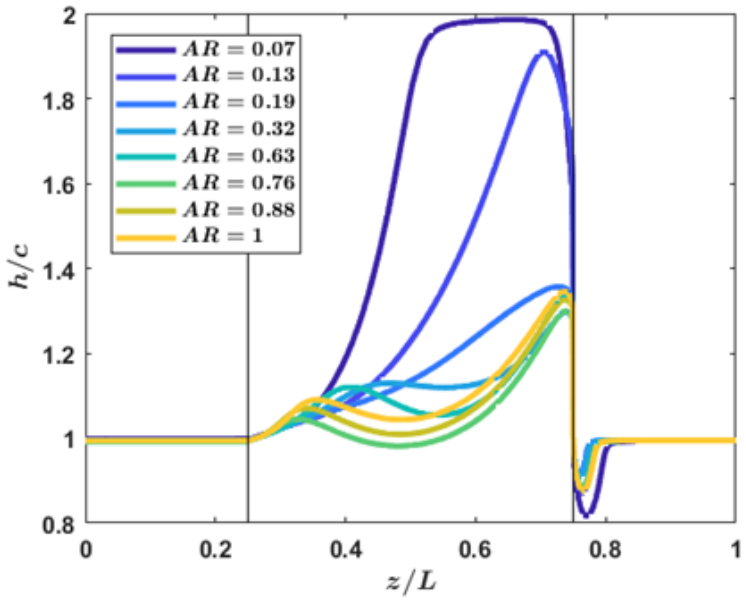

Figure 2.14: Film thickness for various groove aspect ratios.

0.132, show the same physical film thickness behavior of maximum (full groove) penetration that maintains a recirculation region, despite the additional geometric complexities. It is hypothesized that similar reasoning will lead to correlations between expanded area and seal stability criteria.

Analyzing the film thickness, groove pressure drop ratio, and expanded area across cases with various groove aspect ratios has lead to a clear physical explanation for the case with minimum leakage backed by quantitative results, namely corresponding to the largest groove induced pressure drop and most film expansion that includes a recirculation region. This demonstrates the use of effective film thickness based analysis as a valuable tool for providing geometric design insight for grooved seals.

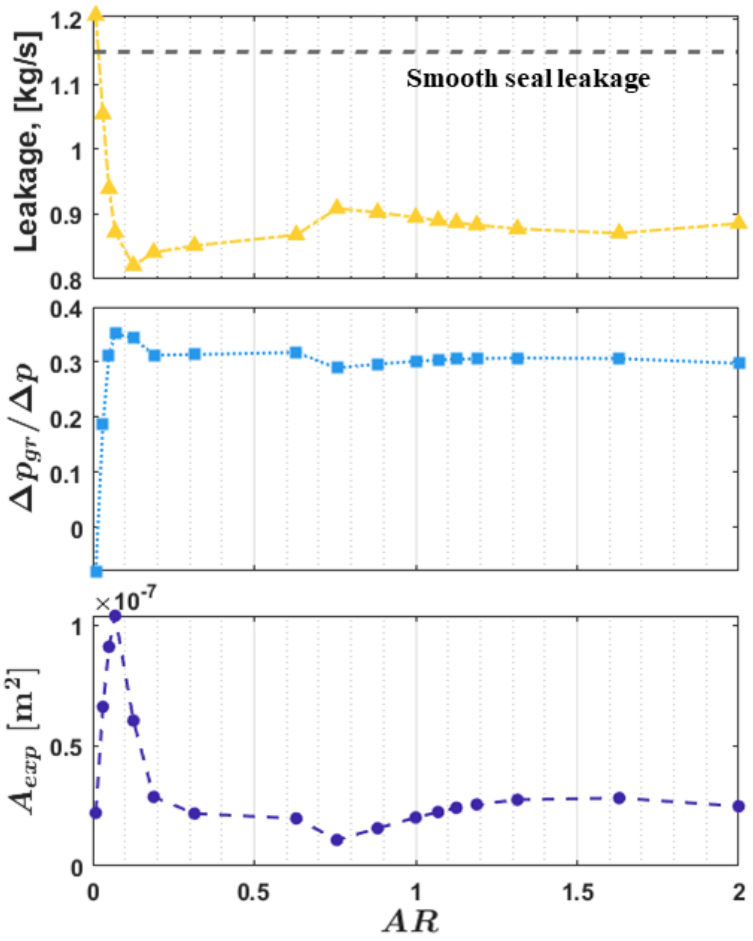

Figure 2.15: Top to bottom: Leakage (full circumference equivalent), groove pressure drop ratio, and expanded area vs. groove aspect ratio.

2.4 Discussion

The combination of the quantitative metrics of groove pressure drop and expanded area in Sections 2.3.2 and 2.3.3, along with the qualitative description of the flow patterns presented in Section 2.3.1, provide a full description of seal behavior, including the driving mechanisms behind changes in leakage performance at different operating conditions. While reductions in leakage at higher rotor speeds is well documented, the role of the groove compared to the land sections is given much less attention. The use of an effective film thickness in bulk flow analysis allows this comparison to be explicitly quantified and shows a lesser role of the groove at higher circumferential to axial Reynolds number ratios. This same analysis also lead to the identification of an optimal groove aspect ratio range for minimum leakage, now grounded by a physical explanation where expanded area should be maximized while retaining a recirculating region such that the

groove pressure drop ratio is maximized. While generally in agreement with bigger data approaches, this physical intuition arose naturally from the effective film thickness based analysis.

The local quantification of the shear stress, detailed in Section 2.3.2 and depicted in Fig. 2.9, adds necessary precision to an inherently empirical and uncertain component of bulk flow modeling. Figure 2.16 shows the pressure loss due to viscous forces, comparing the impact of the effective shear stress used in this paper to traditional shear stresses based on Hirs definition. Note that, following Eqn. 2.1, $(dp/dz)_{visc} = -\tau_z/h$ and that the y-axis is shifted by the single groove pressure differential such that the integrated pressure loss at the model outlet is zero. Bernoulli effects due to film expansion and contraction are not included in Fig. 2.16 to highlight the effect of the viscous forces on pressure loss. While the pressure loss in the land sections is comparable and the slopes in Fig. 2.16 are similar in these regions, the increase in losses at the groove entrance and the complex loss behavior at the groove to land transition are observed only when the effective shear stress is employed without the need for an additional empirical loss coefficient. This quantification of the effective shear stress has also revealed a remarkably consistent shape for the shear stress profile, which, when combined with the demonstrated increase in precision, creates an avenue for marked improvement in shear stress bulk flow modeling through a more physical profile at the jet flow recirculating flow interface.

All quantities can be described by the circumferential to axial Reynolds number ratio and total Reynolds number, which can be interpreted as the direction and relative magnitude, respectively, of the bulk flow velocity vector in the axial-circumferential plane. This forms the basis for a modeling structure to improve bulk flow methods for grooved seals that traditionally suffer from a need for a number of well tuned empirical coefficients. A more accurate identification of the role of the groove through the groove pressure drop ratio and through an updated shear stress profile can lead to a more physical mechanism for modeling the additional losses at the groove to land transition typically captured by loss coefficients, possibly eliminating the need for a loss coefficient altogether. Thus, the analysis presented here backed by the effective film thickness has the capability to address some of the largest areas of uncertainty in current bulk flow models for grooved seals.

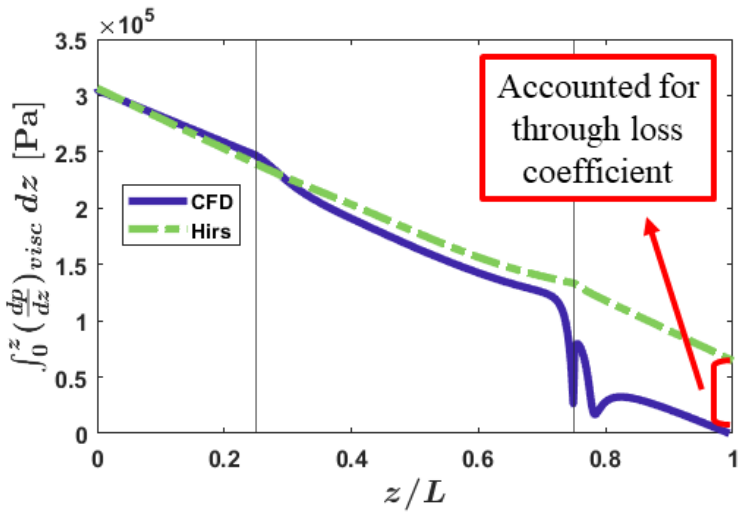

Figure 2.16: Comparison of the cumulative viscous pressure loss due to the effective shear stress from the present results and shear stresses predicted by a traditional Hirs definition.

2.5 Conclusion

This paper presents the first quantitative analysis of an effective film thickness in circumferentially grooved seals that captures flow features and effects previously neglected in bulk flow theory and modeling. A single groove seal CFD model is constructed, and simulations were run for a range of pressure differentials and rotor speeds. The effective film thickness is found by calculating the radial-most streamline in the jet flow region, leading to the quantification of the flow patterns, local shear stress, and expanded area. Net expansion into the groove depends predominantly on the circumferential to axial Reynolds number ratio. For constant geometry and variable operating conditions, decreases in leakage with higher circumferential to axial Reynolds number ratio are found to be dominated by increases in land shear stresses, where the influence of the groove on pressure drop is lessened. When operating conditions are held constant and the flow is subjected to changes in groove geometry only, decreases in leakage correspond directly to increases in net expansion and groove pressure drop ratio, indicating the predominance of film thickness behavior over changes in leakage. An optimal aspect ratio range is suggested between 0.07 and 0.19 based on maximum expanded area that retains a recirculation region within the groove.

Use of an effective film thickness more faithfully describes the physical nature of the flow in circumferentially grooved seals and provides a platform for a more fundamental exploration into the mechanisms dictating the flow, as described herein. Analyzing local changes in film thickness and flow variables has

highlighted modeling areas that can be improved when a more physical approach is taken. Effective film thickness based analysis can foster new model development to capture those local variations, such as an updated shape of the axial shear stress distribution that accurately captures the groove to land transition losses. This development inherently includes the fundamental flow information presented in this paper, reducing empiricism and potentially eliminating particular coefficients from bulk flow models entirely. The present results are a necessary and significant step in the sequential development of improved bulk flow predictions where a novel modeling approach has been defined and its use has provided insight into grooved seal flow fields and performance and established physical relationships between critical bulk flow modeling components. By directly addressing some of the main sources of uncertainty in current bulk flow codes, these modeling changes based on an effective film thickness have the capability to drastically improve the accuracy of bulk flow predictions for circumferentially grooved seals.

Chapter 3

Form Shear Stress Modeling

The corresponding manuscript title for this chapter is ”Form Shear Stress (FSS) Correction in Bulk Flow Analysis of Grooved Seals Based on Effective Film Thickness.” The manuscript has been submitted to the *ASME Journal of Tribology* for publication at the time of dissertation writing.

Nomenclature

$\dot{m}$	Leakage	ρ	Density
N	Number of grooves	μ	Kinematic viscosity
p	Pressure	AR	Groove aspect ratio
u, w	Circumferential, axial velocity	Re	Reynolds number
$x(\theta), z$	Circumferential, axial direction	τ	Shear stress
ω	Rotor speed	λ	Friction factor
U	Relative velocity	h	Effective film thickness
R	Rotor radius	L	Model length
c	Clearance	ξ	Loss coefficient
Δp	Pressure differential		

Subscripts

tot	Total resultant	l	Land
r, s	Rotor, stator	g	Groove

3.1 Introduction

Annular seals are commonly employed in various turbomachines to reduce leakage flow across a region with a large pressure differential. A balance piston in a multistage pump, for example, equilibrates the entire pump pressure rise while restricting leakage. Through the addition of circumferentially cut grooves on the rotor or stator surface, leakage can be further reduced at the expense of more complex flow fields and difficulty in predicting the dynamic response. Annular seals are known to have a significant impact on overall turbomachine performance, efficiency, and stability, making their analysis critical to design efforts [3]. The need for accurate and efficient analysis methods for annular seals remains strong as turbomachine design continues to push the boundaries of operating conditions and efficiency.

Modern seal analysis includes both simplified bulk flow methods and full computational fluid dynamics (CFD) studies for the prediction of leakage and rotordynamic coefficients to quantify the steady state performance and dynamic response of the seal. Continual advancements in computational capability and resources has led to an increase in use and development of fully three-dimensional seal analysis methods. For example, Wu et al. [32] utilized higher fidelity CFD methods to analyze the influence of gas content on rotordynamic performance of grooved seals as a complementary effort to a series of experiments. The authors identified a potential rotordynamic coefficient excitation frequency dependence for higher gas volume fractions. Using a fully transient CFD method, Li et al. [33] examined the effect of static and dynamic eccentricity on rotordynamic coefficient predictions, finding a small but non-negligible sensitivity to whirl amplitude only at higher static eccentricities. While studies such as these are becoming increasingly common, the setup complexity and computational effort required to ensure accurate and reliable results from full CFD methods remains a challenge, creating a need for continued development of simplified and efficient alternatives such as bulk flow methods, which is the focus of this paper.

Bulk flow methods typically utilize Hirs turbulent thin film theory [9] in a series of control volumes (CV) along with radial averaged quantities and a circumferential perturbation assumption to simplify the inherently three dimensional flow down to a single dimension. In doing so, a number of empirical coefficients are typically introduced to model various flow effects. Blasius type friction factors, for example, are often employed to capture the effect of shear stresses on the rotor and stator surfaces as empirical functions of local Reynolds number. Grooved seals add additional flow field complexity due to the formation of a recirculation region and its interaction with the clearance flow. This further increases the reliance on empirical coefficients

and the uncertainty of the overall method. Various efforts have taken place to effectively capture the additional effects of the groove region within bulk flow methods, specifically targeting the groove shear stresses due to their high input uncertainty. In an early method for liquid grooved seals, Nordmann et al. [20] used an average depth and different friction factors on each surface within a single CV to generate rotordynamic coefficient predictions that qualitatively matched those of the experiments for an eight groove seal. Through the addition of a second CV and a loss coefficient at the end of the groove, Iwatsubo and Sheng [21] attempted to differentiate between the groove and clearance flows leading to qualitatively accurate trends but overpredicted coefficients. A method frequently discussed and considered in the literature is that of Marquette and Childs [24] that featured three CVs where the shear stresses at the interface between the clearance and recirculating flow followed the work of Wyssmann et al. [34] based on Prandtl's mixing length model. This method also featured a groove loss coefficient while incorporating a linear film penetration approximation within the groove region. While this three CV method intuitively provides the best physical approximation to the flow, the strong prediction accuracy reported by Marquette and Childs required a number of well tuned empirical coefficients. A different approach was taken by Han et al. [35], who used a modified control volume definition to develop semi-empirical analytical equations to predict leakage and tooth clearance pressure for straight-through liquid labyrinth seals. This yielded accurate flow rates as compared to CFD results for a cryogenic machine tool liquid nitrogen spindle seal case, though the analysis needed a number of its own empirical coefficients, some of which were taken from previous bulk flow studies.

The issue with numerous empirical coefficients in grooved seal bulk flow modeling is discussed by Frêne et al. [36] when considering the difficulty in modeling inertia effects in high Reynolds number bearings and seals. They noted that that three CV methods are only effective if the empirical coefficients can be well defined. More recent efforts have utilized CFD in various manners to improve the values used for some of these coefficients or directly identify the magnitude of the shear stresses themselves. Migliorini et al. [11] used CFD to define the steady state solution, including shear stress data, for use in a bulk flow perturbation method for rotordynamic coefficient prediction in a full hybrid method. San Andrés et al. [12] extracted friction factor and streamline penetration angle data from CFD simulations for use in a modified hybrid-type three CV bulk flow method and achieved reasonable prediction accuracy compared to CFD results, with Wu and San Andrés [25] later extending this analysis to triangular and scalloped groove geometries. A similar approach was taken by Wu and San Andrés [37] for gas labyrinth seals, again seeking updated values for friction factor coefficients as functions of operating conditions. While CFD has proven to be a valuable tool

for reducing the uncertainty in some empirical coefficients, the continued reliance on fitting these coefficients to particular seals or cases calls attention to the limitations of current grooved seal bulk flow shear stress modeling methods.

Also contributing to the prediction of the influence of the grooves in many bulk flow methods is the groove loss coefficient, analogous to an inlet loss coefficient at the seal inlet plane. Despite its frequent use, little work has been done to quantify its influence on prediction results and address its uncertainty, despite similar interest in the inlet loss coefficient. Yang and San Andrés [38] investigate the effects of geometric curvature at the seal inlet plane of a smooth seal CFD model, noting that the inlet loss coefficient does not depend on pressure differential or rotor speed, but does vary significantly with preswirl ratio. They also note a decrease in direct stiffness and damping with decreasing inlet loss coefficient as the inlet corner is rounded, highlighting the sensitivity of the loss coefficient to seal conditions, and ultimately of bulk flow rotordynamic coefficient predictions to loss coefficient values. In a numerical method for predictions of static characteristics of helical grooved seals, Nagai et al. [39] employ a loss coefficient formulation, developed by Constantinescu and Galetuse [40] for step bearing analysis, to account for pressure drop effects due to sudden contractions, leading to qualitatively reasonable predictions of the pressure variations within the groove region. Despite such evidence suggesting that the groove loss coefficient is an uncertain and impactful parameter, bulk flow models often assume a standard value, typically 0.1, or match it to the inlet loss coefficient without sufficient justification. Grooved seal bulk flow modeling continues to rely on significant assumptions regarding the groove flow field and on heavy empiricism when accounting for the influence of the shear stresses, as in the use of a groove loss coefficient. A new modeling approach is thus desired to address these shortcomings that lead to inaccurate predictions.

Recent work by the present authors in Ref. [13] quantified an effective film thickness, a physical flow boundary that separates the clearance flow from the recirculating flow based on real flow expansion and contraction, for use in bulk flow analysis of grooved seals. By using a modified CV definition based on the effective film thickness, physical flow information was inherently included in the analysis. This allowed for a detailed examination of the relationship between the flow field, effective film thickness, and steady state performance. Reference [13] also highlighted the opportunity for improved shear stress modeling through a more physical analysis approach. The results created a platform for reduced empiricism and the potential elimination of particular empirical coefficients in grooved seal bulk flow modeling, though an explicit determination of the groove shear stresses was still desired. The present work seeks to build on

those efforts by directly quantifying the shear stress contributions within the groove region through that same effective film thickness analysis framework. By leveraging single groove CFD simulation data and the effective film thickness, the additional shear stresses within the entire groove region can be identified as a correction to traditional shear stress models. This correction is labeled as a form shear stress (FSS) based on the clear relationship between the behavior of the additional shear stresses and the shape, or form, of the effective film thickness. Given the limitations in bulk flow shear stress modeling for grooved seals identified above, this paper has the following objectives: 1) isolate and quantify the additional form shear stress component within the groove region using effective film thickness based analysis, 2) generate axial and circumferential form shear stress models for efficient implementation into current bulk flow methods, 3) demonstrate the utility of the novel form shear stress models at providing accurate predictions of physical flow features and reducing empiricism in bulk flow methods for grooved seals. The third objective is addressed through the use of additional single groove and full seal CFD results to assess the predictive capability of the FSS models and through implementation of the FSS models into a simplified bulk flow method. This is the first time that an effective film thickness foundation has been utilized to directly quantify and model the additional groove shear stresses. The novel shear stress modeling approach in this paper is adaptable and applicable to a wide array of seal scenarios through an extension of the parameter range considered here or the consideration of additional parameters relevant to a particular application. The present methodology thus provides an avenue for widespread and significant improvements to bulk flow model prediction accuracy for grooved seals.

The remainder of this paper is structured as follows. First, the single groove CFD model used to generate simulation data is described, and the analysis procedure used to isolated and quantify the FSS components is detailed. The axial and circumferential FSS ratios are examined across a range of groove geometries and operating conditions, ultimately leading to predictive models for the shear stress ratios as functions of two Reynolds number quantities. The prediction accuracy of the models is then assessed through single groove and full seal CFD simulation data for additional seal cases. Lastly, the FSS models are implemented into a simplified bulk flow method to demonstrate the utility of the present modeling approach, followed by concluding remarks.

3.2 Methodology

The computational methods and analysis procedures employed in this paper are outlined in this section, beginning with a brief description of the single groove CFD model used to generate the core simulation data set. The isolation and extraction of the form shear stress component is then detailed. This establishes a foundation for the proposed form shear stress modification to bulk flow methods for grooved seals.

3.2.1 CFD Modeling

The computational methodology employed in this study follows that of the author's previous work in Ref. [13], where the effective film thickness was first quantified and used for grooved seal analysis. Details relevant to the current study are reported here for clarity and continuity, though the reader should refer to Ref. [13] for a complete discussion on model setup, parameters, mesh independence, and direct quantification of the effective film thickness upon which the present analysis builds.

The base seal model used in this study follows the geometry of the finely-grooved seal in the experimental work by Marquette et al. [29], and the geometry of the full seal is summarized in Table 3.1. The CFD model used to generate film thickness and FSS simulation data is of a single groove, where the land sections on either side of the groove are $L_l/2$ in length. Table 3.1 also includes details on two additional seals based on experiments by Iwatsubo et al. [41] and Nordmann et al. [20]. These seals are used to develop both single groove and full seal CFD results to assess the performance of the FSS models, to be discussed below.

The single groove CFD model is depicted in Fig. 3.1. The model consists of a single seal groove with half of a land section on either side. A 0.05 degree circumferential sector model and a circumferential interface are employed to leverage the axisymmetry of a seal in centered (unperturbed) operating conditions and significantly reduce the computational domain to aid in meshing and required computational resources. An axial interface with a prescribed pressure change is employed at the model inlet and outlet to represent a fully developed seal groove sufficiently downstream of the seal inlet plane. A steady-state simulation delivers the flow field used to define the effective film thickness, depicted in Fig. 3.2. Radial averaging across the film delivers the local bulk pressure and velocities used to quantify the FSS components, to be described below. A summary of the CFD modeling setup and boundary conditions is given in Table 3.2.

A two-step convergence method was used to ensure full convergence to steady state results for each simulation, particularly regarding the flow fields within the groove region. Mesh independence for the single

Table 3.1: Geometry and fluid property details of the seals considered in this study.

	Marquette et al. [29]	Iwatsubo et al. [41]	Nordmann et al. [20]
ρ [kg/m^3]	984.5	997	997
μ [kg/m s]	0.0005	0.001	0.000798
L [mm]	34.925	35.2	23.5
R [mm]	38.252	35.2	23.5
c [mm]	0.1105	0.175	0.2
L_g [mm]	1.587	1.6	0.7
D_g [mm]	1.587	1.2	0.5
L_l [mm]	1.587	1.6	1.5
N	10	11	8

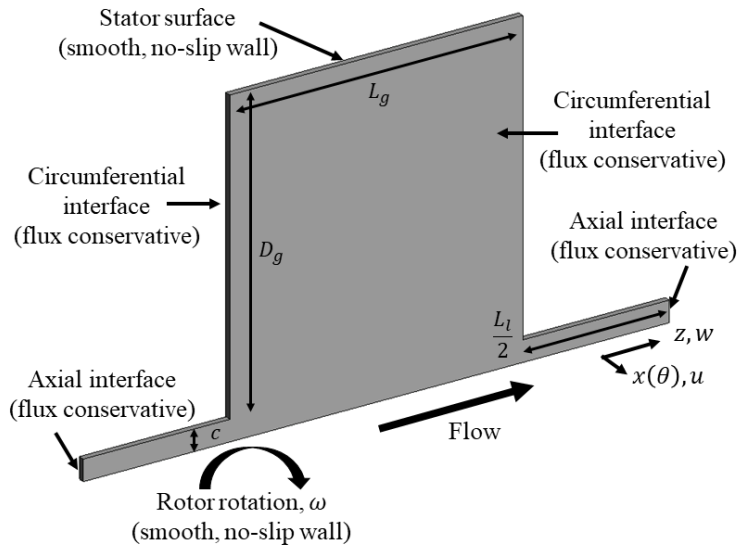

Figure 3.1: Baseline geometry and CFD setup for the single groove seal model, including boundary conditions.

groove model, not included here for brevity, was verified using a series of grids with increasing number of elements where less than 1% difference in leakage was observed across the set of grids. A visual examination of the cross-film and cross-groove velocity profiles was also conducted to confirm mesh independent results. The Shear Stress Transport (SST) turbulence model [30] was employed, where all grids were sufficiently refined near walls and verified to have $y+ < 5$ everywhere. Simulations were performed using ANSYS CFX v. 2021 R1 [42].

Several sets of simulation data were generated in order to isolate and determine the effect of various quantities on the FSS bulk flow component targeted in this study. Based on previous results and preliminary analysis, the authors identified the ratio of circumferential to axial Reynolds number, Re_x/Re_z, the total

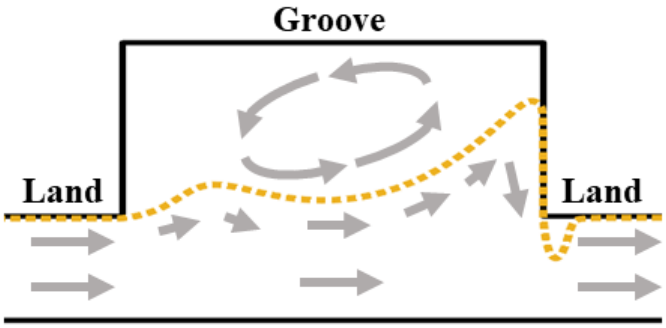

Figure 3.2: Diagram of the effective film thickness for a single groove, shown as the yellow dotted line.

Table 3.2: Details of the CFD setup for the single groove model.

Working fluid	Water
Turbulence model	SST
Thermal treatment	Isothermal (adiabatic walls)
Circumferential interface	Rotational periodicity
Axial interface	Translational periodicity with pressure change
Convergence criteria	Global 1e-10 RMS
Conservation target	1%

resultant Reynolds number, Re_{tot}, and the groove aspect ratio, AR, as primary quantities of interest dictating physical flow behavior. The Reynolds number is defined in this work as $Re = 2c\rho V/\mu$, where V is the bulk flow velocity equal to u, w, or $\sqrt{u^2 + w^2}$ for the circumferential, axial, and total quantities, respectively. The hydraulic diameter, $2c$, is used as the characteristic length in accordance with standard seal analysis. Note that Re_x/Re_z is equivalent to the ratio of circumferential to axial velocity, a kinematic characteristic of the flow. The two Reynolds number quantities help describe the relative magnitude and direction of the bulk flow vector in the axial-circumferential plane. These three primary quantities thus account for the effects of the flow direction in relation to the circumferential direction of the grooves as well as groove geometry. Six data sets, summarized in Table 3.3, were generated to explore the space in these three variables. The first three sets employed a fixed groove geometry and varied operating conditions to investigate the influence of the Reynolds numbers. The deep data set in Table 3.3 represents the base case geometry and best matches the experimental fluid properties and operating condition ranges for the finely-grooved seal in Ref. [29]. The shallow and middle data set geometries were chosen based on seal cases with similar geometry in the literature. The last three sets fixed the operating conditions and varied AR to isolate geometric effects in

different regions of the Reynolds number space. The AR range was selected to encompass typical groove depths and to extend to depths where the cyclic behavior of additional recirculation regions with increasing depth could be observed. Note that fluid temperature, specified through adjustments to the fluid density and viscosity, was also varied to achieve certain relevant Reynolds number ranges. Across the single groove simulation cases shown in Table 3.3, Re_x/Re_z varies from 0 to 2.5, Re_{tot} from 4,000 to 20,000, and AR from 0.01 to 3.

3.2.2 Form Shear Stress (FSS) Quantification

Having established a series of simulation data sets using the single groove CFD model, the form shear stress component is then isolated and quantified in order to analyze its variation with the primary quantities of interest. This section outlines the analysis procedure used to quantify this additional bulk flow form shear stress term.

As described above, the behavior and influence of the shear stresses within the groove region is difficult to quantify, typically requiring a number of approximations and empirical coefficients, such as the groove loss coefficient. Motivated by the clear link between the behavior of the effective film thickness and the pressure loss across a groove as described in Ref. [13], this work seeks to isolate and quantify the additional shear stresses within the groove region. The analysis stems from the continuity and conservation of axial and circumferential momentum equations for an incompressible fluid given in Eqns. 3.1 - 3.3 following Ref. [3] as

$$\frac{\partial w}{\partial z} = -\frac{w}{h}\frac{\partial h}{\partial z} \tag{3.1}$$

$$\frac{\partial p}{\partial z} = -\frac{1}{h}(\tau_{rz} + \tau_{sz}) + \frac{\rho w^2}{h}\frac{\partial h}{\partial z} \tag{3.2}$$

$$\frac{\partial u}{\partial z} = -\frac{1}{\rho h w}(\tau_{r\theta} + \tau_{s\theta}) \tag{3.3}$$

The equations as presented are formulated for smooth seals or land sections where the axial gradient terms are retained so that the effective film thickness can be employed. This work targets the shear stress terms, τ, in both the axial and circumferential directions and seeks to improve their formulation within the grooves. Within a land section or for a smooth seal, the shear stresses are considered well approximated quantities

Table 3.3: Geometry, fluid properties, and operating conditions for the single groove simulation sets used in the FSS analysis. All conditions are modified cases of the base case seal in Marquette et al. [29].

Data Set	AR	ρ [kg/m^3]	μ [kg/m s]	ω [krpm]	Δp [bar]
Shallow	0.07	997	0.0008899	0 - 24	3 - 7
Middle	0.76	1000	0.00131	0 - 24	3 - 7
Deep	1	984.5	0.0005	0 - 24	3 - 7
AR set 1	0.01 - 3	984.5	0.0005	10.2	4.14
AR set 2	0.01 - 3	1000	0.00131	4	4
AR set 3	0.01 - 3	993	0.00069	24	3

and modeled following Hirs bulk flow formulation [9] that employs a Blasius type friction factor model. Following this definition, the friction factors are defined as empirical functions of local Reynolds number as

$$\lambda_{r,s} = aRe_{r,s}^{-B} \qquad Re_{r,s} = \frac{2c\rho U_{r,s}}{\mu} \tag{3.4}$$

where the empirical coefficients $a = 0.0674$ and $B = 0.217$ were selected in the present study to be suitable for rotating machinery [8]. The shear stresses on the rotor and stator surface are then modeled as functions of the friction factors and the local velocity relative to the respective surface, $U_r = \sqrt{w^2 + (u - \omega R)^2}$ and $U_s = \sqrt{w^2 + u^2}$, as

$$\tau_r = \frac{1}{2}\rho\lambda_r U_r^2 \qquad \tau_s = \frac{1}{2}\rho\lambda_s U_s^2 \tag{3.5}$$

The shear stresses act in directions opposite the relative velocity and have axial and circumferential components given by

$$\tau_{rz} = \tau_r \frac{w}{U_r} \qquad \tau_{sz} = \tau_s \frac{w}{U_s} \qquad \tau_{r\theta} = \tau_r \frac{(u - \omega R)}{U_r} \qquad \tau_{sz} = \tau_s \frac{u}{U_s} \tag{3.6}$$

This shear stress formulation is widely employed in seal bulk flow analysis methods and provides industry accepted solutions for smooth seal cases.

The influence of the grooves on the behavior of the bulk pressure and circumferential velocity, according to Eqns. 3.2 and 3.3, is most notably accounted for through modified shear stress definitions within the groove region. The work in Ref. [13] provides a framework for isolating the bulk flow shear stress components in the conservation of momentum equations by utilizing the effective film thickness. The present work builds on this analysis by considering the influence of the groove on the shear stresses as a correction to the traditional

Hirs shear stress definition that is well suited for smooth seals or land sections. The authors term this a form shear stress correction based on the clear qualitative relationship between the shape, or form, of the effective film thickness and the axial location of additional shear stress behavior, as described below.

Using the effective film thickness approach, modified bulk flow conservation of axial and circumferential momentum equations are considered as

$$\frac{\partial p}{\partial z}_{total} = \frac{\partial p}{\partial z}_{Hirs} + \frac{\partial p}{\partial z}_{form} + \frac{\partial p}{\partial z}_{inertia} = -\frac{1}{h}(\tau_{rz} + \tau_{sz} + \tau_{z,form}) + \frac{\rho w^2}{h}\frac{\partial h}{\partial z} \tag{3.7}$$

$$\frac{\partial u}{\partial z}_{total} = \frac{\partial u}{\partial z}_{Hirs} + \frac{\partial u}{\partial z}_{form} = -\frac{1}{\rho h w}(\tau_{r\theta} + \tau_{s\theta} + \tau_{\theta,form}) \tag{3.8}$$

where the additional groove shear stress terms, $\tau_{z,form}$ and $\tau_{\theta,form}$, are quantified in this paper. Applying effective film thickness based analysis to the single groove simulation data allows direct quantification of the total axial gradients of pressure and circumferential velocity, the left-hand-side terms of Eqns. 3.7 and 3.8, as well as the inertial pressure gradient term due to film expansion and contraction. The Hirs shear stresses, and thus the Hirs axial gradient components, represent the original shear stress components of Eqns. 3.2 and 3.3 and are also readily quantified using the extracted local bulk velocities and Eqns. 3.4 - 3.6. The only remaining unknown is thus the form terms, which can now be quantified through the difference between the total gradient and the known component gradient terms.

A visual representation of the procedure used to isolate the FSS component terms is shown in Fig. 3.3 for a sample case from the deep $AR = 1$ data set. The top plot shows the effective film thickness, resembling the expansion and contraction behavior described thoroughly in Ref. [13]. The middle and bottom plots depict the isolated component terms of Eqns. 3.7 and 3.8, respectively, where each plotted line corresponds to an individual axial gradient term of the equations. Note that Eqn. 3.8 does not contain an inertia term, so this component is not included in the bottom plot of Fig. 3.3. In both cases, a cumulative, or axially integrated, quantity is plotted for each component according to Eqn. 3.9 as

$$dp = \int_0^z \frac{\partial p}{\partial z} dz \Big/ \Delta p \qquad du = \int_0^z \frac{\partial u}{\partial z} dz \Big/ \left(\frac{1}{2}\omega R\right) \tag{3.9}$$

in order to examine the net effect of each term on pressure (middle plot, Eqn. 3.7) or circumferential velocity (bottom plot, Eqn. 3.8). The axial plot is nondimensionalized by the model prescribed pressure differential such that the total pressure drop is from 1 to 0. The net effect of each term at the end of the single groove

section thus represents the fraction of the total pressure drop accounted for by that term. The circumferential plot is nondimensionalized by $\frac{1}{2}\omega R$, the fully developed bulk circumferential velocity value for a Couette-type cross film profile that is asymptotically approached in smooth and grooved seal flows. In this way, the net effect of each term is shown as a fraction of the fully developed bulk circumferential velocity.

We first consider the axial direction in the middle plot of Fig. 3.3. The total term clearly exhibits two linearly decreasing segments in each land section, similar to the pressure profile that would be seen in a smooth seal. The groove region experiences local pressure variation that correlates closely to the behavior of the film thickness. The inertia term mirrors the shape of the film thickness, where film expansion and contraction corresponds to local increases and decreases in pressure, respectively, in a Bernoulli-like manner. In the land sections, the Hirs component slope matches the total slope, confirming that a Hirs shear stress definition is an accurate model for the shear stress induced pressure loss in smooth sections. Within the groove, the slope of the Hirs term is altered slightly but a predominantly linear drop remains, highlighting a low sensitivity of Hirs shear stress definition to the local bulk velocity variations within the groove. The form component is seen to be approximately negligible in the land sections, as expected since the Hirs component captures the total contribution well. At the start of the groove, an initial form pressure drop is seen that aligns with the initial film expansion. A linear drop is observed throughout the middle part of the groove, though the slope is slightly smaller than that of the Hirs component. Finally, a sharp drop and recovery period is observed at the groove exit where the acknowledged effects of the sharp geometry and corresponding film contraction are typically accounted for through a groove loss coefficient. The net effect of the form component is to contribute just below 50% of the total pressure drop across the single groove model for this sample case.

For the circumferential direction in the bottom plot of Fig. 3.3, the total term again displays approximately linearly segments in each land section, now increasing. Across the groove, local increases and decreases in the circumferential velocity are observed, again occurring near regions of film expansion and contraction. The Hirs component shows an approximately linear increase across both the land and groove sections, a product of the bulk circumferential velocity being slightly less than the fully developed value of $\frac{1}{2}\omega R$ due to the presence of the grooves. Similar to the axial direction, the form component contribution in the circumferential direction is approximately constant in the land sections, as the Hirs component accounts for all of the total profile. Within the groove, similar behavior to the axial direction is again observed, with the net effect being a reduction in u across the groove equal to approximately 4% of the fully developed value of $\frac{1}{2}\omega R$ for this sample case. Note that for both the axial and circumferential direction plots, the total profile is a sum of the

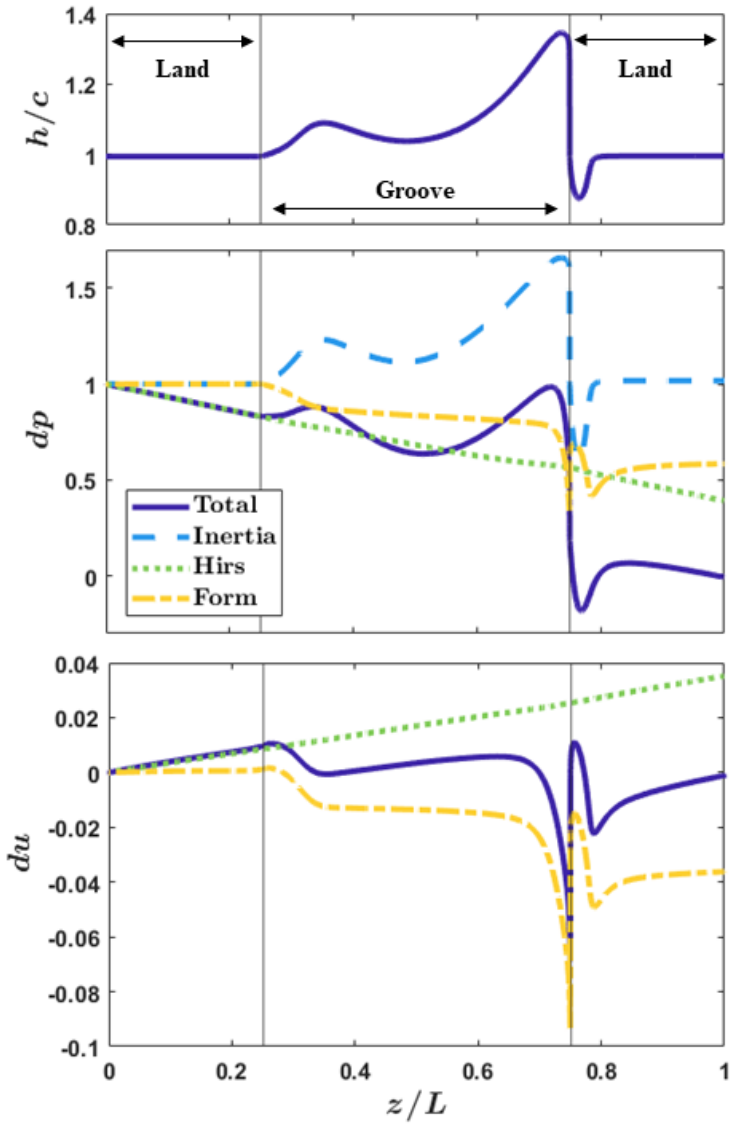

Figure 3.3: Sample processing and isolation of the effective film thickness (top) and individual components of the axial (middle) and circumferential (bottom) bulk flow momentum equations. The middle and bottom plots y-axis labels are defined in Eqn. 3.9.

other component profiles, confirming the isolation of the individual components.

Additional assessment of grid independence was conducted at this stage based on the sharp gradients and peaks observed in the form component profiles, particularly near the groove to land transition region. The form component isolation procedure, depicted in Fig. 3.3, was applied to simulation results from a sequence of refined grids, and the resulting profiles were analyzed. The same cases and grids used for grid independence in Ref. [13] were used again here, namely three grids with increasing number of elements and

four operating cases that bounded the original simulation set in Ref. [13]. Across the successively refined grids, only marginal qualitative differences were observed for the resulting axial and circumferential form component profiles. The minimum value along the form component profile differed by at most 2% and 6% in the axial and circumferential directions, respectively. The cumulative contribution of the form components, seen as the furthest axial point (rightmost point) along the profiles, differed by at most 3% and 4% for the axial and circumferential directions, respectively. Thus, the use of the present grid remained justified based on minimal variation in metrics specific to the FSS components targeted in this study.

With the FSS component quantified as described above and depicted in Fig. 3.3, its behavior and net effect can be examined across the geometry and Reynolds number range established through the single groove simulation data sets described in Table 3.3. The focus in this paper is on the FSS components. A complete discussion of the relationship between the effective film thickness and steady state performance can be found in Ref. [13]. Figure 3.4 displays the film thickness and cumulative axial and circumferential FSS component profiles for three cases with the same operating conditions and varying AR. Of note is the clear link between the behavior of the FSS components and the expansion and contraction of the film thickness. For example, the prolonged and larger magnitude film expansion in the $AR = 0.07$ case corresponds to larger magnitude decreases in p and u caused by the FSS component over a longer axial distance. The net effect of the FSS component in the axial direction is greatest for the $AR = 0.07$ case, also corresponding to the lowest leakage result among these three cases. In the circumferential direction, the net effect of all three cases is very similar, though across the groove, u decreases significantly more in the $AR = 0.07$ case than the other two presented here.

Figure 3.5 displays the cumulative axial FSS component profile for two case sets varying either the rotor speed or pressure differential, all with $AR = 1$. The film thicknesses and circumferential form stress profiles are approximately the same for these simulation subsets and are thus omitted. While the qualitative shape of the profile is consistent across the cases shown, the net effect of the axial FSS component increases with pressure differential and decreases with rotor speed. Larger Δp increases the axial velocity and creates sharper film transitions that increase pressure loss, while larger ω increases the land shear stresses and reduces the pressure drop induced by the form component within the groove.

While the full complexity of the FSS profiles provides valuable insight into the qualitative relationship between the physical flow patterns and the influence of the shear stresses, a linear approximation is employed to simplify the modeling and analysis presented in this paper and to allow for easy implementation into current

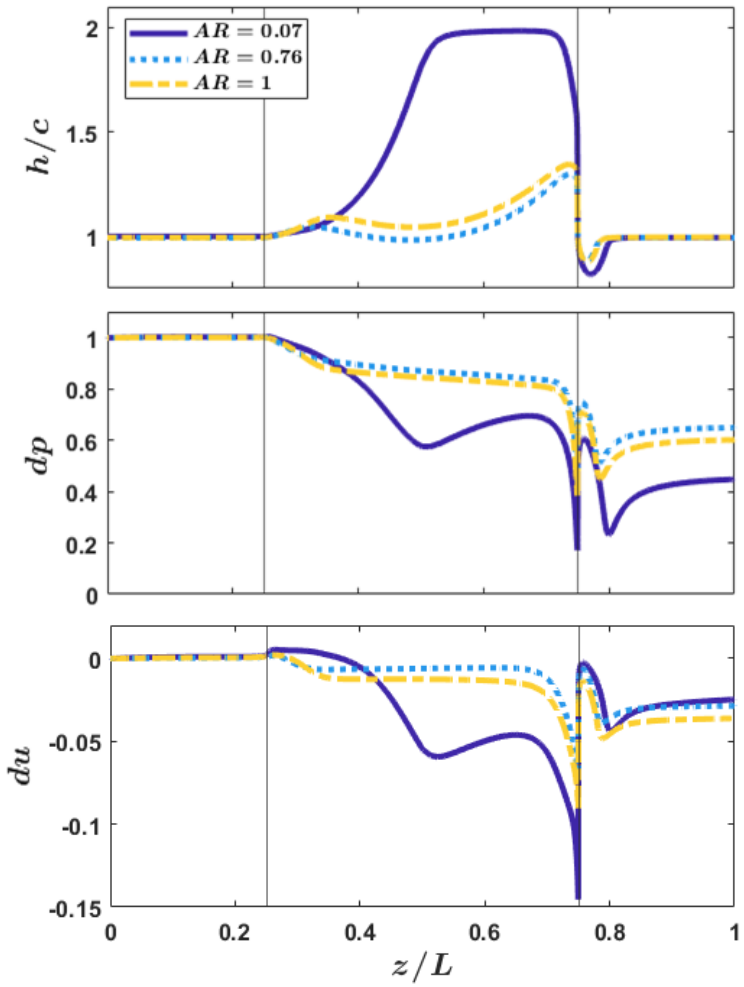

Figure 3.4: Profiles of film thickness, cumulative axial FSS component, and cumulative circumferential FSS component (top to bottom) for various AR. Note that all profiles in the bottom two plots correspond to the FSS component. The middle and bottom plots y-axis labels are defined in Eqn. 3.9.

bulk flow methods. A depiction of this process is shown in the top plot of Fig. 3.6. Initial consideration was for a simple linear fit to the discrete points along the FSS profile falling within the groove region, denoted by the black vertical lines in Figs. 3.3 - 3.6. This fit was intended to approximate the net contribution of the FSS component, which could also be captured by directly applying a linear approximation that matched this net contribution exactly at the end of the groove region. Both approximations are shown in the top of Fig. 3.6. The bottom of Fig. 3.6 displays the error in slope between these approximations for the axial FSS profile of a sample set of cases with $AR = 0.07$ representative of the entire data set, considering the directly applied net form contribution approximation to be the nominal value. The error is seen to increase sharply for cases with a large circumferential flow component, where $Re_x/Re_z > 2.5$. This approximately coincides with the upper

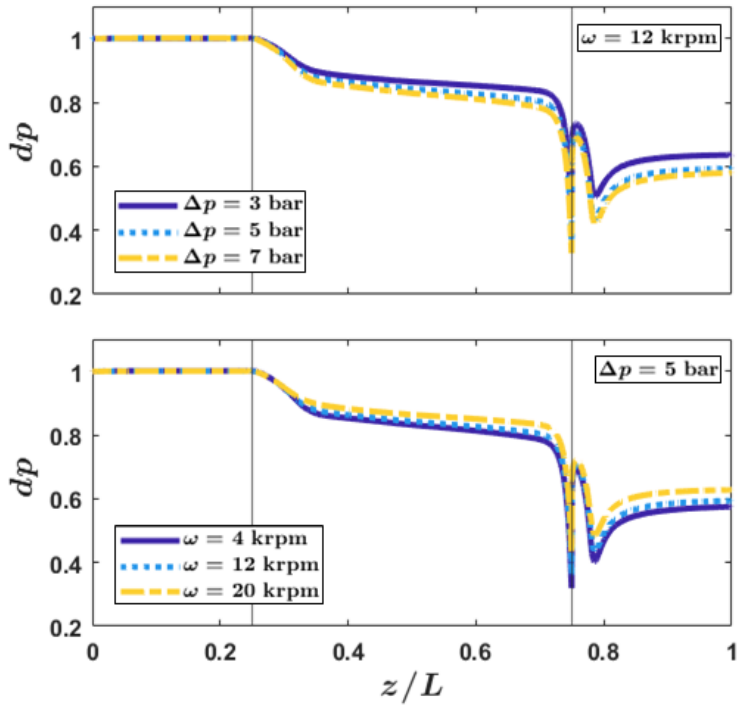

Figure 3.5: Profiles of the cumulative axial FSS component for various Δp and constant ω (top) and for various ω and constant Δp (bottom). The y-axis label is defined in Eqn. 3.9.

bound on Re_x/Re_z resulting from the core base data set, where Δp and ω prescribed in the simulations were bounded by the same limits as the experimental work. Cases with higher Re_x/Re_z, plotted to the right of the vertical red line, were subsequently considered to assess the applicability of the linear approximation. Low error values suggest that directly applying the net FSS contribution as a linear profile across the groove is a reasonable approximation to the true FSS behavior extracted from the single groove CFD results. The approximation thus becomes less appropriate for $Re_x/Re_z > 2.5$ where the error is higher. A review of the literature reveals that the conditions found in many seal applications naturally results in $Re_x/Re_z < 2.5$, as in a balance piston for a multistage pump where the total pump pressure rise creates a significant pressure driven axial flow component (e.g. Ref. [12]). Thus, the linear approximation that directly applies the net FSS contribution is considered widely applicable to industrially relevant applications and is adopted for the remainder of this paper.

Figures 3.3 - 3.6 depict the cumulative effect of the axial and circumferential FSS components in terms of the axial gradients. To allow for efficient implementation into current bulk flow methods, the models and results presented below consider the FSS in the equivalent τ representation using the appropriate factors

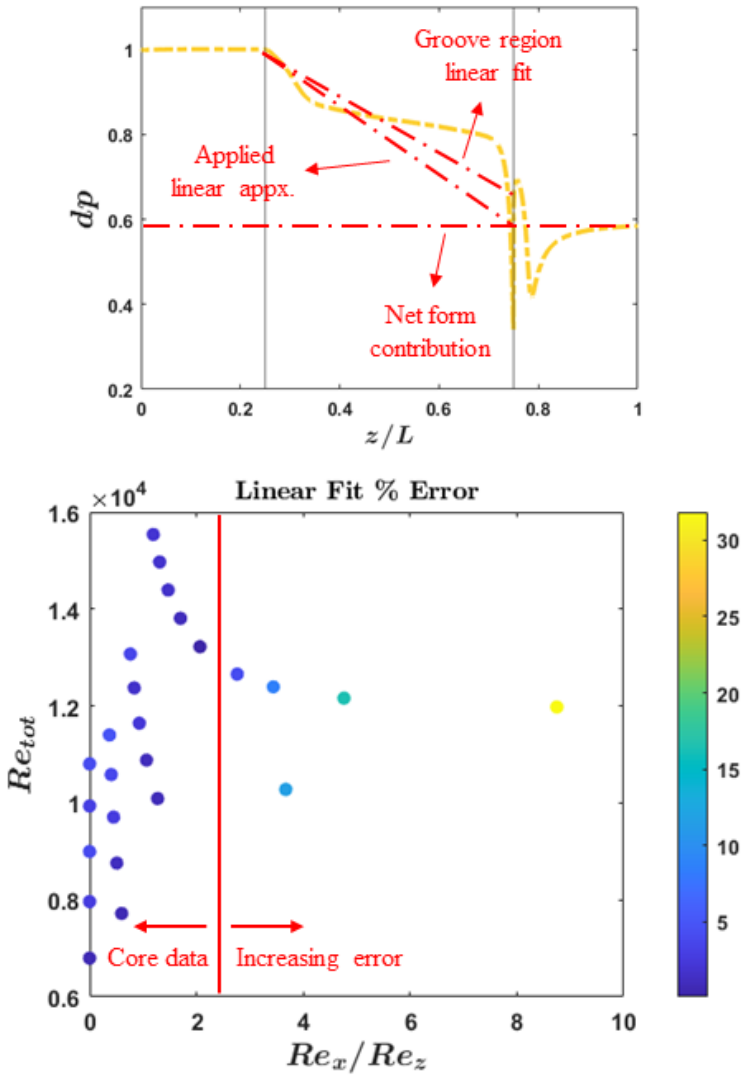

Figure 3.6: Top: sample axial FSS profile depicting the two linear approximations described in the text for the error calculation. The y-axis label is defined in Eqn. 3.9. Bottom: error in slope between the linear fit and the approximation that directly applies the net form contribution across the groove region.

according to Eqns. 3.7 and 3.8. In order to leverage the single groove simulation results towards the generation of models that can be implemented across different seal cases and conditions, a proper nondimensionalization of the FSS components was also identified. The FSS components are seen to cause a net reduction in both pressure and circumferential velocity. Since the value of the shear stresses in the land sections are well predicted by Hirs theory and the formulation is already included in many bulk flow models, the value of τ_{land} predicted by Eqns. 3.4 - 3.6 at the groove entrance is chosen as the nondimensional factor for the model results presented below. In the axial direction, both $\tau_{rz,land}$ and $\tau_{sz,land}$ serve to reduce p, so their sum,

$\tau_{z,land} = \tau_{rz,land} + \tau_{sz,land}$ is chosen for nondimensionalization. In the circumferential direction, $\tau_{r\theta,land}$ acts to promote u while $\tau_{s\theta,land}$ reduces it, so $\tau_{s\theta,land}$ is chosen for nondimensionalization. Thus, the ratios $\tau_{z,form}/\tau_{z,land}$ and $\tau_{\theta,form}/\tau_{s\theta,land}$ are used to generate the FSS models below, representing the ratio of the FSS component in the groove to the shear stress in the land sections. Surface models for these FSS ratios are developed in the next section, along with an assessment of their prediction capabilities.

3.3 Results and Analysis

The following sections detail how the form shear stress ratios, quantified above, were modeled for direct use in bulk flow methods. The variation of the form shear stress ratio with AR and with Re_x/Re_z and Re_{tot} are explored first, with the latter being used to generate surface models for the behavior. Additional single groove simulation data for different seals is used to validate the surface model predictions. Comparisons to CFD data from accompanying full seal simulations is used to assess the model's ability to capture developing flow conditions. Finally, the surface models are implemented into a simplified bulk flow method and the resulting predictions for leakage and groove circumferential velocity are evaluated based on their ability to capture the known and observed influence of the shear stresses.

3.3.1 Variation with Aspect Ratio

Initial efforts sought to utilize all three primary parameters of interest, namely AR, Re_x/Re_z, and Re_{tot}, to develop a model in three independent variables. While such a model is obtainable, the complexity of the relationship between the FSS ratios and AR, in particular, created a significantly weaker fit and added unnecessary complication to the physical interpretation of the observed trends in the data. To simplify the modeling and avoid a purely numerical fit, the authors separate the AR results and present them independently of the analysis in Re_x/Re_z and Re_{tot} discussed below. The AR results presented here will aid in the physical understanding of the FSS behavior with changes to groove geometry. The results in Re_x/Re_z and Re_{tot} will be used to generate models that capture changes in the FSS due to changes in operating conditions which is of primary importance to the predictive capability of bulk flow methods.

Figure 3.7 displays the FSS ratios as functions of AR for the discrete sample of cases in the three simulation sets with constant operating conditions and varying groove geometry (see the last three rows of Table 3.3). All three sets display similar qualitative features across the AR range shown, indicating that the

trends in the FSS ratios seen here are representative of the underlying flow physics. In the axial direction, a peak in FSS ratio is seen for relatively shallower grooves, corresponding to the region of minimum leakage across this same AR range. A local reduction in FSS ratio near $AR = 0.7$ is observed, where groove geometry allows a full recirculation region to form leaving less room for film expansion and causing a slight depression in the mid-groove film thickness. Note that the axial FSS ratio is analogous to the groove pressure drop ratio examined in Ref. [13] since the seal geometry was the same in both instances. An overall higher magnitude is seen for AR set 1 since the fluid properties and operating conditions for that set resulted in relatively high Re_{tot} and low Re_x/Re_z, increasing the sharpness of the film transitions while retaining a relatively low circumferential flow component.

In the circumferential direction, the highest values for the FSS ratio are at higher AR, indicating that deeper grooves are able to slow or reduce the circumferential velocity better than their shallow counterparts due to the increased surface area within the groove and an increase in the amount of fluid that opposes the circumferential flow in the clearance region. A similar but smaller magnitude local peak is observed in the same low AR region as for the axial direction. The FSS ratio is overall lower in magnitude for AR set 3, which had the highest Re_x/Re_z values amongst the three AR sets due to its low Δp and high ω. This suggests that the groove becomes less effective at reducing circumferential velocity relative to the land sections when the circumferential component of the seal flow increases, likely a result of the flow direction becoming more parallel to the configuration of the grooves which circumferentially spreads and lessens their effect on u.

The analysis of the FSS ratios versus AR provides invaluable insight into the behavior of the additional groove shear stresses as the groove geometry, and thus the flow pattern, varies. The influence of the Reynolds number quantities, Re_x/Re_z and Re_{tot}, is examined next and used to develop predictive models for the FSS for varying flow conditions.

3.3.2 Reynolds Number Models

Analysis of the FSS ratios as functions of Re_x/Re_z and Re_{tot} is the subject of this section. Surface models are generated and examined across the different simulation data sets. The prediction capability of these models is then assessed later, including the implementation of the models into a simplified bulk flow method to demonstrate the utility of the modeling methods in this paper.

Preliminary analysis indicated that the FSS ratios were strong functions of Re_x/Re_z and Re_{tot}, describing the direction and relative magnitude of the bulk flow vector in the axial-circumferential plane, for each data

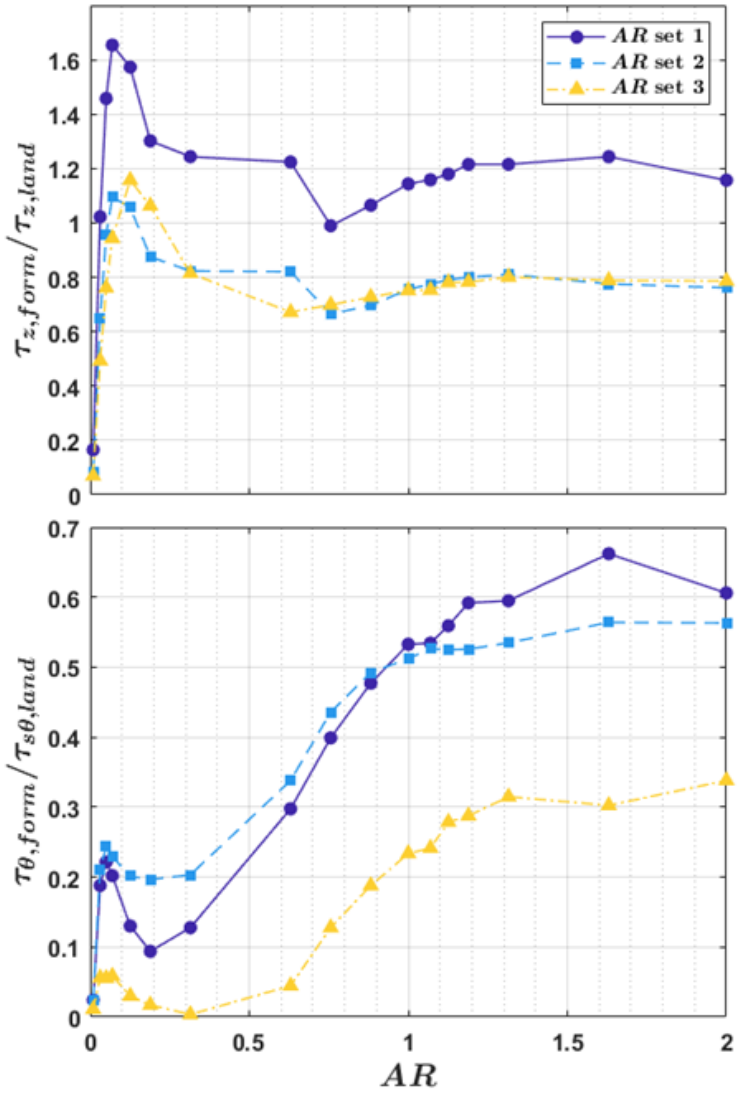

Figure 3.7: Axial and circumferential FSS ratios for a range of AR for all three AR sets. Results are approximately constant for $AR > 2$ and are thus omitted.

set with constant geometry and variable operating conditions (top three rows of Table 3.3). Figure 3.8 displays the axial (top row) and circumferential (bottom row) FSS ratio simulation data. Similar trends exist for both FSS ratios in the shallow, middle, and deep data sets, indicating consistent behavior that can be well approximated by a surface model with persistent formatting. Two additional data points for separate seal cases are included on the $AR = 0.76$ plots which serve as single groove validation cases, to be discussed below.

To produce a model for the FSS component that could be easily implemented into bulk flow methods, each

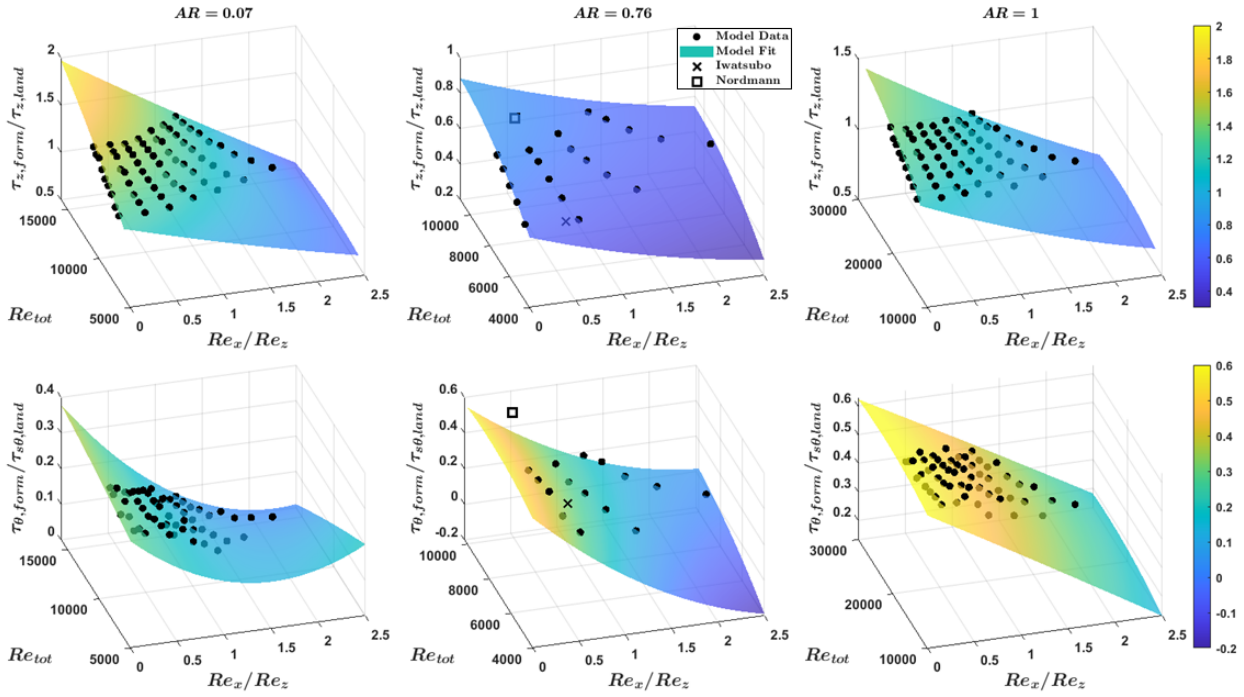

Figure 3.8: Data and surface model fits for the axial (top row) and circumferential (bottom row) FSS ratios for the shallow, middle, and deep data sets. Also included are the single groove validation case results (middle plots). The color (shading) scale for the surface model fits is uniform across each row of plots.

set of data in Fig. 3.8 was curve fit using linear regression analysis in two independent variables, Re_x/Re_z and Re_{tot}. Polynomial equations were considered based on initial examination of the data. A second degree polynomial was chosen to represent both the axial and circumferential FSS ratios, given by Eqns. 3.10 and 3.11 as

$$\frac{\tau_{z,form}}{\tau_{z,land}} = A_1 + A_2\left(\frac{Re_x}{Re_z}\right) + A_3 Re_{tot} + A_4\left(\frac{Re_x}{Re_z}\right)^2 + A_5\left(\frac{Re_x}{Re_z}\right)Re_{tot} + A_6 Re_{tot}^2 \tag{3.10}$$

$$\frac{\tau_{\theta,form}}{\tau_{s\theta,land}} = C_1 + C_2\left(\frac{Re_x}{Re_z}\right) + C_3 Re_{tot} + C_4\left(\frac{Re_x}{Re_z}\right)^2 + C_5\left(\frac{Re_x}{Re_z}\right)Re_{tot} + C_6 Re_{tot}^2 \tag{3.11}$$

based on an overall best fit across all simulation sets considered here and to provide consistency in reported model coefficients. In the circumferential direction, the data points with $Re_x/Re_z = 0$, or where $\omega = 0$, are omitted when determining the model coefficients to avoid the numerical divergence when dividing by $\tau_{s\theta,land} = 0$. Note that the FSS methodology, modeling, and bulk flow implementation presented in this paper would apply regardless of the specific model format chosen, allowing for the development of alternative numerical models for the FSS ratios that include additional variables or effects if desired.

The resulting surface models are displayed along with the model data in each plot of Fig. 3.8. The coefficients A_i and C_i are summarized in Table 3.4, including the model R^2 and adjusted R^2 values. The R^2 values are very high for all six models presented, indicating that the chosen second order polynomial model describes the variation in model data about the mean extremely well, and more generally, that the FSS ratio is a strong choice for capturing the additional groove shear stresses and its variation with seal flow conditions. Since the addition of coefficients to the model necessarily increases R^2, an adjusted R^2 may be employed to account for overestimation of the R^2 values by comparing the number of model coefficients to the number of data points. The adjusted R^2 is also well above an acceptable value across all models. Coefficients in Table 3.4 in gray cells and italicized are considered statistically insignificant in the present models based on a 90% confidence evaluation to determine if the coefficient is significantly different from zero. Removal of a model coefficient alters the significance of all other coefficients, so the statistical significance presented in Table 3.4 should be considered with respect to the current models and not representative of the global behavior of a particular parameter.

In the axial direction, the FSS ratio data and model show an increase with Re_{tot} and decrease with Re_x/Re_z, in agreement with the physical description of the behavior of the axial FSS in Fig. 3.5 for changes in Δp and ω. Based on the uniform color (shading) scale for the surface plots across all three data sets, it is observed that the FSS ratio is generally largest for the $AR = 0.07$ set, in agreement with previous results that a groove depth in that range results in higher FSS and less leakage than its deeper counterparts. The $AR = 0.76$ set is seen to be the least sensitive to both Reynolds number quantities, a possible product of the slight depression in the mid-groove film thickness mentioned above for this AR range that mitigates the interaction between the clearance and groove flows and thus the overall influence of the FSS. The slightly lower range of Re_{tot} that resulted from this particular data set is also a likely contributing factor to lower sensitivity overall.

The circumferential plots along the bottom row of Fig. 3.8 display slightly more scattered data, possibly due to increased sensitivity to radial averaging during bulk flow processing for the Couette-like circumferential velocity profile, though the high R^2 values still indicate a strong model fit to the data variation. Again, the FSS ratio is seen to qualitatively decrease with Re_x/Re_z, confirming that the groove is less effective at reducing circumferential velocity for cases with higher circumferential flow components. All three data sets seemingly show less sensitivity to Re_{tot} than in the axial direction, indicating that the flow direction in the axial-circumferential plane, and thus its relationship to the groove configuration as discussed above, is the

Table 3.4: Coefficients for the surface models presented in Eqns. 3.10 and 3.11 for each data set. Italicized gray cells indicate a statistically insignificant coefficient in the current fit based on 90% confidence criteria.

	$AR = 0.07$	$AR = 0.76$	$AR = 1$
A_1	0.59	0.21	0.64
A_2	*-0.089*	-0.17	-0.18
A_3	0.00012	0.00011	5.1e-5
A_4	*0.014*	0.024	0.026
A_5	-3.2e-5	*-1.8e-6*	-7.8e-6
A_6	*-2.0e-9*	-4.9e-9	-7.1e-10
R^2	0.98	0.98	0.98
$R^2_{adj.}$	0.98	0.98	0.97
C_1	0.25	0.36	0.52
C_2	-0.17	-0.52	-0.19
C_3	*1.1e-5*	*5.6e-5*	*9.0e-6*
C_4	0.072	0.071	*-0.0017*
C_5	*-9.8e-6*	*1.3e-5*	*4.3e-7*
C_6	*-1.7e-10*	*-3.5e-9*	*-1.9e-10*
R^2	0.95	0.99	0.97
$R^2_{adj.}$	0.94	0.99	0.96

primary factor dictating the influence of the groove on the circumferential velocity. As AR increases, the dependence on higher order terms appears to decrease, as seen in the lessened curvature of the model surfaces. This is supported by the decreased levels of statistical significance in the higher order term coefficients for the deeper groove cases.

The FSS surface models presented in Fig. 3.8 were based on simulation data for a square groove geometry at different AR and operating conditions. Additional simulation data was generated for a half-circle groove geometry based on the seal simulations of Untaroiu et al. [43]. The surface model fits, not included here for brevity, displayed similar traits to those for the square groove geometries, namely high R^2 values above 0.91 and qualitatively similar trends with Re_x/Re_z and Re_{tot}. This confirms the applicability of the FSS modeling approach presented here to more complex seal geometries and flow fields.

While the FSS ratio models presented here require their own coefficients, the physical modeling approach used in their development, namely the use of the effective film thickness, enables the models to capture the physical behavior of the additional shear stresses across the entire groove region without the use of a loss coefficient. This is shown to be true for a wide and industry applicable range of seal geometries and operating conditions. The formulation of the surface models also allows for easy implementation into bulk

flow methods since the recovery of the FSS magnitude depends only on the land shear stress, considered a well approximated and easily predicted quantity in current bulk flow methods. This is demonstrated in a later section, where the models are used in a simplified bulk flow method for leakage predictions and seen to improve the prediction of the influence of the additional groove shear stresses. An assessment of the predictive capability of the models for other seals and conditions is presented next.

3.3.3 Single Groove Validation

In order to further validate the prediction capability of the FSS ratio models presented above, two additional seal cases were considered using the same single groove modeling and analysis framework as was applied to the base case seal that generated the original model data. The seals chosen were based on the experimental work by Iwatsubo et al. [41] and Nordmann et al. [20] based on their use in the literature and relevance to industrial pump applications. The details of these seals are presented in Table 3.1. For each seal, a single groove model was generated and simulated representative of the $\Delta p = 5.88$ bar, $\omega = 3.5$ krpm, and $\Delta p = 7.3$ bar, $\omega = 6$ krpm cases for the Iwatsubo and Nordmann seals, respectively. The axial and circumferential FSS ratios were quantified and compared to the predicted values from the $AR = 0.76$ data set models, shown in the middle plots of Fig. 3.8, as this AR most closely matches the groove geometry of the Iwatsubo and Nordmann seals. The single groove CFD FSS ratios for the Iwatsubo and Nordmann cases are displayed alongside the data and model surfaces in Fig. 3.8.

Table 3.5 summarizes the prediction accuracy of the FSS ratio models for the two single groove validation cases. Included in the model predictions are 95% prediction confidence intervals, which include variation in the model data used to estimate the surface response and random variation for a new observation. For both validation cases, the prediction in the axial direction is very accurate, with each case having less than 5% error compared to the CFD calculated results. The circumferential predictions show a slightly larger discrepancy compared to the CFD results, with both FSS ratios being underpredicted by up to a 27%. This larger error is attributed to the previously described processing sensitivity in the circumferential direction, and future work could seek to directly quantify the influence of this error on bulk flow predictions. Still, the accuracy of the predictions given by the FSS ratio models is thus considered acceptable given the complexity of the FSS contributions being predicted, particularly in the circumferential direction.

The single groove validation results presented here demonstrate general applicability of the FSS models for the prediction of additional shear stress losses in seals of similar geometries. While the current models

Table 3.5: Comparison of the model predicted FSS ratios to those extracted from the single groove CFD validation cases. Note that the predictions were made using the $AR = 0.76$ data set models. Confidence intervals are for new model predictions.

Case	Predicted ±95% CI	CFD	% Error
	$\tau_{z,form}/\tau_{z,land}$		
Iwatsubo	0.58 ± 0.03	0.56	4.4
Nordmann	0.78 ± 0.05	0.76	3.0
	$\tau_{\theta,form}/\tau_{s\theta,land}$		
Iwatsubo	0.35 ± 0.05	0.47	27
Nordmann	0.42 ± 0.08	0.56	25

are limited to variations in Reynolds number for a single AR, the approach is shown to be valid and can be extended to different Reynolds number ranges and seal groove geometries, such as the half-circle groove geometry considered alongside the base model development above.

3.3.4 Comparison to Full Seal CFD

In addition to the direct single groove FSS model validation presented above, the models were assessed in their ability to predict the additional FSS component for grooves at different axial locations along the full seal length. The single groove CFD model assumes the seal flow is fully developed, approximating a groove sufficiently downstream of the seal inlet plane where the bulk velocity profiles across a groove are no longer changing from groove to groove. In a real seal, the circumferential velocity develops axially, beginning at a preswirl value dictated by upstream conditions and increasing asymptotically towards $\frac{1}{2}\omega R$, the previously described assumed value for fully developed Couette-type flow. This axial development causes Reynolds number variations between grooves, leading to potentially different FSS effects from each groove. For incompressible flow, the bulk flow axial velocity, and thus the axial Reynolds number, remains constant in each land section. As the circumferential velocity develops, the circumferential Reynolds number increases, leading to axial increases in both Re_x/Re_z and Re_{tot} for subsequent grooves further downstream of the seal inlet.

In order to assess the ability of the FSS ratio models to predict this potential variation in response with groove axial location, accompanying full seal CFD models were generated for each of the three seals in Table 3.1. The full seal model is depicted in Fig. 3.9. The CFD setup mirrors that of the single groove models,

namely an axisymmetric steady state model, except for the inlet and outlet boundary conditions. In order to best match the experimental seal conditions, the model inlet was specified by a mass flow rate equivalent to the experimentally reported leakage and a preswirl equal to the reported value, if available, or alternatively, the value used for the theoretical calculations in the respective papers. The preswirl ratios, $u/\omega R$, were set at 0.25, 0.08, and 0.2 for the Marquette, Iwatsubo, and Nordmann seals respectively. At the model outlet, 0 gauge pressure is specified. Since the full seal CFD models do not include upstream or downstream regions, these boundary conditions eliminate the need to consider inlet and outlet pressure loss, where the seal-only pressure differential becomes implicit to the CFD solution based on the specified mass flow. The simulation for the Marquette seal corresponds to the $\Delta p = 6.45$ MPa, $\omega = 24.6$ krpm experimental case. The same case is simulated for the Iwatsubo and Nordmann seals as in the single groove simulations above.

Once the full seal CFD results were obtained, individual groove sections, equivalent in geometry to the single groove counterparts, were processed and analyzed in the same manner as the single groove model and validation case results above. The CFD extracted FSS ratios were again compared to those predicted by the models in Fig. 3.8 for each axial groove, and the results are shown in Fig. 3.10. The model predictions are generated using the data set model best matching the groove geometry of each seal, namely the $AR = 1$ model for the Marquette seal and the $AR = 0.76$ model for the Iwatsubo and Nordmann seals. The model predictions include 95% prediction confidence intervals found in the same manner as for the single groove validation cases, shown in Fig. 3.10 as vertical error bars.

After the first few grooves in each seal case, the CFD results generally display a small axial decrease in FSS ratio. Recall that as the circumferential velocity develops axially, Re_x increases, so both Re_x/Re_z and Re_{tot} increase axially as well with the increase in Re_x/Re_z tending to be of greater relative magnitude. This same axial decrease in FSS ratio is observed in the model predictions, also seen as a move down the surface models in Fig. 3.8 for predominantly increasing Re_x/Re_z. Overall, there is strong quantitative agreement between the predicted and CFD extracted FSS ratio values in both directions and for all three seals, apart from the first groove in each case. Slight differences are observed between the single groove CFD results and downstream grooves of the full seal CFD results for the Iwatsubo and Nordmann seals, particularly in the circumferential direction. In these two seals, u does not reach a fully developed state by the end of the seal, so the flow field in the last few downstream grooves still does not match that of the fully developed single groove CFD model. This effect has a larger influence on the circumferential FSS ratio values, highlighting the larger sensitivity of $\tau_{\theta,form}$ and $\tau_{s\theta,land}$ to flow changes, specifically the circumferential velocity.

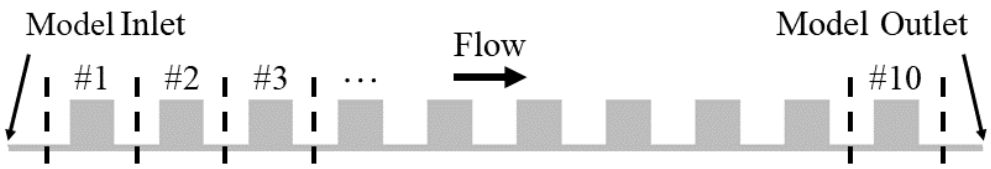

Figure 3.9: Diagram of the full seal CFD model, shown here for the Marquette seal where $N = 10$. Also shown are the groove sections individually processed for comparison to the FSS model predictions.

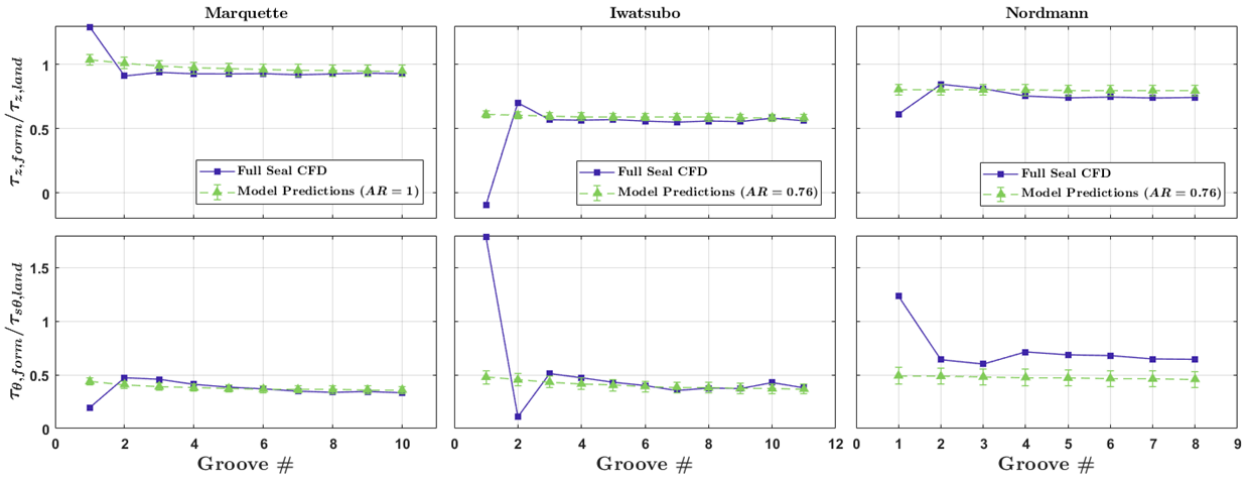

Figure 3.10: Comparison of the model predicted axial (top) and circumferential (bottom) FSS ratios to those extracted from individual groove sections of the full seal CFD simulations. Groove number increases with axial location. Included are 95% confidence intervals for new model predictions, displayed as vertical error bars.

The discrepancy between predicted and CFD extracted values at the first few grooves can be attributed to the developing flow at the beginning of the seal. The largest variation occurs in the seal with the smallest preswirl ratio value, the Iwatsubo seal, where the initial development of circumferential velocity just inside the seal is the most aggressive. This indicates a possible limitation of the current models where FSS ratio predictions for grooves with u significantly less than $\frac{1}{2}\omega R$ may not be as accurate as for grooves further downstream. More generally, this implies that the single groove CFD model that assumes fully developed flow may not provide the best approximation for grooves with developing flow conditions, even when the bulk flow Reynolds numbers are equivalent. Future work may seek to directly quantify the effect of this limitation on bulk flow method predictions and adapt the FSS models accordingly to account for developing flow conditions.

The single groove and full seal comparisons presented above confirm the prediction accuracy of the FSS

models generated in this paper. Finally, the FSS ratio models are implemented into a simplified bulk flow model to examine their influence on leakage and circumferential velocity predictions and demonstrate the efficacy of the present modeling approach.

3.3.5 Bulk Flow Leakage Predictions

Having established a method for extracting the FSS components, produced models for the axial and circumferential FSS ratios as functions of local Reynolds numbers, and assessed the performance of these models against additional single groove and full seal CFD simulation data, this section seeks to demonstrate the utility of the present FSS modeling approach when implemented in a bulk flow method through a series of simplified leakage predictions. A simplified bulk flow method is employed here based on Eqns. 3.1 - 3.3 which includes the same axial and circumferential momentum equations used in the single groove analysis procedure. Of note is the inclusion of $\partial h/\partial z$ terms, meaning that this method utilizes the effective film thickness, to be derived from the full seal CFD results. These bulk flow equations are employed for the clearance region flow along the entire axial length of the seal, including both land and groove regions. Many modern bulk flow methods for grooved seals modify the shear stresses between the clearance and recirculating flow based on additional assumptions, such as the free shear layer assumption and mixing length model employed by Marquette and Childs [24] in their three CV method. The present method makes no such change, as was assumed in the isolation of the FSS components, so that the FSS models can be directly applied. Proper modifications to the FSS analysis procedure presented above could render FSS models directly applicable to any particular bulk flow method. Many current bulk flow methods account for the additional losses due to the groove to land sharp contraction through an empirical groove loss coefficient, ξ_g, based on Eqn. 3.12 as

$$p_g - p_{land} = \frac{1}{2}\xi_g \rho w_{land}^2 \tag{3.12}$$

where w_{land} is the axial velocity in the subsequent land section after the contraction. The present method includes the pressure loss of Eqn.3.12 to analyze the sensitivity of the bulk flow predictions to ξ_g when the FSS model is not used.

The simplified method includes the unperturbed equation set only, producing leakage predictions with and without the FSS modification developed herein in order to clearly demonstrate the influence of the FSS model while avoiding the additional complexities associated with implementing an effective film thickness

based approached into existing perturbation methods. The discretized equations are solved using a simple explicit Euler method. An iterative method selects the inlet axial velocity that results in a pressure drop across the seal that best matches the target pressure differential. The circumferential velocity at the seal inlet is specified via the preswirl ratio and matches the values used to produce the full seal CFD results for each seal. The pressure drop across the seal that resulted from the full seal CFD simulations is prescribed as the target pressure differential in each case. As the effective film thickness served as the basis for the FSS modeling approach and is incorporated into the bulk flow equations used here, an effective film thickness is derived from the full seal CFD results and prescribed for each seal case.

Leakage predictions are generated for each of the three seals in Table 3.1 for the same operating case as in the full seal CFD simulations. Without the FSS model, leakage is predicted for a range of ξ_g to assess sensitivity to this empirical coefficient, with a range of 0 to 0.5 chosen based on reported values for ξ_g or for the similarly defined inlet loss coefficient. When the FSS model is employed, ξ_g is set to 0 as the FSS model inherently includes the additional losses at the contraction point. Local Reynolds numbers are calculated at the start of each groove which determine the value of the FSS ratio used within that particular groove region.

Figure 3.11 displays the leakage predictions for each seal, displaying the experimentally reported values, standard bulk flow predictions for various ξ_g, and modified bulk flow predictions when the axial FSS model is included. Note that the inclusion of the circumferential FSS model has minimal influence on overall leakage prediction and was not included in generating the results of Fig. 3.11. Its influence on the prediction of circumferential velocity is presented independently. First, note the reduction in leakage for increasing ξ_g in the standard method results. A larger ξ_g is meant to approximate higher losses at the sharp contraction, leading to less pressure drop being accounted for by the land sections and a reduction in predicted leakage as expected. A percent difference above 35% is observed between the lowest and highest values for ξ_g for each seal case. While the treatment of the shear stresses within the groove region may differ between bulk flow methods and alter the magnitude of variation in predicted leakage, these results are considered generally representative of the high sensitivity to groove loss coefficient for bulk flow methods.

A red vertical line is included to denote the intersection between the standard bulk flow predictions and experimentally reported leakage, where the x-axis value of this intersection represents the value of ξ_g needed to best match the experiments within the present simplified bulk flow method. As previously stated, the value for ξ_g is frequently assumed, often equal to 0.1, without proper justification. The current results suggest that the most experimentally accurate predictions come with varying values of ξ_g depending on the specific seal,

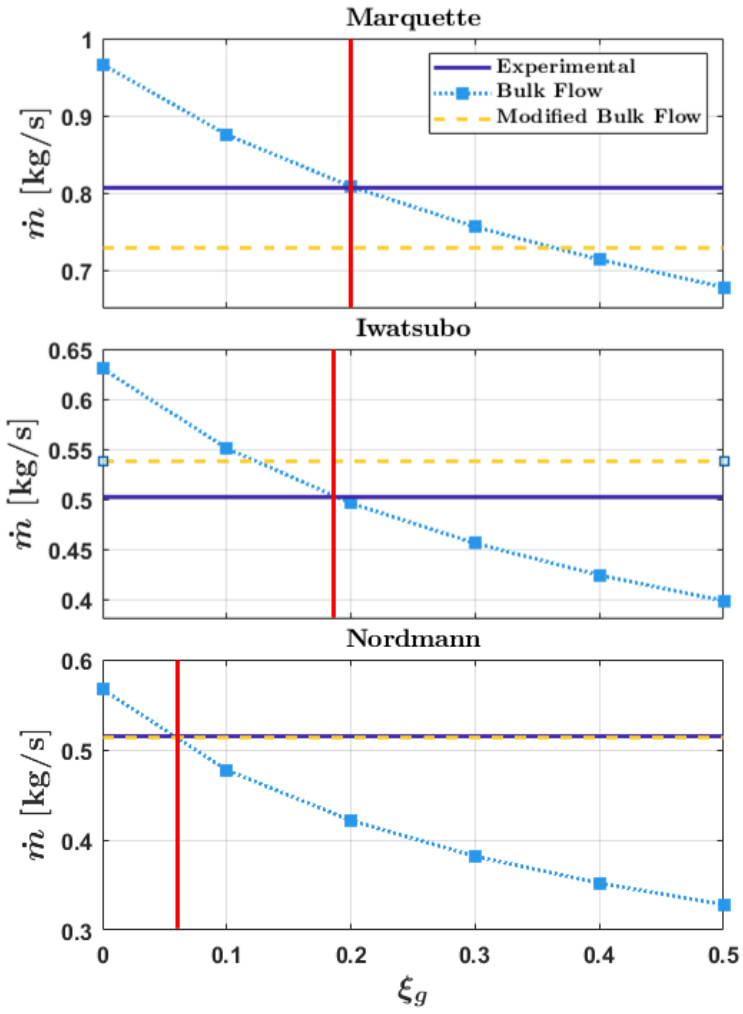

Figure 3.11: Prediction of leakage vs. ξ_g for the standard bulk flow method compared to the FSS modified bulk flow method and experimentally reported leakage. The vertical red (solid) line denotes the intersection between the standard bulk flow predictions and experimental results.

with optimal ξ_g values both above and below the typical 0.1 assumption shown here. The modified bulk flow results are generated when the axial FSS model is included and $\xi_g = 0$, producing a single leakage value. The sensitivity to ξ_g is eliminated since the FSS model accounts for additional shear stress losses across the entire groove, including the sharp contraction. Leakage values predicted by the modified method differ from the experimental results by at most 10%, demonstrating that a bulk flow method that utilizes the FSS model can predict leakage with reasonable accuracy while reducing the empiricism associated with the groove loss coefficient.

A similar comparison is made when including the FSS model in the circumferential direction. Circumferential shear stresses dictate the axial development of circumferential velocity, which is known to be of importance to the prediction of cross-coupled stiffness and thus the contribution of the seal to pump rotordynamic stability [3]. The axial profile of circumferential velocity is compared in Fig. 3.12 for each of the three seals to demonstrate the influence of the FSS model on the circumferential velocity within the groove region. In Fig. 3.12, the experimental results are replaced by the circumferential velocity profile extracted from the full seal CFD results, as bulk flow velocity profiles are rarely measured or reported in grooved seal experimental studies and were not available here. The standard bulk flow results were generated with $\xi_g = 0.1$, the typically assumed value, and without the axial FSS model. The modified bulk flow results include the FSS model in both the axial and circumferential direction. The observations remain the same in both cases with or without the axial FSS model.

All axial profiles of circumferential velocity across the three cases show u axially approaching $\frac{1}{2}\omega R$ or a value near it, as expected, though the rate of increase depends on the particular seal geometry, operating conditions, and preswirl ratio. In the standard bulk flow prediction, u approaches $\frac{1}{2}\omega R$ exactly, as the simplified bulk flow method used here includes no alteration to the circumferential momentum equation within the grooves. The full seal CFD profiles approach a value slightly less than $\frac{1}{2}\omega R$ due to the presence of the grooves, leading to a net reduction in u across the entire seal. A sample profile for a single downstream groove is shown in the overlay of the top plot of Fig. 3.12. The solid line full seal CFD result displays approximately linearly increasing segments in the land sections and a net reduction across the groove. The balance between the land and groove region effects prevents u from developing fully to $\frac{1}{2}\omega R$, as seen in the lower final value for u for the CFD results. When the FSS model is included, the physical behavior of the profile now closely resembles the CFD results. Again considering the top plot overlay, the rate of increase in u in the land sections is approximately equivalent between the CFD and modified bulk flow results. More importantly, a linear reduction in u is observed across the groove in the modified bulk flow profile, leading to a better approximation for the final value of u at the end of the seal. The approximation of u near the seal inlet is less accurate than near the outlet, in agreement with the observations made in the previous section. Aside from differences in the overall rate of development and groove influence on u, similar trends are observed across all three seal cases, indicating a strong ability of the FSS model to capture the physical behavior of u within the groove and across the entire seal.

The comparisons in Figs. 3.11 and 3.12 clearly demonstrate that when implemented into a bulk flow

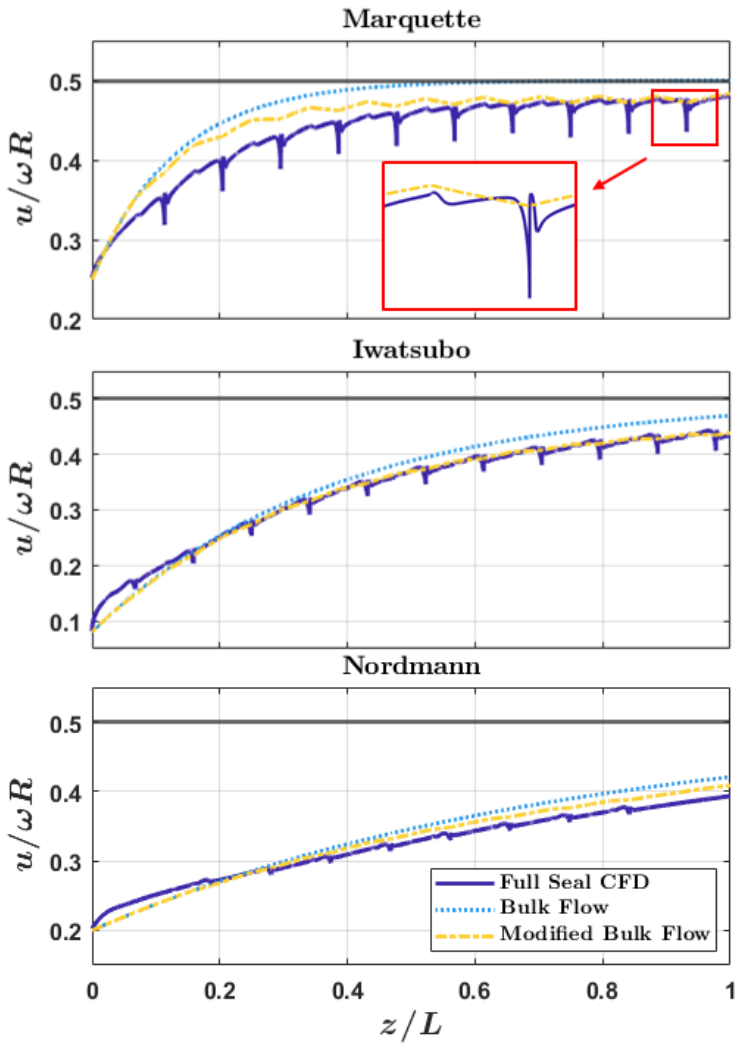

Figure 3.12: Prediction of the axial profile of circumferential velocity for the standard bulk flow method compared to the FSS modified bulk flow method and full seal CFD results.

method, the axial and circumferential FSS models can effectively capture the physical behavior and influence of the additional shear stresses within the groove region. While the results presented here were generated using a simplified representative bulk flow method, the FSS methodology in this paper is grounded by a physical analysis and understanding of the flow, making the approach adaptable to other bulk flow methods currently deployed or in development.

3.4 Conclusions

This paper presents the first method for quantifying the additional shear stress contributions by grooves in annular seals through the use of an effective film thickness based analysis. As an extension to the methodology in Ref. [13], this study utilizes single groove CFD simulation data to isolate, analyze, and quantify the axial and circumferential shear stress components within the groove region as a correction to a traditional shear stress definition. The term form shear stress (FSS) is adopted as a result of the observed link in behavior between the shape, or form, of the effective film thickness and the groove shear stresses. Surface model fits for the FSS are developed as functions of the circumferential to axial Reynolds number ratio and total resultant Reynolds number. High R^2 values above 0.91 and consistent behavior across the data sets confirms the use of the models to capture the variation in FSS behavior. Single groove simulations for additional seal cases were used to assess the prediction accuracy of the FSS models. The predicted FSS ratios had a maximum error of 4.4% and 27% in the axial and circumferential directions, respectively, an encouraging result given the complexity of the groove flow field and its influence on the shear stresses. Accompanying full seal CFD simulations were used to assess the model predictions for developing flow conditions, in contrast to the fully developed assumption of the single groove simulations used to generate the model data. The prediction accuracy is lower for grooves where the circumferential velocity is significantly less than the assumed fully developed value but improves for grooves further downstream of the seal inlet. This indicates that the current models are limited in their ability to predict the FSS contributions for grooves nearest to the seal inlet, though the net influence on bulk flow predictions is assumed to be minor since the effect is generally limited to a few grooves. A simplified bulk flow method that incorporates the effective film thickness is used to generate leakage and circumferential velocity profile predictions to demonstrate the utility of the FSS modeling approach. When implemented, the axial FSS model eliminates the sensitivity to a commonly used and empirical groove loss coefficient. Leakage predictions for all three seal cases considered fall within 10% of the experimentally reported values which compares well to the industry standard bulk flow prediction accuracy. In the circumferential direction, use of the FSS model reduces the predicted net circumferential velocity across the entire seal while also capturing a local decrease in circumferential velocity within the groove region, both in strong agreement with the full seal CFD results.

Use of the effective film thickness in shear stress analysis of grooved seals allows for more physical information to be inherently included in the modeling of a notoriously empirical and uncertain quantity in

bulk flow modeling. By directly quantifying the form shear stress components through the effective film thickness for the first time, this paper demonstrates a modeling approach that can accurately capture and predict the behavior of the shear stresses within a groove region without the need for an additional empirical loss coefficient, thus significantly reducing the uncertainty and empiricism within a bulk flow method. The novel approach presented here is shown to be generally applicable to seals of varying geometry and operating condition and can be easily adapted and implemented into existing bulk flow analysis methods, providing an avenue for substantial improvements in bulk flow prediction accuracy for grooved seals.

The present work addresses the formulation of the FSS models and their ability to capture grooved seal flow physics through a demonstration of the predictive capability and modeling feasibility in a simplified bulk flow method. Future research could explore the implementation of FSS models into full bulk flow methods including rotordynamic coefficient prediction. Minor modifications to the FSS analysis procedure would facilitate implementation into the array of existing bulk flow frameworks for a comparison of the impact on prediction results. Additional single groove cases could also be utilized to expand the parameter space or consider the influence of additional effects, such as compressibility, to move towards a more comprehensive FSS model.

Chapter 4

CFD Sensitivity Study

The corresponding manuscript title for this chapter is "Computational Fluid Dynamics Prediction of Rotordynamic Coefficients for Grooved Seals: Model and Numerical Sensitivity." The manuscript has been accepted for publication in the *ASME Journal of Engineering for Gas Turbines and Power* at the time of dissertation writing.

Nomenclature

$\dot{m}$	Leakage	θ	Circumferential coordinate
K, k	Direct, cross-coupled stiffness	$[X]$	Placeholder for arbitrary quantity
C, c	Direct, cross-coupled damping	$\Delta[X]$	Uncertainty in quantity $[X]$
M, m	Direct, cross-coupled mass	ω	Rotor speed
N	Number of elements	Ω	Whirl speed
r	Grid refinement ratio	e	Dynamic eccentricity (whirl amplitude)
α	Growth rate	c	Clearance
p	Pressure	ε	Whirl amplitude ratio, e/c
u, w	Circumferential, axial velocity	y^+	Y plus, nondimensional wall distance
x, z	Circumferential, axial direction		

Subscripts

ax	Axial	l	Land
rad	Radial	in	Seal inlet
cl	Clearance	0	Bulk (radially averaged)
gr	Groove		

4.1 Introduction

Many turbomachinery applications employ annular seals to reduce leakage flow across a region with a large pressure differential. A multistage centrifugal pump, for example, may include impeller neck ring seals, interstage seals, and balance drums to equilibrate the full pressure rise across the pump. Introducing circumferential grooves on the rotor or stator surface offers additional leakage reduction through kinetic energy dissipation between the land and groove sections but comes with increased flow complexity and analysis difficulties. As trends in turbomachinery continue to seek higher efficiencies and operational extremes, the need for accurate and robust rotordynamic prediction and stability analysis methods remains high.

Early analysis methods utilized bulk flow theory based on Hirs turbulent thin film theory [9], radial averaging, and a perturbation method that simplified the problem to a single dimension. While efficient, bulk flow methods rely heavily on empirical coefficients and thus contain accuracy limitations depending on the level of tuning. As computational power continually increases, full computational fluid dynamics (CFD) methods have become an attractive alternative as they require few assumptions on the nature of the flow and are generally applicable to all sealing scenarios. The most recent CFD advancements for seal analysis have focused on fully transient methods, where the whirl trajectory of the rotor is explicitly modeled and time-dependent solutions are obtained using moving grid solutions (e.g. [17, 18]). These methods are widely applicable and potentially very accurate, but their development is still an active research area, and the transient nature of the solutions comes at a high computational cost [19].

A more mature method, and the focus of this paper, is the quasi-steady (QS) method, which employs a rotating reference frame to transform the inherently transient whirling rotor problem into a series of steady-state solutions. Using appropriately modified boundary conditions on the rotor and stator surfaces, a set of simulations for various whirl speeds produces frequency independent rotordynamic coefficients at a reduced computational cost when compared to its transient counterparts. The QS method has been applied to many seals studies over the last few decades, including for incompressible grooved seals. For example, Mortazavi and Palazzolo [16] applied the QS method to a detailed groove-on-rotor seal model, demonstrating the method effectiveness and explaining the destabilizing nature of that particular seal. San Andrés et al. [12] studied a boiler feed pump using the QS method while extracting information from the CFD results to be used in a modified bulk flow method.

Despite successful and widespread use in the literature, inconsistencies exist amongst published CFD studies regarding the treatment of certain modeling aspects. This leads to wide variability in model setups. In addition, full quantitative analysis on the impact of these choices is often not presented, and few studies have been dedicated to this cause. Pugachev et al. [44] perform a wide sweeping sensitivity study on a short gas labyrinth seal model, examining differences in results produced by various CFD methods, turbulence models, and downstream region lengths, among other modeling features. Snyder and Santos [45] perform a similar sensitivity sweep for a set of liquid and gas smooth seal models, though no upstream or downstream regions are included in the model. The coverage in prior literature of particular modeling aspects, including upstream and downstream regions, centrifugal growth, and whirl amplitude, that provides quantitative explanations for certain modeling choices, specifically when using the QS method for incompressible grooved seals, is thus insufficient.

Based on the shortcomings in the currently available literature, this study has the following objectives: 1) to demonstrate the variability and gaps in understanding of how particular modeling choices influence rotordynamic coefficient prediction results, 2) to comprehensively study the sensitivity of the predicted leakage and rotordynamic coefficients when varying these modeling choices, specifically when using the QS method for a circumferentially grooved seal model, and 3) to provide rigorous quantitative results on the influence of these modeling choices where only qualitative discussions existed previously. This is the first paper dedicated to a comprehensive and quantitative analysis of the influence of the upstream and downstream regions, centrifugal growth, and whirl amplitude on predicted leakage and rotordynamic coefficients when using the QS method with an incompressible grooved seal model. The discussion will serve as a valuable resource for engineers seeking to apply CFD methods for grooved seal analysis, highlighting the careful considerations needed to ensure accuracy improvements over bulk flow analysis counterparts. Ultimately, this work will advance more regular use of CFD methods due to stronger understanding of the modeling details and mechanisms dictating their performance.

The remainder of this paper is structured as follows. First, a brief introduction and survey of the literature specific to the modeling aspects investigated in this study is presented. The computational modeling approach and geometric model chosen are detailed next, namely the use of the quasi-steady (QS) method for rotordynamic coefficient predictions of annular seals and the base case circumferentially grooved seal model. A numerical uncertainty estimation is then provided for the mass flow rate and each of the rotordynamic coefficients, followed by an investigation into local grid refinement sensitivity within the grooved regions.

Results are then presented quantifying and analyzing the impact of the upstream and downstream regions and boundary conditions, rotor centrifugal growth, and whirl amplitude. Finally, a summary of the sensitivity results and their impact are given, followed by concluding remarks.

4.2 Literature Survey

The following sections contain brief surveys of the literature pertaining to the specific modeling features investigated in this study. This survey addresses the paper's first objective by detailing the variability in modeling setup and justification that led to the modeling approach in the present study. Each subsection corresponds to subsections of the results presented later in this paper.

4.2.1 Upstream and Downstream Region

It is almost universally agreed upon that the computational model most closely matching the geometry and setup of the target experimental or in-use rig will produce the most accurate predictions. Despite continually increasing computational power, a full-scale, intricate CFD model for each design iteration is practically infeasible, and modelers will be forced to determine which modeling aspects are paramount as they balance accuracy and efficiency. The inlet and outlet boundaries and the inclusion of upstream and downstream regions in annular seal CFD models is often commented on in this regard with varying levels of justification. Few studies have attempted a comprehensive and quantitative investigation of their influence on the predicted rotordynamic coefficients. Since these regions are rarely included in bulk flow methods, and instead treated as empirical inlet and outlet loss and preswirl coefficients, their inclusion in full CFD models suggests a more physically accurate prediction.

Moore [46] performed a CFD investigation of a gas labyrinth seal in seal-only, with upstream, and with upstream and downstream configurations, noting that the addition of the upstream region improves the cross-coupled stiffness while adding the downstream region improves the direct stiffness, though the comparison to experimental results still shows significant error and analysis of the flow field differences producing those changes in coefficients was not provided. Wagner et al. [47] employed the QS method on a gas labyrinth seal model, stating that early on in their investigation it became obvious that the complete model geometry and boundary conditions had a significant impact on rotordynamic results. The authors detail the sensitivity of the seal flow field to the boundary conditions and flow field in the upstream region, as well as

the flow in the downstream region impacting the flow field in the seal while producing its own non-negligible forces. A comparison of the forces from the models with different geometric aspects incorporated suggest that the regions external to the seal itself can generate non-negligible forces. A parametric study by Pugachev et al. [44] considered the upstream region to be fixed based on the experimental setup geometry and examined the effect of increasing the length of the downstream region, though the forces produced in the downstream region (any configuration) are not included in the calculation of global coefficients. The authors note a significant decrease in magnitude of the direct stiffness when the length of the downstream region is doubled, but provide no physical explanation for this mechanism. Other papers dealt more specifically with the resulting flow fields that may influence the changes in coefficients. In a study employing the QS method for gas labyrinth seal predictions, Tsukuda et al. [48] included an upstream region that best approximates the experimental geometry (though exact dimensions were not provided with the experiments). The authors provide circumferential pressure profiles within the upstream region that display nonzero perturbed pressures and comment on the need for an accurate upstream region based on this fact, though no comparison of predictions for various upstream geometries is presented.

More recently, CFD studies of annular seals have sought to include all details of the experimental setup in the geometric model, including detailed versions of the upstream and downstream regions and the locations of the inlet and outlet boundaries. Mortazavi and Palazzolo [16] employ the QS method for rotordynamic coefficient prediction of a groove-on-rotor seal, using detailed radial injection ports to accurately model swirl and suppress back flow at the inlet and an outlet chamber, labyrinth tooth, and extension region to suppress back flow at the outlet. The resulting predictions compare well to experiments, and the authors comment on the importance of subdomain modeling in CFD predictions of seals. Thorat and Hardin [49] perform a similar study for a gas hole-pattern seal, including radial inlet nozzles, an outlet chamber, radial outlet ports, and a full exit labyrinth seal to closely match the experimental setup. The CFD method employed is verified as a reliable rotordynamic prediction tool based on good comparisons to the experimental values. While studies such as these produce good comparisons to experiments and suggest the need for geometrically accurate models, such analysis is not yet available for all sealing scenarios, and a quantitative comparison of predictions with geometrically varying subdomains is still lacking. In addition, the influence of inlet and outlet boundary condition and their relationship to the upstream and downstream regions has not been fully considered.

4.2.2 Rotor Centrifugal Growth

It is well known that seal clearance can play a pronounced role in system performance [3], though deviations from the nominal or static clearance can also have a significant impact on leakage and rotordynamic coefficient prediction. For example, Waschka et al. [50] studied the influence of rotation on seal discharge coefficient for a gas labyrinth seal, noting that clearance reductions of up to 50% of the original value were possible due to centrifugal and thermal effects. A recent series of studies by Subramanian et al. [51, 52] seek to create a combined CFD-FEA method to predict rotordynamic coefficients for gas labyrinth seals that includes rotor centrifugal and thermal growth effects, finding a 25% deviation in effective damping even at the lowest running speed when only centrifugal growth is considered.

Despite the evidence suggesting radial growth effects must be taken into account during modeling, many experimental investigations do not include specific measurements of the dynamic or running clearance, leaving modelers to guess or approximate based on the available data. In a comprehensive CFD study of a gas labyrinth seal, Moore [46] discusses inaccuracy in the experimentally reported clearance that resulted in wide discrepancies between their simulation results and the experimental ones. The clearance was subsequently reduced until the predicted pressure drop and leakage matched the reported values, assuming the adjusted clearance to be correct. Similarly, Mortazavi and Palazzolo [16] adjust the clearance of a groove-on-rotor liquid seal to account for thermal growth and also adjust the rotor surface roughness until the correct leakage value is predicted. The authors note that many combinations of clearance and surface roughness can produce the same leakage result, stressing the importance of meticulous dynamic readings for both parameters during experiments. Given these shortcomings, contributions to the literature are necessary regarding the influence of clearance deviations due to centrifugal growth on model predictions. Results specific to grooved annular seals and the QS method are desired to fully describe the changing flow mechanisms and to highlight the need to report running clearance values should a system be properly modeled.

4.2.3 Whirl Amplitude

The dynamic response of a sealing system is caused by the unsteady, whirling motion of the rotor resulting from operational load imbalances. Modeling methods for annular seals capture this effect through perturbation techniques, where eccentricity, or a deviation from the equilibrium operating position, is imposed. Many studies have experimentally investigated the effect of static eccentricity on seal performance (e.g. [29, 22]),

though fewer have studied the effect of varying whirl amplitude (dynamic eccentricity) on both performance and on modeling prediction results.

When applying CFD methods to annular seal problems, the choice of modeling whirl amplitude varies significantly. In an early investigation using the QS method, Athavale et al. [53] choose $\varepsilon = 0.5$ without justification in order to examine internal flow fields and demonstrate the capabilities of the new advanced CFD methodology, despite Childs [3] suggesting a linearity threshold of $\varepsilon = 0.5$ when considering eccentricity effects. Since the assumption of linearity relies on as assumed small perturbation parameter, a more common choice is $\varepsilon = 0.1$, as employed by Yang and San Andrés [38] when investigating the effect of a rounded corner at the upstream to seal contraction point. Still, this choice is rooted in case-by-case decision making based on previous modeling experience (e.g. early QS studies by Moore [46] frequently cited in the literature) and is not often considered fully in terms of its impact on modeling predictions. Untaroiu et al. [14] claim the whirl amplitude choice is arbitrary and that the predicted coefficients show little sensitivity to the particular value, though no quantitative information is presented to support this claim.

Recently, CFD studies seeking to quantify the effect of whirl amplitude on rotordynamic coefficient predictions for annular seals have started to emerge. In a wide parameter sweep and sensitivity investigation for a sample smooth seal, Snyder and Santos [45] comment on an optimal value of $\varepsilon = 0.2$ being used based on trade-offs between numerical error for too small ε and an invalid linear description of the forces for too large ε, though no quantitative results are presented. Li et al. [33] examine rotordynamic coefficient predictions at multiple whirl amplitudes across a range of static eccentricities noting that the effect of whirl amplitude is small and increases with static eccentricity, though the whirl amplitude range is limited to $\varepsilon < 0.1$. Zhang et al. [54] perform a similar analysis for a sample smooth seal, but also include ”nominal” coefficient predictions for a concentric case with varying whirl amplitude ratio up to 0.8, observing significant deviations from linearity especially at higher whirl amplitudes, though predictions were limited to a smooth seal case. Analytical work by Ikemoto et al. [55] and Yamada et al. [56] extended traditional bulk flow analysis for plain seals to include higher order perturbation terms that account for large whirl amplitude and static eccentricity, though the analysis is again limited to smooth seals. The influence of whirl amplitude on rotordynamic coefficient prediction when using the widely employed QS method has not been fully investigated, in particular for grooved seal cases.

The reviews presented above establish a clear need for additional investigation into the influence of the upstream and downstream regions, centrifugal growth, and whirl amplitude on rotordynamic coefficient

predictions when using the QS method for incompressible grooved seals. The computational method used in this study is presented next, followed by the results and analysis covering each of these modeling features.

4.3 Computational Methodology

The rotordynamic coefficient prediction method, the quasi-steady (QS) method, used in this study is covered first in this section. The details of the computational model are presented next, where a model of a representative grooved annular seal was created to serve as a base case upon which various modeling changes could be made and investigated. Once the base case was established based on acceptable prediction of the rotordynamic coefficients as compared to the experimental results, numerical uncertainties were quantified for rigorous treatment of the results. A local grid sensitivity study focusing on grid refinement within the groove regions is also presented.

Dynamic analysis of grooved annular seals involves predicting the rotordynamic response of the fluid system to the unsteady, whirling motion of the rotor. In order to perform linear stability analysis of a turbomachine that includes the contributions of the sealing component, a well established linearized model for the seal response to a small perturbation of the rotor from a centered operating position is employed, taking the form

$$-\begin{bmatrix} F_x \\ F_y \end{bmatrix} = \begin{bmatrix} K_{xx} & K_{xy} \\ K_{yx} & K_{yy} \end{bmatrix} \begin{bmatrix} x \\ y \end{bmatrix} + \begin{bmatrix} C_{xx} & C_{xy} \\ C_{yx} & C_{yy} \end{bmatrix} \begin{bmatrix} \dot{x} \\ \dot{y} \end{bmatrix} + \begin{bmatrix} M_{xx} & M_{xy} \\ M_{yx} & M_{yy} \end{bmatrix} \begin{bmatrix} \ddot{x} \\ \ddot{y} \end{bmatrix} \tag{4.1}$$

where x and y are the displacement of the rotor relative to the stator [3]. The rotordynamic coefficients K, C, and M are the stiffness, damping, and inertia coefficients representing the response to the displacement, velocity, and acceleration of the rotor center, analogous to those of a mechanical mass-spring-damper system. The present analysis, as is typical for seals, assumes a centered equilibrium rotor position and skew symmetry of the coefficients, where $K_{xx} = K_{yy} = K$ and $K_{xy} = -K_{yx} = k$, similarly for damping and inertia. While often neglected, the cross coupled mass term m is retained in the full coefficient predictions to allow for direct comparison to configurations where only the stiffness coefficients are predicted with a single 0 whirl case, as described in the results below.

The QS method, depicted in Fig. 4.1, transforms the inherently unsteady fluid dynamics problem of the whirling rotor into a steady-state problem by way of a reference frame transformation. Assuming a circular

whirl motion of the rotor about a centered equilibrium position, the reference frame is set to rotate at a speed equal to the whirl speed Ω, the rotor speed is adjusted to the difference between the stationary frame rotor speed and the whirl speed as $\omega - \Omega$, and the stator is set to counter-rotate. Integrated pressures along the rotor surface yield the resulting forces for a particular whirl speed. Considering the rotor to be displaced along the +X axis, those forces become functions of the rotordynamic coefficients and whirl speed according to Eqn. 4.1 as

$$-\frac{F_x}{e} = K + c\Omega - M\Omega^2 \qquad -\frac{F_y}{e} = -k + C\Omega + m\Omega^2 \tag{4.2}$$

Multiple steady state simulations for different whirl speeds then yield frequency independent rotordynamic coefficients according to Eqn. 4.2 based on curve fitting the forces versus whirl speed. This study uses three whirl speed cases, $\Omega/\omega = 0, 0.5, 1$, for each configuration to produce the full set of rotordynamic coefficients. This represents the minimum requirement for quadratic fits based on Eqn. 4.2 and was chosen to limit the computational resources required for the parameter sweep investigation in this paper. Use of five whirl cases for the base case configuration, where $\Omega/\omega = 0, 0.25, 0.5, 0.75, 1$, led to minimal variation in predicted stiffness and damping coefficients, with a maximum difference of 13% for the direct stiffness. Three whirl cases are thus considered sufficient for the present study, though the use of more whirl cases may provide accuracy improvements for particular seal cases and be appropriate for more targeted CFD investigations.

The base model in this study follows the geometry of the experimental test rig used by Marquette et al. [29] due to its relevance to industrial pump applications and use in the subsequent literature as a validation case for both advanced CFD and bulk flow methods (e.g. [57], [22]). The geometry is depicted in Fig. 4.2 showing the full circumference 3D model needed for rotordynamic coefficient prediction (left) and an axial-radial cross-section plane (right). Careful segmentation of the fluid domain into multiple subdomains (bodies) allowed for close control of the grid generation, specifically within the groove regions, that enabled local grid refinement effects to be investigated individually, as discussed below. Note the inclusion of an upstream plenum region, here in its simplest form, and the lack of downstream region, a combination commonly seen in CFD analysis of annular seals despite its potential geometric inaccuracies. The quantitative effect of the inclusion and configuration of these two regions is a primary focus of this study. The seal setup and operating conditions are summarized in Table 4.1. Note that the clearance and radius for the base case differ from the nominal experimental values [29] based on the investigation into centrifugal growth effects, presented in the

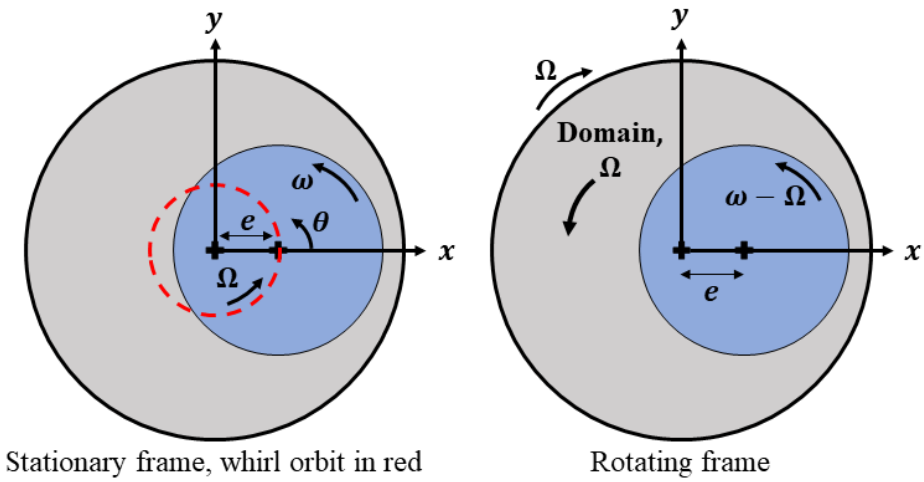

Figure 4.1: Diagram of the quasi-steady (QS) method used for rotordynamic coefficient prediction.

results section. The seal length L describes the seal region only, not including the upstream or downstream lengths.

Simulations were run using the commercial software ANSYS CFX v. 2021 R1 [42] that utilizes a finite volume based solver to evaluate the full discretized Reynolds Averaged Navier Stokes (RANS) equations. Isothermal conditions were employed and fluid temperature was accounted through properly specified density and viscosity. The base model inlet was prescribed by a total pressure equal to the experimentally quoted pressure differential, relying on the assumption of near stagnant flow in the upstream region which is verified by the computational results. The outlet is specified at the seal exit plane in the base case configuration with an average static pressure of 0 gauge pressure. Common choices for turbulence closure include the standard $k-\epsilon$ [58] and shear stress transport (SST) [30] models, which both feature in the CFD literature for turbomachinery applications (e.g. [38, 16]). While extremely robust, the $k-\epsilon$ model has poorer prediction accuracy in near wall regions and in flows with adverse pressure gradients. The SST model utilizes a blended combination of $k-\epsilon$ and $k-\omega$ models to leverage the higher accuracy of $k-\omega$ models in the near wall regions, but it requires more stringent near wall grid refinement, and ultimately increased computational costs, to realize those benefits [59]. The present study employs the $k-\epsilon$ model due to its demonstrated success in similar CFD studies and to limit the computational cost of the large parametric study presented herein. The y^+ value, a nondimensional measure of distance from the wall, is used in CFD to quantify the distance from the wall to the first grid node in relation to the boundary layer profile [60, 42]. The base case grid y^+ values within the seal region fell between 6 and 75, well within an acceptable range when using a

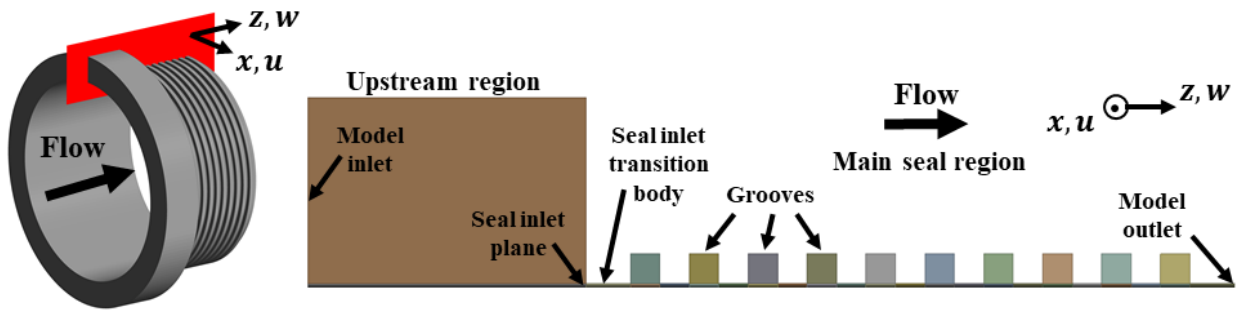

Figure 4.2: Diagram base computational model geometry, highlighting distinct bodies and regions of importance.

Table 4.1: Seal geometry, operating conditions, and setup parameters for the base case model.

Working fluid	Water
Density	984.5 kg/m^3
Dynamic viscosity	5e-4 kg/m s
Rotor speed, ω	24.6 krpm
Pressure differential, Δp	64.5 bar
Seal length, L	34.925 mm
Land length, L_l	1.587 mm
Groove length, L_g	1.587 mm
Groove depth, D_g	1.587 mm
Clearance, c	0.1052 mm
Rotor radius, R	38.2573 mm
Turbulence model	$k-\epsilon$
Inlet	Total pressure
Outlet	Average static pressure
Convergence criteria	Global 1e-7 RMS and/or asymptotic force convergence
Conservation target	1%

wall function approach along with scalable wall treatment in CFX [38]. A two-step local-automatic timescale method was used to avoid convergence issues due to drastically varying time and length scales between the seal region and upstream or downstream regions. Iterative convergence was judged to have occurred when the global RMS residual criteria reached 1e-7 and the integrated rotor surface forces in the normal and tangential directions were stable for several hundred iterations. In some instances, the global RMS criteria was not reached but the forces were well converged, and as such, the results were considered valid and retained.

4.3.1 Base Grid Uncertainty Estimation

An accompanying smooth seal model, matching the geometry of the complementary experimental work by Marquette et al. [61], was used to isolate sensitivity to grid refinement near the seal inlet plane. When combined with extensive grid testing on the present grooved seal, a base grid with 5.86 million elements was identified based on an acceptable comparison to the experimental rotordynamic coefficients (presented in the results section) and the trade-off between accuracy, uncertainty, and computational resources required for a large parameter sweep. A numerical uncertainty estimate was generated using the grid convergence index (GCI) approach by Roache [62]. The results of the GCI estimate are summarized in Table 4.2 for leakage and all rotordynamic coefficients. In short, the prediction results from three successively refined grids are used to assess the influence of discretization on the predicted quantities. The grids are labeled from coarsest (3) to finest (1) and are referenced by the subscripts and superscripts of the variables in Table 4.2. The finest grid (1) used here corresponds to the base case grid. When considering global prediction quantities, the refinement ratio, r, is equivalent to a ratio of the total number of elements between the grids, i.e. $r_{ij} = N_j/N_i$. The grids are chosen such that $r > 1.3$ based on an empirically established and accepted threshold for best results. The final uncertainty estimate, GCI_1^{21}, is an estimate of the numerical uncertainty for the finest grid (1) prediction based on the relative error between the middle (2) and finest (1) grids. A GCI of 0.05, for example, represents a $\pm 5\%$ uncertainty in the predicted value. Thus, GCI_1^{21} serves as an uncertainty estimate for the base case grid used in this study. Note that the theoretical order of convergence $p = 2$ was employed due to non-asymptotic and oscillatory convergence behavior. The relatively high uncertainty in m is attributed to its small magnitude and the consistency of difficulty in its prediction, often being neglected altogether. It is retained in the present analysis to facilitate comparisons with stiffness only predictions, as described in the results below.

The present authors seek to explicitly mention convergence difficulties that arise with the inclusion of upstream and downstream regions in the computational model. Annular seal geometry results in drastically different length scales between the upstream or downstream regions and the seal region. In addition, the flow physics results in widely varying velocity magnitudes and resulting timescales, which create a challenging numerical problem when combined with differing length scales. All results from the present study reveal significantly faster and less troublesome convergence within the seal region, with all convergence problem areas observed to be in the upstream or downstream region, particularly near inlet and outlet boundaries. Avoidance of many convergence issues was achieved through varying timescale selection methods, multistep

Table 4.2: Grid convergence index (GCI) calculations. Grids are labeled from coarsest (3) to finest (1). The finest grid (1) corresponds to the base case grid.

$N_3 \times 10^6$	$N_2 \times 10^6$	$N_1 \times 10^6$	r_{32}	r_{21}			
1.16	2.59	5.86	1.31	1.31			
	$\dot{m}$	K	k	C	c	M	m
GCI_1^{21}	0.001	0.048	0.219	0.123	0.134	0.128	0.573

convergence procedures, and visual convergence criteria. In some instances, minor numerical setup differences led to major qualitative flow field differences. Pugachev et al. [63] highlighted a change in direction of the main vortex when simulating labyrinth seal flow that could only be attributed to use of the multigrid solver option in CFX. The present authors observed a similar effect, where flow fields in the upstream region of an axisymmetric model for different timescale methods became consistent when the multigrid solver was not used. As such, the present authors echo the sentiment by Pugachev et al. that strictly numerical factors may have a non-negligible impact on results, and more careful and widespread verification of flow patterns and any other quantities influencing system performance should be standard practice.

4.3.2 Local Grid Refinement Study

With a base grid established through preliminary mesh sensitivity checks, uncertainty analysis, and experimental comparison, the effect of local grid refinement in isolated sections of the model was quantified to examine which particular model regions require focused refinement efforts. The vast majority of CFD studies for annular seals present grid sensitivity from a traditional global refinement standpoint (e.g. [46]) or do not present sensitivity results at all for brevity (e.g. [12]). Though studies such as these likely complete local grid sensitivity investigations, the results are seldom reported, despite their value in highlighting regions of importance and to link grid sensitivity and convergence issues to flow physics through the identification of potential problem regions. Pugachev et al. [44] describe high levels of refinement needed in tooth tip clearance regions for a gas labyrinth seal model due to high velocity and pressure gradients in these areas, but provide no quantitative results other than a global refinement percent deviation. Hirano et al. [64] perform local grid sensitivity analysis for a gas labyrinth seal by separating the cavities into distinct regions, noting the highest sensitivity coming from the number of elements axially across a cavity. Snyder and Santos [45] utilize local grid refinement on a smooth liquid seal model to establish a final grid based on acceptable GCI results

and computing time. Local grid sensitivity results, specifically for the groove region in grooved annular seals, are thus not yet sufficiently presented and explained in the literature.

The grid sensitivity results presented here focus on the groove regions. Sensitivity is assessed for leakage and stiffness predictions based on the 0 whirl speed case only. Grid manipulation was performed through the growth rate, depicted and defined in Fig. 4.3. Note that when the growth rate is reduced, the number of elements across a region is increased. The effect of the number of elements across the clearance at a constant growth rate of 1 and the number of circumferential elements was also investigated. Note that for all cases except for N_{cl}, the distance from the wall to the first node remained approximately constant, so the y^+ values within the seal region remained unchanged. Sensitivity results are summarized in Fig.4.4 for the four growth rates (a-d), N_{cl} (e), and N_{circ} (f). The growth rate is shown on the top axis (where applicable), while the resulting number of elements N is shown on the bottom axis. The results in each plot are given as a fractional difference compared to the most refined case for that particular parameter variation.

Leakage shows very little sensitivity to any local refinement parameter, with a maximum variation of approximately 1% across all cases, consistent with the extremely low uncertainty given in Table 4.2. Generally, sensitivity for k is higher than for K, suggesting that numerical uncertainty in K may be focused at the seal inlet plane, where the prediction of the stiffness generating Lomakin effect [65] is most prominent, as opposed to within the grooves. This is supported by Fig. 4.4f, where circumferential refinement affects k to a significantly greater degree than K, highlighting the circumferential distribution of pressure as a primary driver of k.

Examining the effect of the four growth rates shown in Figs. 4.4a-d, it is clear that the stiffness coefficients are more sensitive to refinement within the groove, in either direction, than in the clearance or land regions. The total spread in predicted k as a function of $\alpha_{gr,ax}$ is greater than 15%, compared to approximately 4% for $\alpha_{l,ax}$. Similarly, the least refined case for $\alpha_{gr,rad}$ is more than 20% lower than the most refined case, compared to just 3% for $\alpha_{cl,rad}$. Thus, the distribution of pressure and velocity within the groove region is shown to be a highly prominent factor in the prediction of stiffness, where sufficient elements are required to accurately predict the variable variations and their interactions with the clearance flow. Figure 4.4e suggests a noteworthy dependence on the number of elements across the clearance, but further analysis regarding the relationship between N_{cl} and near wall turbulence modeling is necessary for a definitive conclusion.

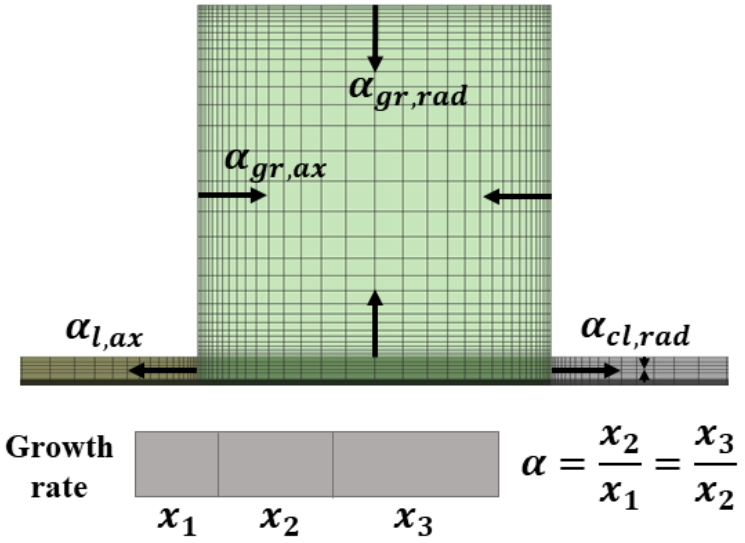

Figure 4.3: Sample grid within the groove region, showing the specific refinement growth rates and definition investigated in the local grid refinement study.

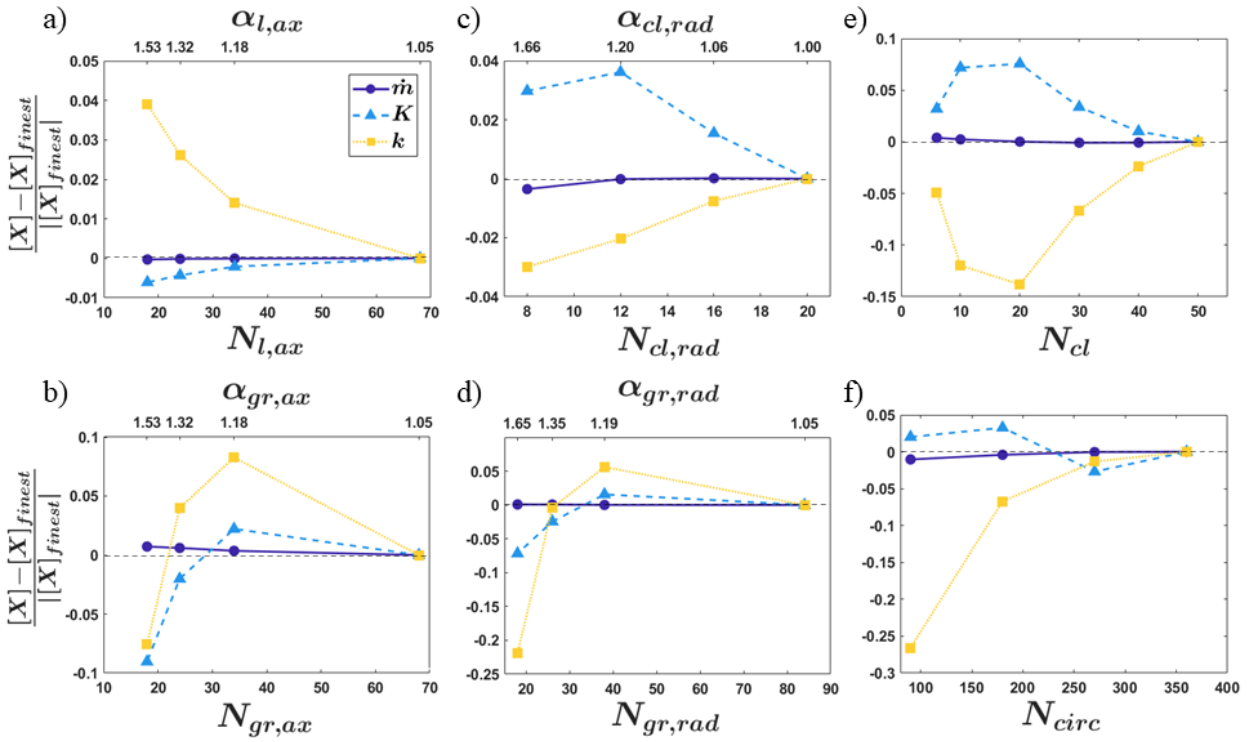

Figure 4.4: Leakage and rotordynamic coefficients vs. local mesh refinement quantities for targeted mesh sensitivity investigation. Top axes are the growth rate (where applicable), bottom axes are the associated number of elements across the specified region. Shown is a fractional difference compared to the most refined grid in each case, i.e. the rightmost data point on each plot.

4.4 Results and Analysis

Having established a base case model and grid, estimated numerical uncertainty, and examined local grid sensitivity in the previous sections, this section focuses on model sensitivity due to various geometric and model setup parameters. A comparison of the base model predicted coefficients to the experiments is presented first. A close examination of the effect of the upstream and downstream region configuration and inlet and outlet boundary condition is given next, including specific analysis of the flow physics dictating the observed changes in predictions. Finally, prediction sensitivity to centrifugal growth effects and modeling whirl amplitude are investigated. Note that subsections below correspond to subsections of the literature survey as previously discussed.

A summary of the quantitative results analyzed in the next sections is given in Table 4.3. Note that the base model includes an adjusted clearance and rotor radius to account for centrifugal growth (discussed below) after preliminary testing indicated an improved prediction of leakage when including this effect. The leakage and all predicted coefficients for the base model fall within 30% error compared to the experimental results given in [29] except for k. Marquette et al. [29] make note of observing rotor runout equal to 25% of the seal clearance. While not giving an explicit definition for the runout they observe, they hypothesize that this created a pumping effect that drove the fluid into rotation. The present authors hypothesize that this effect is the likely cause of the large predicted error in k, as the preswirl and development of circumferential velocity is known to significantly affect k, mostly independent of the other coefficients. Preliminary simulations to account for this runout effect using the QS method with the frozen rotor assumption produced unverified results, confirming the inability of the QS method to account for this phenomena due to geometric asymmetries and the known inaccuracies of the frozen rotor assumption.

4.4.1 Upstream Region

The influence of the inclusion of an upstream region and its configuration, along with the associated inlet boundary condition, is quantitatively investigated in this section. A diagram of the upstream configurations simulated in this study is given in the top of Fig. 4.5, where dashed lines with arrows represent the inlet boundaries. The base seal model configuration (A) includes an upstream region 15mm and 10mm in length and height respectively. Configuration B includes a radial inlet slot covering the entire seal circumference as well as a symmetry boundary condition (dotted line in configuration B of Fig. 4.5) to represent a back-to-back

Table 4.3: Results for various upstream configurations, inlet boundary conditions, downstream configurations, and clearances for different centrifugal growth models. Also included are the experimental results for the same geometry seal by Marquette et al. [29]. Dimensional uncertainty windows for each quantity corresponding to the GCI values in Table 4.2 are included in the top row.

	Model	$\dot{m} \pm 0.001$ [kg/s]	$K \pm 0.09$ [MN/m]	$k \pm 0.45$ [MN/m]	$C \pm 1.13$ [kN s/m]	$c \pm 0.84$ [kN s/m]	$M \pm 0.46$ [kg]	$m \pm 0.30$ [kg]
1	Experimental [29]	0.807	-2.04	5.07	8.43	8.80	3.77	-
2	Base case (A)	0.802	-1.81	2.06	9.16	6.24	3.56	-0.52
3	Radial inlet upstream (B)	0.801	-2.01	2.58	9.14	6.41	3.59	-0.38
	Longer upstream (C)	0.801	-1.98	3.36	9.22	6.47	3.63	-0.34
	No upstream, same BCs (D)	0.880	-4.60	-1.10	6.24	5.47	3.28	-0.44
4	No upstream, mass flow inlet (E)	0.802	-0.76	3.75	11.13	7.13	4.64	-0.26
	No upstream, static pressure (F)	0.810	-4.29	2.00	5.73	5.96	3.29	-0.35
5	Radial outlet downstream (G)	0.820	-3.65	3.91	10.90	7.71	3.96	-0.41
	Axial outlet downstream (H)	0.802	-1.73	2.30	9.46	6.23	3.49	-0.58
6	$c = 0.1105$mm (nominal)	0.868	-1.61	1.95	9.19	6.06	3.48	-0.51
	$c = 0.1029$mm (linear)	0.774	-1.89	2.12	9.14	6.33	3.60	-0.52

experimental setup. This setup is common to seal rigs and was used by Marquette et al. [29], though the geometry is often approximated by an axial inlet boundary similar to configuration A. A longer upstream region (30mm, double the length of the base case) with an axial inlet boundary is also studied and is shown by configuration C. Configurations A-C were all simulated using a total pressure inlet boundary condition equal to the prescribed pressure differential, relying on the assumption of near stagnant flow in the upstream region. Lastly, several cases with no upstream region and varying inlet boundary conditions were investigated (cases D-F). Configuration D employs an inlet boundary condition that matches configurations A-C.

Sections 2 and 3 of Table 4.3 show the predicted leakage and rotordynamic coefficients for varying upstream region configurations. Comparison of the cases with an upstream region of varying geometry (A-C) shows that leakage predictions remain almost identical, as do both damping and mass coefficients. A slight decrease in direct stiffness is observed for the radial and longer axial upstream cases as compared to the base

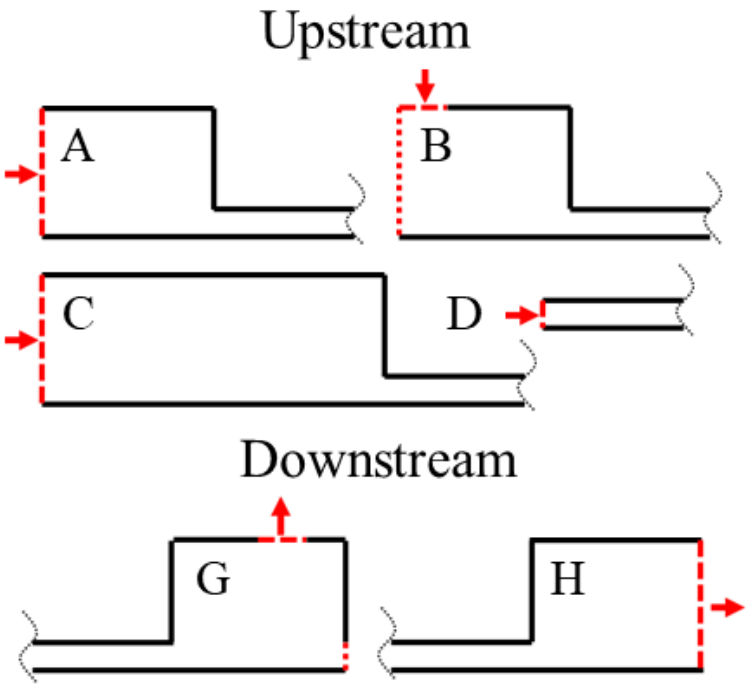

Figure 4.5: Geometries of the upstream and downstream regions examined in this study. Inlet and outlet boundaries indicated by the dashed line. The vertical dotted line in configuration B indicates a symmetry condition. The vertical dotted line in configuration G indicates a free slip wall condition.

case, though this difference is at most 11%. The primary discrepancy lies in the predicted cross-coupled stiffness, as seen in the 25% and 63% increases for configurations B and C respectively. Given the uncertainty estimate for the base case cross-coupled stiffness, the present results indicate that, within an allowable range, the radial inlet with symmetry configuration (B) may be sufficiently approximated by the axial inlet boundary configuration (A), which may be desirable in order to reduce model complexity. Without an upstream region, configuration D predicts a 10% larger leakage since no pressure drop is accounted for at the seal inlet plane. Significant errors in predicted stiffness are also seen for this configuration, including a considerably underpredicted k.

Figure 4.6 displays contour plots of the perturbed pressure extracted axially and circumferentially along a mid-surface at $0.5c$ for configurations A-D. Note that p_0 corresponds to the circumferentially averaged pressure at each axial location, and that the perturbed pressure is nondimensionalized by the bulk axial dynamic pressure at the seal inlet plane ($z/L = 0$). The pressure perturbation within the upstream region ($z/L < 0$) is negligible and only the main seal region ($0 \leq z/L \leq 1$) is shown here. Recall that the model setup has the rotor eccentric along the x axis ($\theta = 0$), as shown in Fig. 4.1. Near the seal inlet plane, the

restoring force due to the Lomakin effect [65] is observed, where positive and negative pressure perturbation occurs near the minimum and maximum clearance locations, respectively. Further downstream, high and low pressure regions develop in the circumferentially converging and diverging film sections, respectively, due to the circumferential pumping effect of the rotor surface motion. This is indicative of the viscous wedge effect that creates a destabilizing force in the positive y axis direction for the given rotor eccentricity and is more prominent when the circumferential velocity is higher. The Lomakin and wedge effects are known to be primary factors influencing the direct and cross-coupled stiffness, respectively. The pressure contours for cases A-C display similar behavior, apart from the region in case C highlighted by the dashed oval in Fig. 4.6 for $0.1 < z/L < 0.3$. Here, the perturbation caused by the wedge effect is seen to extend further upstream without altering the perturbation near the seal inlet plane. While displaying the same core features, the contour for case D visibly differs from cases A-C, clearly demonstrating that the same boundary conditions without an upstream region is not an appropriate approximation for the observed flow physics.

The increased prominence of the wedge effect in the case C contour and the isolation of the cross-coupled stiffness as the differing coefficient across configurations A-C points to a variation in net circumferential velocity within the seal as the mechanism driving flow field and performance changes. Since all other conditions remain constant, changes in net circumferential velocity are predominantly caused by the development of circumferential velocity, or preswirl, within the upstream region, as suggested and seen in similar CFD studies for annular seals (e.g. [47]). Figure 4.7 displays circumferential velocity contours in the axial-radial plane for cases A-D, normalized by the rotor surface speed, ωR. Clearly, the highest circumferential velocity at the seal inlet plane is observed for configuration C, as the longer upstream region provides more time for the circumferential velocity to develop. While configurations A and B show qualitatively different flow fields within the upstream region, near the seal inlet plane the circumferential velocity becomes relatively consistent. Further examination of the developed preswirl is shown in Fig. 4.8 which depicts the axial profile of nondimensional circumferential velocity, $u/\omega R$. Note that the profile is taken across an axial line at $0.5c$, the midspan of the seal clearance. The sharp drop in u at the seal inlet plane is due to the artificially high value in the upstream region, as the extracted values are near the rotor surface and do not represent the bulk circumferential velocity magnitude since much of the flow in this region is nearly stagnant. A similar profile was observed by Mortazavi and Palazzolo [16] for their groove-on-rotor CFD case. In accordance with earlier observations, the longer upstream region results in a clearly higher preswirl magnitude, while the radial and axial inlet upstream cases with the same dimensions are close to indistinguishable. No preswirl

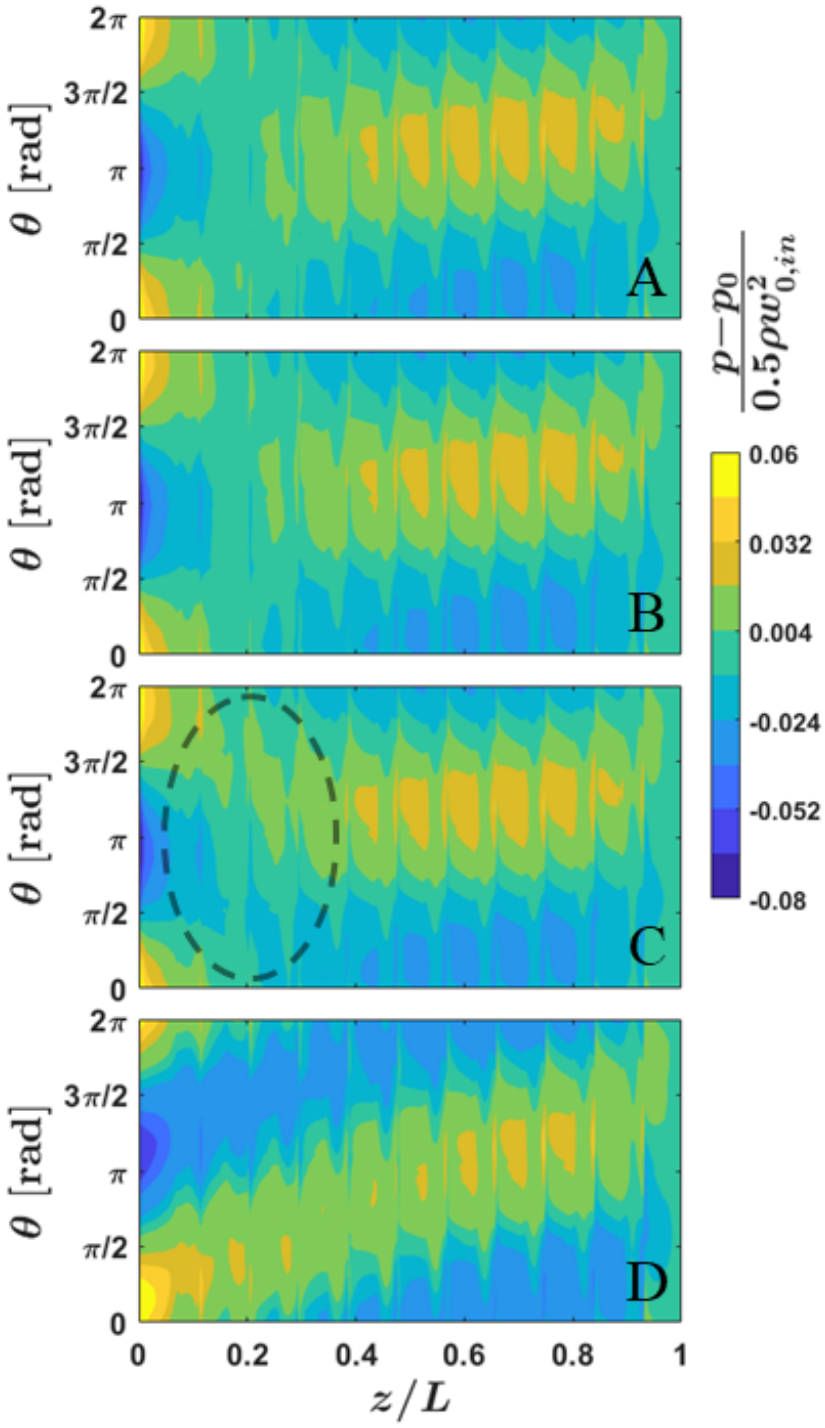

Figure 4.6: Axial-circumferential perturbed pressure contours for cases with varying upstream geometry. Values are extracted from a surface at $0.5c$. In the contour value, p_0 is the bulk pressure at each axial location and $0.5\rho w_{0,in}^2$ is the bulk axial dynamic pressure at the seal inlet plane. Pressure perturbation is negligible within the upstream region ($z/L < 0$) and is not shown here.

is predicted by configuration D. All cases show a swirl ratio profile that converges to just below 0.5, as expected for incompressible grooved seals. The pressure contour and preswirl profile similarity between cases A and B supports the agreement in predicted rotordynamic coefficients, reinforcing the use of an axial inlet geometry as a reasonable approximation to the radial inlet, back-to-back configuration. This analysis confirms the dependence of the cross-coupled stiffness on the upstream region geometry through the predicted development of preswirl.

Despite most authors agreement that an upstream region is necessary for accurate rotordynamic CFD predictions for annular seals, studies are continually performed without one (e.g. [45]), and a comprehensive analysis regarding the necessary boundary condition adjustments and assumptions is rarely provided. In order to quantitatively confirm what the upstream region provides in terms of flow dynamics, additional simulations were run (cases E and F in section 4 of Table 4.3) using the same geometry as configuration D, namely no upstream region, while varying the boundary condition. In case E, a mass flow was specified at the inlet that matched the base case leakage prediction, and in case F, a static pressure was prescribed that resulted in a leakage prediction close to the base case. For both E and F, the inlet velocity direction is chosen to match the preswirl value of the base case (A) to eliminate the preswirl dependence described in the comparison of cases A-C above. Comparing cases A, E, and F in Table 4.3, we see large discrepancies in the predicted values for K, k, and C. A close examination of the pressure distribution is conducted at the seal inlet plane, where the boundary condition is specified for cases D-F and thus where the most prominent flow field differences are expected. Figure 4.9 display the circumferential profile of the perturbed pressure at this location for cases A, E, and F. The static pressure boundary condition explicitly prescribes the pressure at the boundary and inherently allows for no pressure perturbation, resulting in a uniform pressure profile at the seal inlet plane for case F. When a mass flow is prescribed in case E, a non-uniform circumferential pressure profile is free to develop but is not in phase with the naturally developing profile predicted by case A with an upstream region. The base case (A) has a peak pressure almost exactly at the location of minimum film thickness ($\theta = 0$, in the direction of eccentricity), again indicative of the Lomakin effect dominance in this region. The mass flow inlet case (E), however, has a peak pressure that lags slightly behind. Thus, despite explicitly matching the known leakage and allowing for a non-uniform circumferential pressure profile at the boundary, a mass flow specified inlet is still unable to correctly predict the flow dynamics at the seal inlet plane. This leads to the significantly differing rotordynamic coefficient predictions, as seen in Table 4.3.

The cases discussed above quantitatively examine the influence of the upstream region configuration and

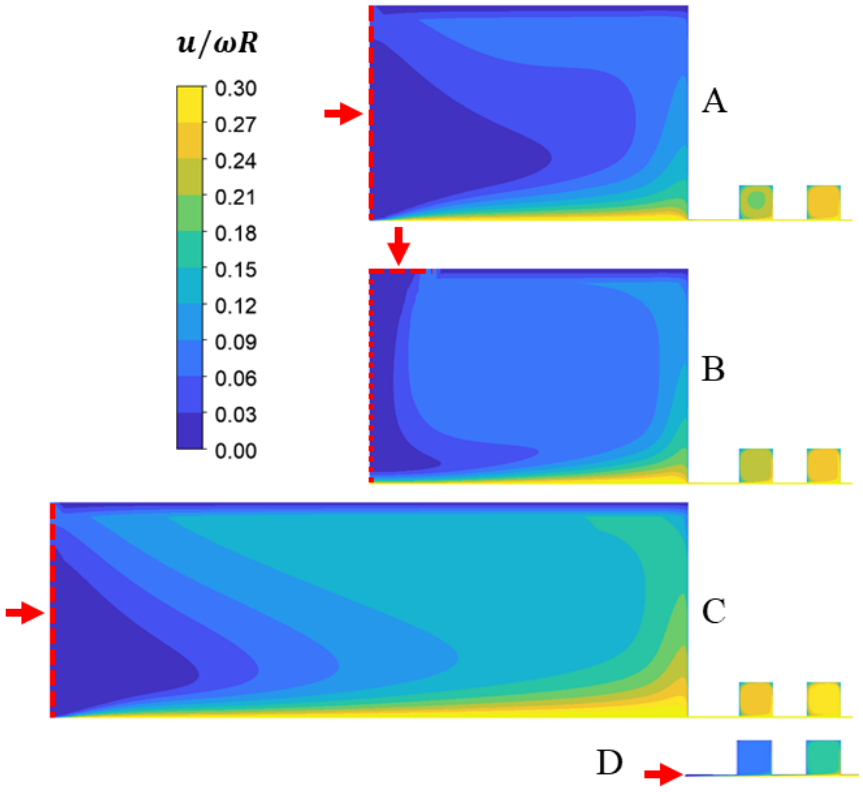

Figure 4.7: Contours of circumferential velocity, nondimensionalized by rotor surface speed, for the four upstream region configurations.

the relationship between the naturally developing flow field and the seal inlet plane boundary conditions. The results confirm the dependence of the cross-coupled stiffness on the development of the circumferential velocity, which is a strong function of upstream region geometry. They also show that an upstream region with an axial inlet may be a viable modeling approximation to a back-to-back seal configuration provided the predicted preswirl remains consistent. The cases without an upstream region show that, when included, the upstream region naturally predicts preswirl, leakage, and a circumferential distribution of pressure at the seal inlet plane. A priori knowledge of all three quantities, while rarely known, is necessary should an upstream region be omitted from the model. Despite eliminating the need for empirical inlet loss and preswirl coefficients as in bulk flow methods, a similar level of uncertainty may still exist in a full CFD method if any arbitrary upstream region is used. Experimentally accurate upstream regions should thus be employed in CFD studies and reported in detail by experimentalists whenever possible.

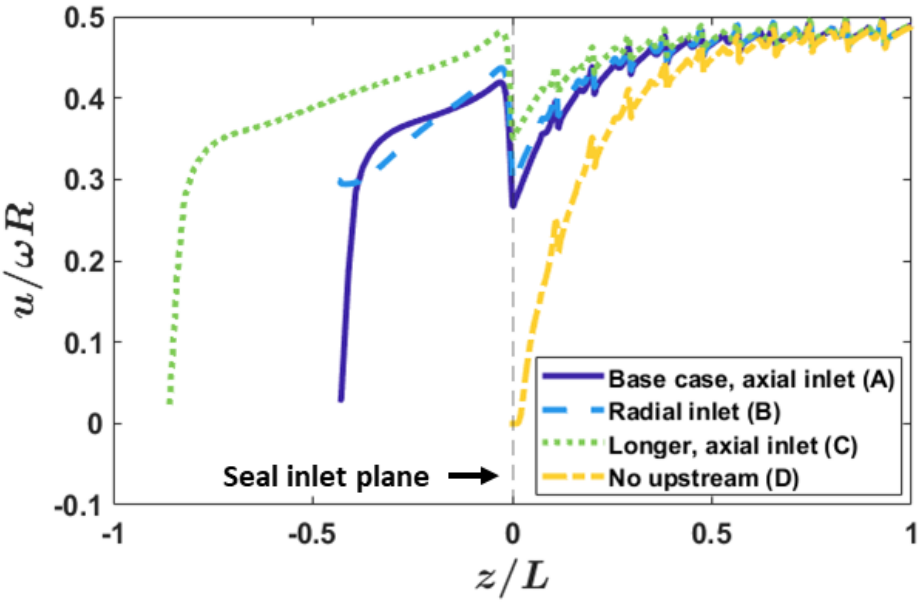

Figure 4.8: Axial profile of circumferential velocity, nondimensionalized by rotor surface speed, for the four upstream region configurations.

4.4.2 Downstream Region

In addition to the upstream region, cases were run with various downstream region configurations, a topic with much less direct coverage in the literature. The results allowed for investigation into the flow physics in this subdomain and its potential influence on predicted rotordynamic coefficients. Two additional cases were considered whose geometries are shown in the bottom of Fig. 4.5. In both configurations G and H, the base case upstream region is included. The downstream region dimensions are 15mm and 10mm for length and height respectively, matching those of the upstream region. Configuration G contains a radially directed outlet slot covering the entire seal circumference specified by 0 gauge average pressure, along with a small radial free slip wall adjacent to the rotor surface to represent conditions similar to a gasket. Configuration H employs an axially directed outlet along the full radial extent of the boundary. Note that the radial equilibrium boundary condition in CFX [42] was used for configuration H that enforces a prescribed average static pressure within multiple circumferential bands. This was chosen due to the expected radial pressure profile caused by the swirling flow and observed convergence issues with other boundary conditions.

Section 5 of Table 4.3 shows the predictions from the radial and axial outlet downstream region cases (G and H). The slightly higher leakage prediction from case G is a result of the 0 gauge pressure boundary

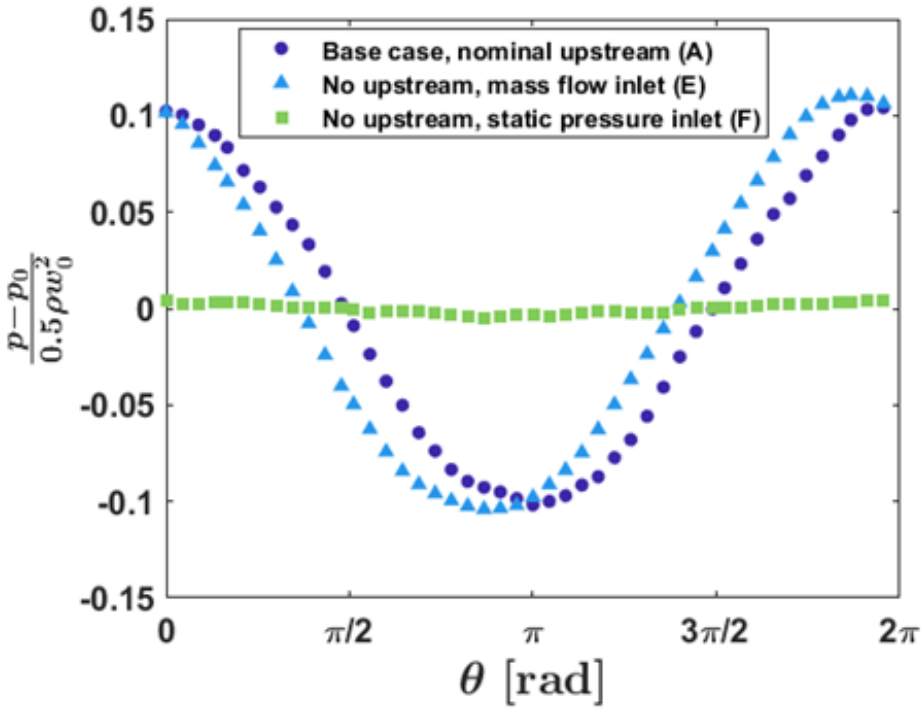

Figure 4.9: Circumferential profile of pressure, nondimensionalized by the dynamic pressure, at the seal inlet plane for cases A, E, and F.

condition being located radially away from the seal exit plane. This creates a low pressure region closer to the rotor surface that artificially increases the pressure drop through the seal. Both stiffness coefficients for configuration G differ in magnitude by greater than 90% as compared to the base case, while the damping coefficients are only slightly higher. Configuration H, on the other hand, predicts stiffness coefficients within 12% of the base case and damping coefficients that vary only marginally. Flow fields and pressure distributions in the upstream and seal regions for cases A, G, and H showed only minor discrepancies, as described below. This indicates that any influence of the downstream region on the predicted forces is mostly isolated from the upstream seal dynamics.

In order to consider the distinct contributions from different regions, Table 4.4 separates the stiffness generated by pressure perturbation within seal ($z/L < 1$) from that within the downstream region ($z/L > 1$). The seal region stiffness coefficients for the base case (A) in Table 4.4 match those in Table 4.3 exactly, as this configuration does not include a downstream region. For cases G and H, the sum of the seal and downstream region contributions in Table 4.4 are equal to the overall stiffness results in Table 4.3. The downstream region stiffness coefficients are notable for case G, both reaching above 70% of the total base

case coefficients. Alternatively, the downstream region coefficients for case H are minimal. The seal region stiffness coefficients for cases G and H are in good agreement with the base case results. This further suggests that the influence of the downstream region is mostly confined to the downstream region itself and does not significantly affect the upstream flow.

Figure 4.10 displays perturbed pressure contours for cases G and H, analogous to those in Fig. 4.6, for a closer examination of the physical influence of the downstream region. Within the seal region, the pressure distribution of cases G and H are very similar and closely match that of case A shown in Fig. 4.6, apart from a small region near the seal outlet plane for case G. The same Lomakin and wedge effects described above are clearly seen in cases G and H. The pressure is nearly uniform within the downstream region of configuration H, reflective of the minor downstream stiffness contributions for this case in Table 4.4. Configuration G shows a discernible, non-uniform pressure in the downstream region, leading to the significant downstream stiffness contributions quantified in Table 4.4. This is seemingly a result of the wedge effect pressure perturbation within the seal not equilibrating in the downstream region, instead continuing through the seal outlet plane and into the downstream region where it is confined by the geometry. The small area of differing behavior near the seal outlet plane in case G likely accounts for the small remaining discrepancy between its seal region only contributions and the base case stiffness predictions. Clearly, non-negligible pressure perturbations can develop in the downstream region depending on its geometry and the location of the outlet boundary. Since the influence on predicted rotordynamic coefficients can be significant, this highlights the importance of using an experimentally accurate geometric model for the downstream region.

The average static pressure boundary condition in CFX employs, by default, some amount of smoothing of the pressure profile along with the enforced average over the entire boundary. This effect is specified through a blend coefficient and meant to aid simulation convergence and robustness [42]. The base case (A) without a downstream region employs this blending as part of the outlet boundary condition, and as a result, the pressure is seen to equilibrate just before the seal outlet plane. Similar behavior naturally develops near the seal outlet plane for case H, but not for case G where significant downstream force contributions were observed, as discussed above. Further investigation sought to quantify the influence of this boundary condition specification when employed at the seal outlet plane, including its potential to enforce artificial boundary physics and its capacity to approximate the net influence of a downstream region. Additional cases (J1-J3) were run using the same model setup as the base case while varying the value of the blend coefficient. Note that a lower blend coefficient means less enforcement of a uniform profile, e.g. a blend factor of 0

Table 4.4: Stiffness coefficients for various downstream configurations and outlet boundary conditions, separately considering the contributions from the seal ($z/L < 1$) and downstream ($z/L > 1$) regions.

	$z/L < 1$		$z/L > 1$	
Model	K [MN/m]	k [MN/m]	K [MN/m]	k [MN/m]
Base case (blend=5%) (A)	-1.81	2.06	–	–
Radial outlet downstream (G)	-2.19	2.46	-1.46	1.45
Axial outlet downstream (H)	-1.81	2.10	0.08	0.20
No downstream, blend=0.5% (J1)	-1.85	2.09	–	–
No downstream, blend=0.1% (J2)	-2.02	2.21	–	–
No downstream, blend=0.01% (J3)	-3.65	3.33	–	–

indicates a freely varying pressure with no limitations other than the specified average.

The bottom of Table 4.4 includes the stiffness predictions for cases J1-J3, where the seal region contributions are equal to the total stiffness results due to the lack of downstream region in the model. When combined with the base case, blend factors between 0.01 and 5% are considered. As the blend factor is reduced and the boundary pressure is allowed to vary more freely, the magnitude of both stiffness coefficients increases. Up to 100% differences between the highest (A) and lowest (J3) blend cases are observed. Stiffness coefficients for case J3 are also seen to be reasonably close in magnitude to the total results of the radial outlet downstream case (G in Table 4.3). This suggests a potential similarity between the blend coefficient and empirical factors employed in bulk flow methods at the seal outlet (e.g. exit recovery coefficient) meant to approximate the flow physics of the downstream region. The perturbed pressure contour associated with case J3 is also shown in Fig. 4.10. Instead of the equilibration observed in the base case, the perturbed pressure magnitude continues to grow up to the seal outlet plane. The location of the peak pressure remains approximately constant throughout the seal, consistent with the wedge effect described above, but the magnitude is almost doubled near the exit plane. Clearly, the value chosen for the blend coefficient has a significant influence on the resulting pressure distribution and thus the predicted coefficients. Comparison between cases G and J3 suggests that a model with a properly specified blend coefficient in lieu of a downstream region may provide sufficiently accurate rotordynamic coefficient predictions. The blend coefficient value to achieve this, however, will rarely be known a priori. Thus, without explicit determination of an appropriate blend coefficient, its use becomes equivalent to an unvalidated empirical coefficient.

This section quantitatively examined the influence of the downstream region and its configuration on

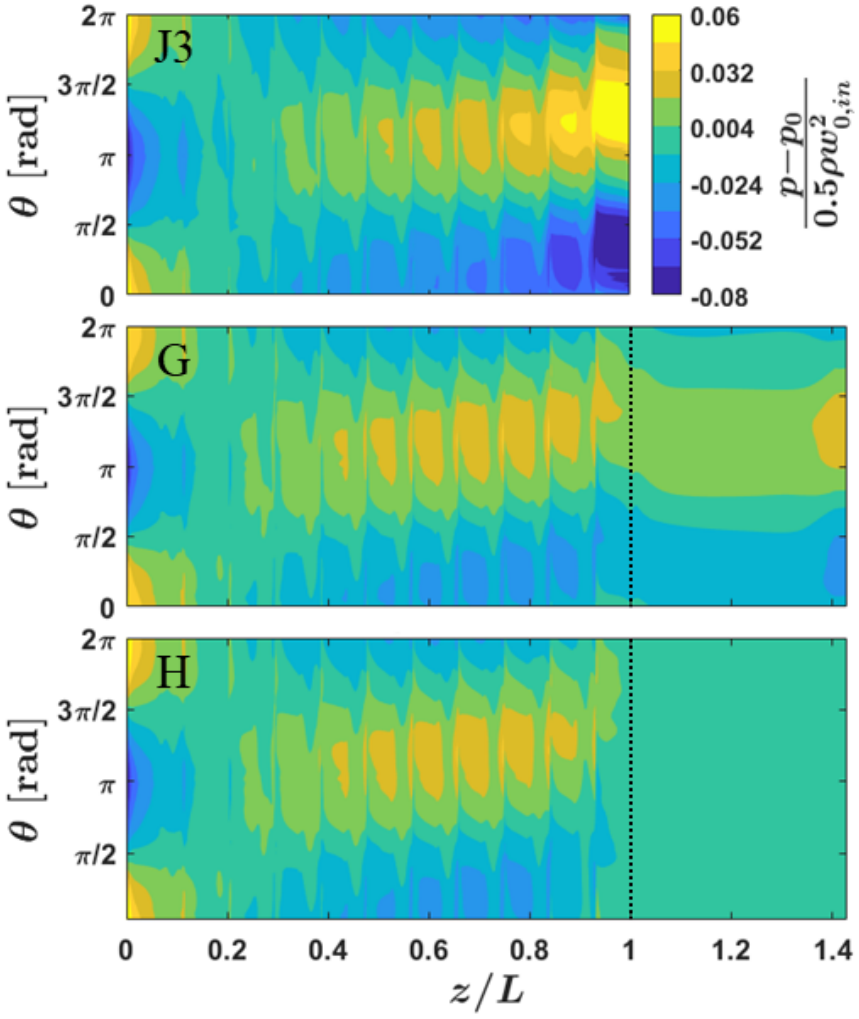

Figure 4.10: Axial-circumferential perturbed pressure contours for cases with varying downstream geometry and outlet boundary condition. Values are extracted from a surface at $0.5c$. The same contour value as in Fig. 4.6 is plotted here. The seal outlet plane at $z/L = 1$ is indicated by the vertical dashed line.

rotordynamic coefficient prediction. It also considered the impact of specific outlet boundary condition specifications and their relationship to the downstream region flow physics. The results show that non-negligible contributions to the developed forces may occur within the downstream region for particular configurations, resulting in changes in stiffness coefficients potentially upwards of 100%. The stiffness developed in the downstream region is mostly isolated from the forces generated within the upstream and seal regions. While rarely considered as a crucial parameter, the amount of pressure profile blending at the seal exit plane is shown to have a significant influence on the predicted stiffness coefficients. The blend coefficient thus represents an additional empirical parameter that exists within the CFD model when the downstream

region is neglected. Similar to the treatment of the upstream region, experimentally accurate downstream region modeling is required in order to realize the accuracy improvements afforded by CFD methods over the empirical coefficient treatment of the downstream region in bulk flow methods.

4.4.3 Rotor Centrifugal Growth

Section 6 of the results in Table 4.3, along with the base case results, describe the effect of accounting for rotor centrifugal growth on the predicted leakage and rotordynamic coefficients when using the QS model. The experimental work by Marquette et al. [29] quotes an initial measured (nominal) radial clearance of $c = 0.1105$mm, noting that proximity probe measurements during testing observed a 4% decrease in clearance between the low and high running speeds (10200 and 24600 rpm). Based on this quoted percent change, the present authors executed simulations with a clearance assuming rotor growth to be linear and quadratic functions of rotor speed, as done by Storteig [66] and Xia et al. [57], respectively. When considered, centrifugal growth is often approximated with a quadratic function based on Roark's formula for stress and strain [67], which requires knowledge of the material properties of the rotor. As mentioned above, the base case includes an adjusted clearance ($c = 0.1052$mm) based on preliminary simulations that predicted leakage much closer to the experimentally reported values, similar to the approach by Moore [46] in their well established CFD study.

As expected, clearance adjustment has the most prominent effect on leakage, where a less than 7% decrease in clearance results in a greater than 10% reduction in leakage. Though not often explicitly quantified in CFD studies and methods, the physical mechanism dictating this is well understood, as a tighter clearance increases the shear frictional forces along the seal length, resulting in a reduction in the mass flow created by the same axial pressure drop. The direct stiffness is similarly affected, as the same clearance reduction results in a 17% reduction in K (though an increase in magnitude). Slight decreases in clearance effectively decrease the restoring force due to the Lomakin effect [65], since the difference in clearance between the side in the direction of eccentricity and the opposite direction is reduced. The cross-coupled stiffness and both damping and mass coefficients show negligible change across the clearance range tested when compared to the estimated numerical uncertainties.

While the fluid mechanisms driving the changes in leakage and rotordynamic coefficients with small clearance adjustments are well understood, the quantitative influence of the adjustment on the modeling results is infrequently presented. These results substantiate the claim that, when employing the QS method

for grooved seal performance prediction, the effect of rotor centrifugal growth is non-negligible and must be measured and reported experimentally to be included in the model.

4.4.4 Whirl Amplitude

Quantification of the effect of modeling whirl amplitude on the leakage and rotordynamic coefficients is shown in Fig. 4.11. Whirl amplitude was varied by altering e (see Fig. 4.1) in the geometric model used for all three whirl speed cases. For each whirl amplitude value, the same grid parameters, boundary conditions, and geometry (apart from e) were used to isolate the effect of the modeling whirl amplitude. As described above, the most common modeling choice for whirl amplitude ratio is $\varepsilon = e/c = 0.1$, which was used in the base setup of this study. As such, the results in Fig. 4.11 are presented in terms of fractional differences from the base case predicted values. The shaded regions represent an uncertainty bound for the indicated value predicted using the base case (see the top row of Table 4.3 for the magnitude uncertainty values for each coefficient). In the discussion below, an arbitrary threshold of 10% is used to assess when deviation from linearity is observed for the predicted coefficients.

The change in leakage with increasing whirl amplitude is shown in the top of Fig. 4.11. Note that no uncertainty bound is shown for leakage since the calculated GCI was 0.001 and is thus visibly negligible on the plot. As expected, leakage increases with whirl amplitude, as the higher eccentricity creates a larger effective clearance due to the widening gap in the direction opposite the rotor displacement. The increase in leakage on the wider side outweighs the reduction in leakage on the eccentric side, and the net leakage increases as a result. Variation in leakage above 10% is seen for whirl amplitudes greater than 0.6, indicating a higher sensitivity to whirl amplitude than to most other modeling and grid parameters.

The top plot of Fig. 4.11 also displays the direct and cross-coupled stiffness as functions of whirl amplitude. Note that the uncertainty in k is not displayed since the GCI was 0.219 and would encompass the full range of the plot. The deviation in k remains below 5% across the entire whirl amplitude range. Coupled with the relatively higher uncertainty estimation, this indicates a small influence of whirl amplitude on k. Changes in whirl amplitude will sightly alter the cross-film velocity profile but not significantly, leading to minimal change in k since it is primarily driven by the development of circumferential velocity. The direct stiffness is seen to increase with whirl amplitude as the higher eccentricity increases the centering Lomakin effect that drives the positive contribution to K. The value for K deviates by greater than 10% from the

base value only when the whirl amplitude exceeds 0.7, indicating that the traditionally accepted 0.5 linearity threshold may be conservative for the type of case examined here.

Direct and cross-coupled damping are seen to decrease and increase with whirl amplitude, respectively, as seen in the middle plot of Fig. 4.11. As the whirl amplitude increases, the amount of fluid remaining in the gap between the rotor and stator decreases. This fluid opposes the whirl motion and is responsible for the direct damping force, so the direct damping decreases as a result.

The bottom plot of Fig. 4.11 displays the direct and cross-coupled mass coefficients versus whirl amplitude. Direct mass, known to be of importance to incompressible liquid seal applications, is seen to increase with whirl amplitude as the larger trajectory whirl amplitude increases the added mass (inertial) contribution to the normal force component. A deviation above 10% from the base case, and outside the estimated base case uncertainty in M, is observed for e/c above 0.5, in agreement with the 0.5 threshold asserted for static eccentricity. While partially attributed to the small magnitude, whirl amplitude is shown to have the most influence on M as compared to the other coefficients. The cross-coupled mass decreases slightly and then increases with whirl amplitude, though all predicted values fall within 10% of the base value. As discussed above, m is notoriously difficult to measure and predict and is often neglected in seal analysis, so its high uncertainty estimation (GCI of 0.573) is not displayed on the plot and its variation across the whirl amplitude range is not considered significant.

The current investigation presents a quantitative analysis of the influence of modeling whirl amplitude, up to $e/c = 0.8$, on the predicted rotordynamic coefficients for an incompressible grooved seal when using the QS method. This extends the coverage in the literature to fully encompass incompressible grooved seal cases and to include higher whirl amplitude predictions. Qualitative trends match the physical understanding and limited previous predictions, while the present results indicate the traditionally accepted linearity threshold of $e/c = 0.5$ may be a conservative estimate in the conditions of this study, particularly for the stiffness coefficients.

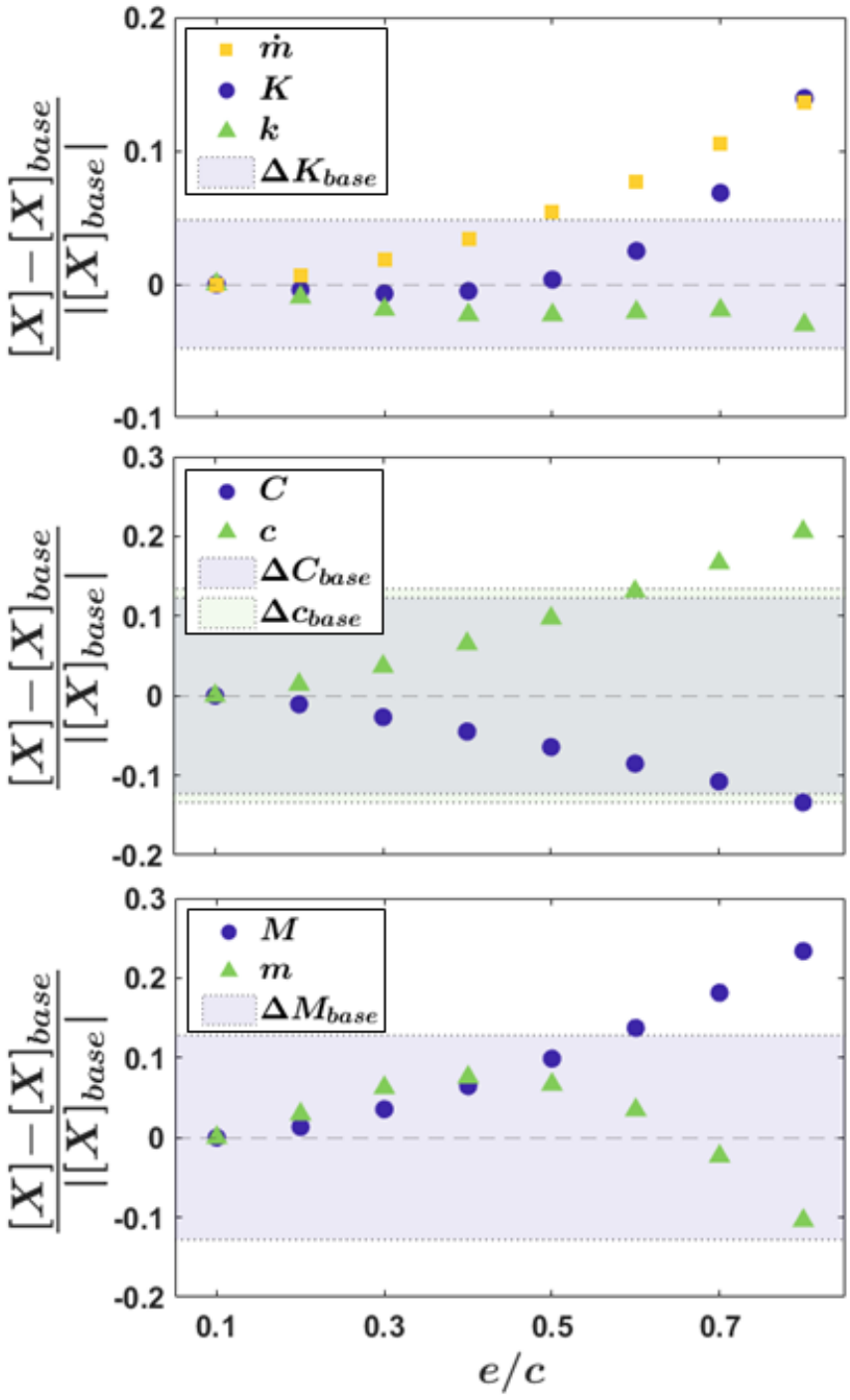

Figure 4.11: Predicted rotordynamic coefficients vs. modeling orbit radius. The uncertainty for leakage is less than 0.1% and is not shown on the top plot. The uncertainties for k and m are 0.219 and 0.573 respectively and cover the range of the data for those quantities in their respective plots, so these uncertainties have been omitted from the plots for clarity.

4.5 Conclusions

This study presents a quantitative and comprehensive analysis of the sensitivity of rotordynamic coefficient predictions to various modeling and setup parameters when using the quasi-steady (QS) method with an incompressible grooved seal model. Close examination of the effect of local grid refinement within the groove regions highlighted the importance of a refined grid within the groove region in order to resolve pressure and velocity gradients and their interactions with the clearance flow. Variation of the upstream region configuration confirmed the strong influence of the development of circumferential velocity on the cross-coupled stiffness, which varied up to 63% for the longer length upstream region. A simpler, axial inlet configuration is shown to be a reasonable approximation to the experimentally accurate radial inlet with symmetry model in this case. The upstream region is proven to provide naturally developing predictions for leakage, preswirl, and circumferential distribution of pressure, which all must be specified if an upstream region is omitted from the model. Depending on the configuration of the downstream region, significant pressure perturbations can develop that lead to greater than 90% changes in stiffness magnitude, mostly independent from the flow within the seal region. Without a downstream region, sensitivity to the amount of pressure profile blending at the seal outlet plane is demonstrated, further highlighting the need for an experimentally accurate downstream region if unvalidated empirical coefficients are to be avoided. Observed 10% and 17% reductions in leakage and direct stiffness, respectively, across rotor centrifugal growth ranges confirm the need to account for this effect, both through dynamic experimental measurements and modeling. Cases with increasing whirl amplitude ratio up to 0.8 demonstrate non-negligible sensitivity, though the often adopted linearity threshold of 0.5 may be conservative in cases similar to the one investigated here. Neglecting or improperly modeling these subdomains and effects can severely diminish model accuracy as their poor treatment in a CFD method may not provide much improvement over treatment with empirical coefficients in simplified bulk flow methods. The results of this paper suggest best practice guidelines when applying CFD methods to grooved annular seals, beginning with uncertainty estimation and local grid refinement studies to ensure numerical uncertainty is accounted and that a sufficiently refined grid within the groove region is used. Best results will be obtained when the most accurate model geometry is employed, including experimentally accurate upstream and downstream regions and an adjusted running clearance, where appropriate.

The investigation in this paper is the first to provide a comprehensive and quantitative analysis of the influence of the aforementioned modeling features on rotordynamic coefficient prediction, specifically for

an incompressible grooved seal and when using the QS method. By supplying quantitative results on the sensitivity to upstream and downstream configuration, rotor centrifugal growth, and modeling whirl amplitude, this paper provides a deeper understanding of how these modeling aspects affect CFD predictions specific to grooved annular seals. The discussion herein is based on results for a liquid seal case. While the quantitative results may not directly apply to gas seal models, the overall conclusions and suggested guidelines can be equally considered for compressible cases. Many compressible seal applications operate in low Mach number regimes where the present results can be directly applied, though further study could seek to quantify differences for high Mach number scenarios where compressibility effects become significant. The information presented here is an invaluable resource for engineers seeking to apply CFD methods for rotordynamic predictions for incompressible grooved seals, and will foster more widespread and accurate application of these methods.

Chapter 5

Conclusion

5.1 Summary

This dissertation presents a series of works seeking to advance the field of circumferentially grooved seal rotordynamic analysis and prediction. Focus was placed on the two main types of seal prediction methods currently employed, namely simplified bulk flow and full computational fluid dynamics (CFD) methods. The use of an effective film thickness allowed for improved shear stress modeling and reduced empiricism in bulk flow methods while a close examination of a set of full CFD results highlighted the critical influence of certain setup parameters, as summarized below.

In Chapter 2, a single groove CFD modeling approach is leveraged to define the effective film thickness, a more physical flow boundary that separates the recirculating flow in the groove from the jet flow in the clearance region. This novel film thickness, along with the derivative quantities of the groove pressure drop ratio and expanded area, are closely examined across a range of operating conditions to uncover the relationship between flow fields, film expansion, and steady state performance. An initial step to quantify an effective axial shear stress highlights regions of viscous pressure loss and recovery that are closely related to the local behavior of the film thickness, demonstrating the ability of the effective film thickness based analysis to capture and explain physical flow behavior. Two Reynolds number quantities, the ratio of circumferential to axial Reynolds number and total resultant Reynolds number, are identified as primary quantities capable of explaining changes in flow patterns and performance. Reductions in leakage for seal conditions with higher circumferential flow component are seen to be driven by increases in land shear stresses, where the influence of the groove at inducing pressure drop is lessened despite an increase in net flow expansion into the groove.

When varying the groove aspect ratio, net flow expansion is seen to be directly proportional to the groove pressure drop ratio and closely related to leakage. This highlighted flow expansion as a primary factor in the determination of leakage. Based on this physical modeling and analysis, a qualitative criterion to minimize leakage is suggested, namely to select a groove geometry that maximizes the expanded area while retaining a full recirculation region within the groove.

The work of Chapter 3 builds on the foundation of Chapter 2 by applying the single groove and effective film thickness modeling framework to an analysis of the shear stresses within the groove region for the first time. By utilizing effective film thickness based analysis, the additional bulk flow shear stress contributions within the groove region, both axially and circumferentially, can be isolated and directly quantified as a correction to a traditional Hirs shear stress definition. This contribution is named a form shear stress (FSS) due to its close relationship to the shape of the effective film thickness. Surface model fits are generated for the axial and circumferential FSS as functions of the same two previously identified Reynolds number quantities. The predictive capability of the FSS models is assessed through additional single groove and full seal CFD simulations. Error in predicted FSS less than 4.4% and 27% for the axial and circumferential directions, respectively, is observed for the single groove validation cases, an inspiring result given the complexity of the groove shear stress behavior meant to be captured by the FSS. Comparison of individual grooves from full seal CFD simulations indicates a limited ability of the model to account for developing flow conditions in grooves near the seal entrance. When the FSS models are implemented into a simplified bulk flow method, the need for a groove loss coefficient is eliminated, the physical behavior of the shear stresses within the groove is captured, and leakage predictions are within 10% of the experimentally reported values. This leakage prediction error compares well to the industry standard bulk flow prediction accuracy.

Chapter 4 addresses the use of the quasi-steady (QS) method for the prediction of rotordynamic coefficients for grooved seals, providing rigorous examination of prominent modeling features and their influence on prediction results from the standpoint of the flow physics. A local mesh refinement study revealed the need for a sufficiently refined grid within the groove region to fully resolve pressure and velocity gradients. The natural development of the flow predicted within the upstream region, specifically the development of circumferential velocity, is quantitatively confirmed to be vital to the overall rotordynamic predictions. Variations in upstream geometry resulted in up to 63% variation in predicted cross-coupled stiffness. Direct specification of preswirl, mass flow, and circumferential distribution of pressure at the seal inlet plane are all required should the upstream region be omitted from the model, though these are rarely all known a priori.

Potential pressure perturbation at the seal exit and within the downstream region causes up to 90% differences in direct stiffness for various downstream region configurations and boundary conditions. These significant variations in predicted coefficients for different upstream and downstream configurations highlight the need for experimentally accurate model geometries for all applicable subdomains. Changes in predicted leakage and direct stiffness for small variation in clearance due to rotor centrifugal growth indicate the need for this effect to be experimentally monitored and subsequently included in CFD models. The results also indicate that a slightly relaxed linearity threshold may be appropriate for seal conditions similar to those investigated here when considering the effect of modeling whirl amplitude.

The bulk flow analysis in Chapters 2 and 3 is the first work to define and quantify an effective film thickness for grooved seals and the first to utilize an effective film thickness framework to quantify and model the additional shear stress component, the FSS, within the groove region. The physical foundation on which the modeling efforts are built allows for flow field information to be inherently included in the analysis, ultimately leading to a reduction in empiricism within bulk flow methods. The effective film thickness and form shear stress modeling approach presented here thus provides an avenue for significant improvements in prediction accuracy for grooved seal bulk flow methods with the capability of being adapted to a wide variety of sealing scenarios, conditions, and geometries. The CFD analysis in Chapter 4 provides the first comprehensive study on the influence of local mesh refinement, upstream and downstream regions, rotor centrifugal growth, and modeling whirl amplitude on the rotordynamic coefficient prediction for an incompressible grooved seal when using the QS method. The results highlight the extreme care needed during model setup to realize the promised accuracy improvements over simplified bulk flow methods. By providing best practice guidelines based on predicted flow fields, this work furthers the use of full CFD methods for more regular rotordynamic prediction and serves as a valuable resource for engineers and rotordynamicists. This cumulative body of work concentrates on the understanding and accurate prediction of the flow physics within grooved annular seals, and ultimately, the influence of the flow physics on steady state and dynamic seal performance. The ideas presented herein advance the understanding and accuracy of the two major facets of seal performance prediction that will continue to be used in the development and design of modern seals and turbomachines.

5.2 Future Research

The investigations in this dissertation lead to several avenues for additional research in the areas of effective film thickness bulk flow modeling and full CFD method predictions. First, based on the final results of Chapter 3, a study on the implementation of the FSS models into full bulk flow perturbation methods for the prediction of rotordynamic coefficients is clearly warranted. With modifications to the analysis procedure used to quantify the FSS, updated models can be developed and deployed into other existing bulk flow frameworks so that their effect on rotordynamic coefficient prediction can be directly quantified. The governing equations in the present bulk flow demonstration allowed for a continually varying clearance, or film thickness, based on the use of the effective film thickness in the original quantification of the FSS. As such, a CFD-derived effective film thickness was employed in tandem with the FSS models to generate the subsequent leakage predictions. Many current industry bulk flow methods do not allow for a continually varying film thickness, so a direct implementation of the FSS models into these methods would be without explicit use of an effective film thickness. Further investigation would be necessary to determine if the implementation of these two features, the effective film thickness and the FSS, are independent in terms of their influence on rotordynamic prediction. The individual influence of each on predicted rotordynamic coefficients could also be quantified. The FSS model robustness could also be assessed through a sensitivity study examining how changes in FSS value, or more fundamentally in FSS model coefficients, impact leakage and rotordynamic coefficient predictions. Finally, a comparison of the influence of the FSS models on predictions from one, two, and three CV bulk flow methods could help elucidate the physical mechanisms behind why certain method types outperform others for certain seal scenarios.

A natural extension of this work would consider the effects of compressibility, as the simulations and analysis in this thesis assumed incompressible flow conditions and utilized water as the working fluid. For applications with working fluid and operating conditions generating Mach numbers below 0.3, where compressibility effects are generally considered negligible, the methodology and results of this dissertation are directly applicable. Because of the physical foundation of the effective film thickness, the modeling approach presented in Chapter 2 is adaptable and can be modified as necessary to account for compressible flow effects. Visual examination of numerical flow field results for gas labyrinth seals (e.g. Tsukuda et al. [48]) indicates that similar expansion and contraction behavior of the clearance region flow exists in compressible flow conditions, suggesting that the quantification of the effective film thickness would translate directly. Many

bulk flow methods for gas labyrinth seals replace the conservation of axial momentum equation with heavily empirical formulas (e.g. Neumann's equation) for direct prediction of the mass flow rate and pressure within each labyrinth cavity [3]. These equations are generally functions of a flow coefficient and kinetic energy carry over factor, which are each themselves empirical functions of geometry and operating conditions. Recent and continual efforts have sought to improve the modeling of these flow coefficients towards more accurate leakage predictions (e.g. Wu and San Andrés [68]). Similarly to the potential elimination of the groove loss coefficient in Chapter 3, an analysis of the relationship between the effective film thickness, the shear stresses within the labyrinth cavities, and these leakage equation coefficients could reveal avenues for reduced empiricism in the bulk flow leakage equations for gas labyrinth seals. When discussing full CFD methods, the modeling principles discussed in Chapter 4 apply equally to incompressible and compressible seal cases, namely to use as accurate geometry as possible for all flow domains and subdomains and to carefully examine all results from the standpoint of the flow physics. A compressible seal case study analogous to that of Chapter 4 would allow for a direct comparison of the effects of the various modeling parameters for different working fluid assumptions, including a discussion of the impact on fluid density where applicable.

The numerical work in Chapters 2 and 3 would benefit greatly from experimental investigations that could provide data to validate the shape and behavior of the effective film thickness and the FSS models. Experimental data for this purpose is scarce due to the difficult measurement conditions for annular seals, namely tight working clearances, the presence of curvature and rotational effects, and limited visual access to the fluid domain. Select studies have developed two-dimensional experimental models for flow visualization that neglect surface curvature and rotor rotation (e.g. Kuwamura et al. [69] and Szymański et al. [70]). This relies on the assumption that compressible seals with predominantly axial flow components have pressure distributions and carry over coefficients mostly independent of these effects. Additionally, the majority of these studies use an enlarged-scale geometric model to improve visual access. The present results suggest that the effective film thickness is definitively influenced by the ratio of circumferential to axial Reynolds number across the full range considered, possibly a result of the increased influence of inertial effects for the higher density working fluid. Preliminary simulations also indicated that a model with simple geometric scaling may not be representative of the original scale, even if Reynolds numbers are equivalent. Attaining velocimetry or other flow visualization data for an experimentally accurate grooved seal setup would likely require the design of a test rig for this specific purpose. The generation of a velocimetry or flow visualization database is a worthwhile pursuit as it would serve as a validation dataset for a wide array of bulk flow and

full CFD modeling and research efforts.

Appendix A

Computational Modeling Details

This dissertation employs two primary computational models to generate simulation data, a single groove axisymmetric model (Chapters 2 and 3) and a full seal eccentric rotor model (Chapter 4). While these models are described in brief in their respective chapters, additional detail for each is provided here regarding the model geometry creation, meshing, solver setup, and simulation execution. The primary objectives are to allow for reproducibility of the present methods and processes and to foster shared knowledge of the challenges and possible solutions associated with seal CFD modeling. The two models are addressed separately in the subsections below. The reader is referred to the ANSYS CFX documentation [42] for additional information on the use of specific settings and options within CFX that are discussed below.

A.1 Single Groove Axisymmetric CFD Model

A simplified single groove CFD model was leveraged in Chapters 2 and 3 to produce simulation data sets for further analysis. The assumption of fully developed flow was utilized to simulate a single groove of a seal with potentially many grooves. This assumption is only strictly valid for grooves sufficiently downstream of the seal inlet, where the circumferential velocity has fully developed and is no longer changing with axial location. The use of this model for predictions of grooves outside the fully developed regime is considered in Chapter 3 with limited success, though further investigation is required to fully describe the limitations of the single groove model in these instances. The axisymmetry of a circumferentially grooved annular seal in centered operating condition was leveraged to consider only a sector of the full seal circumference, further reducing the modeled fluid domain. This limits the use of the model to studies of steady state performance

since the development of fluid reaction forces is a result of circumferential variations in pressure and velocity. Despite these limitations, the results of Chapters 2 and 3 highlight the major benefits of using an efficient model of a reduced fluid domain for fundamental seal analysis. The length of the smooth section on either side of the groove was chosen as $L_l/2$, or half of the full seal land length. In this way, the single groove model represents sections that could directly link together to form the entire seal. The resulting model is depicted in the top of Fig. 2.2.

Creation of the model fluid domain was performed using ANSYS Design Modeler. An initial sketch in the axial-radial plane established the single groove length, depth, and clearance dimensions. A strictly two-dimensional solution is not allowed by the CFX solver, so a representative three-dimensional domain must be used. For an axisymmetric geometry, this equates to a small sector of the overall seal circumference. A revolution of the axial-radial sketch about the rotor center axis created the small sector model. A 0.05 degree sector was chosen to maintain a small computational domain and to allow for high quality elements with sufficiently refined grids, as described in the meshing discussion below. The fluid domain was sectioned into four bodies, as shown in Fig. A.1, to allow for targeted meshing and direct specification of the number of elements within certain sections and along certain dimensions. The four bodies were combined into a single part within Design Modeler to automatically share topology between bodies.

Meshing was performed within the ANSYS Meshing utility by directly specifying the desired number of divisions along various dimensions, including the land and groove section lengths. In this manner, the grid was almost completely determined by the user, maximizing control over grid generation. A combination of the Sweep Method and Edge Sizing controls were used to create the desired grid. Edge Sizing applies the desired division along the specified edge or edge set. The Sweep Method, as applied here, maps a grid through a body between initial and target faces. An example is a radial sweep between the rotor and stator land surface in the leftmost body of Fig. A.1. Both types of sizing control were made using a number of divisions, N, and a bias value, B, where the bias defines the difference in length between the first and last elements in the division. Geometric series relationships can transform between these metrics and the growth rate, α (see Fig. 4.3 for α definition), and first and last division lengths. These relationships allow for direct manipulation of first node spacing for turbulence modeling considerations and for close matching of grid spacing between bodies.

The final grid used for the base case single groove model contained 167,400 elements and is displayed in Fig. 2.2. Biasing within each domain body lead to higher numbers of elements near walls, with a heavy

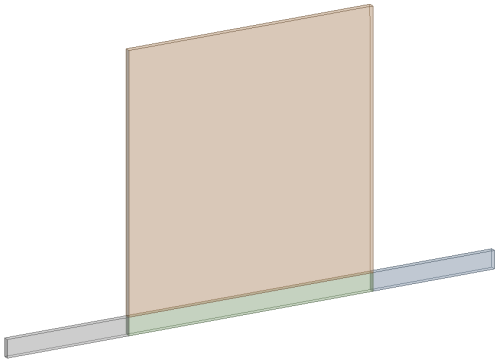

Figure A.1: Single groove CFD model fluid domain, showing the sectioning of the domain into multiple bodies for direct and efficient grid manipulation.

concentration of elements near the corners at the start and end of the groove. Element aspect ratio, defined as the ratio between the longest and shortest dimensions of an element, fell between 1 and 215 for the base case grid. It is suggested that element aspect ratios stay between 1 and 100, though empirical observations in CFD studies extend that range to around 1000 for some incompressible cases. The smallest axial and radial grid spacings were 2e-7 m and 3.4e-7 m, respectively, located at the corners of the groove. Element thickness (arc length) in the circumferential direction was approximately constant at 1.1e-5 m, though this increases slightly with radial location due to the curvature of the sector model. Note that a tradeoff between sector size and element aspect ratio exists when very small elements are utilized, as larger sectors stretch the circumferential dimension of all elements. Increasing the sector size while maintaining reasonable aspect ratios requires additional circumferential divisions, increasing the total number of elements and overall computation time. Three elements were utilized in the circumferential direction for the base grid in combination with the small sector size. The meshing process described here resulted in a grid of entirely hexahedral elements. Other meshing options within the ANSYS Meshing suite could result in different element types, though manual control may become more challenging when using other methods. The present hexahedral grid was thus chosen to maintain the highest level of user control and allow for closer examination of particular meshing parameters and specifications where appropriate.

Boundary condition specification for the single groove model is described in detail in Chapter 2 and depicted in Fig. 2.2. The rotor and stator surfaces were modeled as no slip adiabatic walls with the appropriate speed applied to the rotor through a rotating wall condition. The axial and circumferential interfaces, as shown in Fig. 2.2, were specified with axial and rotational periodicity conditions, respectively, with flux conservative

boundaries. An additional Pressure Change interface model was applied in the axial direction to enforce the desired single groove pressure drop. A domain interface target of 0.01 was also added within the Solver Control settings to ensure full convergence of the simulation with the inclusion of domain interfaces. The isothermal heat transfer option was employed for all cases, which is a common assumption in incompressible seal CFD studies where thermal effects are typically negligible. The effect of fluid temperature is accounted through the manually specified fluid density and viscosity.

The turbulence model selected was the Shear Stress Transport (SST) $k-\omega$ model, which blends the use of the $k-\omega$ model in the near wall regions and the $k-\epsilon$ model further from the walls. This approach leverages the near wall modeling benefits of the $k-\omega$ model and retains the robustness of the $k-\epsilon$ model. Seal analysis in the CFD literature generally applies the SST model, the isolated standard $k-\epsilon$ model, or a variant of either. The potential advantages of the SST model are realized when the placement of the first grid node is within the viscous sublayer. This is assessed through the y^+ value, a nondimensional measure of distance from the wall in relation to the flow boundary layer profile. A criteria of $y^+ < 5$ is generally considered acceptable for obtaining the near wall benefits of the SST turbulence model. Achieving this places tighter restrictions on the mesh and requires additional elements near the walls, ultimately increasing the overall computational time. A tradeoff thus exists between the potential accuracy benefits of the SST model and computational expense. The simplified single groove model domain is small enough that a well-refined grid would still be computationally efficient, and the SST model was chosen as a result. In addition, the SST model is known to perform better in regions of flow separation. Preliminary comparisons were made between predictions when using the SST and the standard $k-\epsilon$ turbulence models. Better predictions of the separated vena contracta region just after the sharp contraction at the groove to land transition point were observed in the SST model results, whereas the $k-\epsilon$ model often failed to predict this separation entirely and only captured a slight pressure variation. Since the analysis of Chapters 2 and 3 focus heavily on relating the effective film thickness to performance metrics, this further substantiated the use of the SST model to capture the additional detail in predicted flow fields. The final grid was chosen such that $y^+ < 5$ everywhere for all simulation cases.

ANSYS CFX utilizes a pseudo-transient solver approach for steady state simulations that uses a pseudo-timestep to march towards the steady state solution. This timestep is chosen by the user either through direct specification or through the specification of a multiplicative factor applied to an internally calculated timestep. The latter option is the default in ANSYS CFX and was used for the single groove model primarily

through the Auto Timescale option in the simulation control settings. The Auto Timescale option applies the calculated timestep uniformly to the entire fluid domain. When using the Auto Timescale setting, a Length Scale Option must also be specified to dictate the aggression level of the internally calculated timestep. The Conservative Length Scale Option was employed here without additional testing since the rate of convergence could be readily adjusted through the applied timescale factor. The user input Auto Timescale Factor ranged between approximately 0.01 and 100, depending on the specific case, the step in the convergence procedure, and whether a timescale ramping method was being used (described below). In many cases, a trial and error process was employed to select timescale factors that maximized convergence rate while ensuring convergence was still reached. Convergence difficulty was encountered for select cases with deeper grooves, which was hypothesized to be a result of larger differences in physical flow timescales within the groove region for deeper grooves compared to shallower ones. The use of a Local Timescale Factor helps mitigate this effect by applying different timescales across the fluid domain specific to each grid element and the flow within it. This Local Timescale Factor was utilized for the problematic deeper groove cases to achieve convergence. The details of this approach are discussed along with the full seal model in the following section.

As described in Chapter 2, mesh independence testing revealed that a typical convergence criteria of 1e-6 RMS was not sufficient to ensure the flow fields, particularly within the groove region, had fully converged. This resulted in a two-step convergence procedure being used, where an initial simulation was run to a convergence criteria of 1e-6 RMS and a second simulation to a criteria of 1e-10 RMS. Note that without further context, a convergence criteria of 1e-10 RMS would be considered extremely restrictive, as compared to CFD studies of seals in the literature. The separation of the two simulation steps allowed the timescale factor to be adjusted, if appropriate, to increase the rate of convergence in the second simulation and potentially limit the additional computational time required by the two-step procedure. Given the partially converged state of the initial simulation, the timescale factor was generally increased by one or two orders of magnitude for the second step simulation without issue. The convergence history for a sample case using the two-step procedure is given in Fig. A.2, where the increase in convergence rate (slope) of the decreasing residuals denotes the transition between steps one and two in the procedure. Note that the results at the conclusion of steps one and two correspond to the 1e-6 RMS and 1e-10 RMS plots lines, respectively, of Fig. 2.3. The use of a two-step convergence procedure and extremely tight convergence criteria underscore the need for close visual verification of CFD results, both for cases with convergence difficulties and for cases

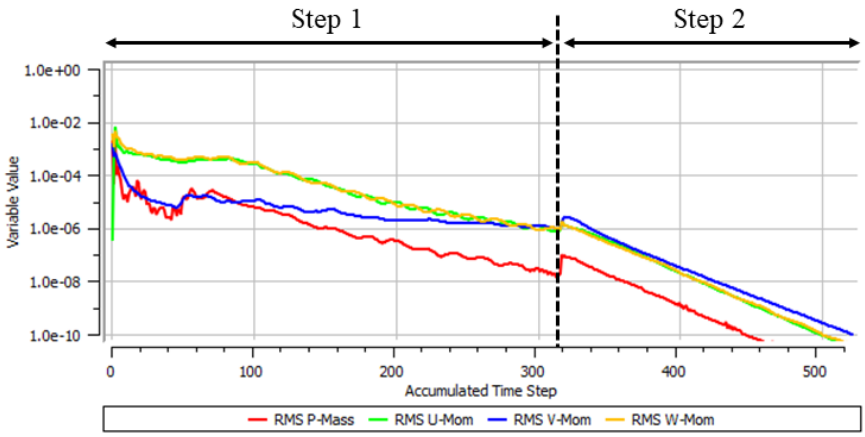

Figure A.2: Convergence history for a sample single groove case, showing the four RMS values (pressure and three velocity components) and the two steps of the convergence procedure. Note the increase in rate of convergence during step 2 due to the increase of the timescale factor.

that appear to be fully converged when standard criteria are met.

In addition, it was found that some cases with convergence issues could be assisted by beginning with a smaller timescale factor and gradually increasing it until the desired timescale factor was reached. This approach was termed a timescale ”ramping” method. Timescale ramping was applied through a User Function in CFX Pre, where the applied timescale factor was specified as a function of the iteration number. Timescale ramping was applied to the first step in the convergence procedure for select cases. In general, cases with high rotor speeds and higher circumferential flow components experienced more convergence difficulties and required initially lower timescale factors or the use of timescale ramping.

Simulations were generally run using three cores in parallel using the Intel MPI Local Parallel run mode, either on a local workstation or using Rivanna, the UVA High Performance Computing cluster. Simulation time and CPU hours used varied based on convergence behavior and the timescale factors employed. For example, a case using constant timescale factors of 1 and 50 for the first and second convergence steps, respectively, used a total of 1.37 CPU hours across both steps. A case using timescale factor ramping (increasing from 0.01 to 1) for step one and a constant timescale factor of 10 for step two used a total of 5.82 CPU hours across both steps. These cases should only be considered as representative examples since simulation time can vary with each case and with additional external factors, such as other processes on the workstation during a simulation. The trial and error timescale factor selection process employed for many cases also prevented systematic analysis of the resulting computational time.

A.2 Full Seal Eccentric CFD Model

A CFD model of a full seal with an eccentric rotor was employed in Chapter 4 to generate leakage and rotordynamic coefficient predictions for various model configurations. In order to analyze the fluid dynamic response due to off-center operating conditions or whirl motion of the rotor, the full seal circumference is now included in the model. The inclusion of various subdomains is also considered throughout Chapter 4, and the potential impact of these subdomains on the model setup, mesh generation, and simulation execution is discussed here. Modeling aspects similar to those presented for the single groove model above will be stated here without further discussion.

The base case model is shown in Fig. 4.2, where the full axial and circumferential extent of the seal are considered and the upstream region subdomain is included. To create the geometric model of the fluid domain, ANSYS Design Modeler is again used. A combination of axial extrusions and revolutions about the center annulus axis were used to generate the full fluid domain with a rotor eccentric along the +X axis. The fluid domain was again partitioned into multiple bodies to allow for direct manipulation of the subsequent grid. The different colors on the right side diagram of Fig. 4.2 denote the different bodies of the model in the axial-radial plane.

The grid generation procedure followed that of the single groove model, namely the use of Sweep Methods and Edge Sizing for direct specification of the number of division and bias factor applied to certain domain bodies. The grid for the base case model contained 5.86 million hexahedral elements and is depicted in Fig. A.3. In the axial-radial plane (top of Fig. A.3), the smallest axial and radial grid spacings were 9.2e-6 m and 4.7e-6 m, respectively. Note that these grid spacings are larger than their respective counterparts used in the single groove model because of a change in turbulence model, discussed below, and to reduce the total number of elements. Since the full seal circumference is included in the model, the number of circumferential elements becomes a critical parameter both in resolving the circumferential pressure variation and in determining the total number of elements in the model. Sensitivity of the stiffness coefficients to the number of circumferential elements was studied and presented in Fig. 4.4. The final grid contained 180 circumferential elements and approximate grid spacing (arc length) of 1.4e-3 m in the circumferential direction. This resulted in element aspect ratios between 2 and 285. The grid was again biased to have more elements near the walls, as depicted in Fig. A.3, though to a lesser degree than in the single groove model. The tradeoff between refinement in the axial-radial plane, element aspect ratio, and the total number

of elements is again observed. The base grid described here represented a satisfactory balance between computational feasibility, sensitivity, and accuracy.

Initial mesh sensitivity studies on an accompanying smooth seal model were used to assess the influence of local grid refinement near the seal inlet plane at a reduced computational cost due to the exclusion of the grid elements within the grooves. When returning to the grooved seal model, additional mesh sensitivity was conducted regarding local grid refinement within the groove region, as presented in Fig. 4.4. Finally, an overall uncertainty estimate for predicted leakage and each rotordynamic coefficient was generated for the selected base grid using the Grid Convergence Index (GCI) procedure. A brief description of the GCI procedure and the ensuing uncertainty results are presented in Chapter 4 and Fig. 4.2. Note that the overall sensitivity and numerical uncertainty in the full seal model is significantly higher than that of the single groove model. While mesh independence is still required, the criteria with which it is assessed may need to be relaxed as the model complexity increases. Reliable numerical uncertainty estimates should be supplied in addition to mesh independence results whenever possible to provide maximum context to the reader regarding the influence of the grid.

Turbulence closure for the full seal model was achieved using the standard $k - \epsilon$ model. Preliminary investigations indicated that a sufficiently refined grid capable of achieving $y^+ < 5$ everywhere while maintaining reasonable element aspect ratios would require a minimum of 90 million elements. Thus, the use of the SST model was considered a nonviable option for the parameter sweep investigation in Chapter 4. The wall function approach typically employed with the $k - \epsilon$ turbulence model generally requires $30 < y^+ < 300$, such that the first node is outside the buffer layer and within the log-law layer of the boundary layer profile. Scalable wall functions within ANSYS CFX, which are utilized for this model, allow for further grid refinement near walls by artificially placing all nodes outside the viscous sublayer. The y^+ values for the base grid fell between 6 and 75, well within the allowable range when using the Scalable wall function treatment in CFX. The use of both the SST and $k - \epsilon$ models in seal CFD analysis is well validated in the literature. Additional studies that directly quantify the difference in seal rotordynamic predictions when using each turbulence model on appropriately refined grids are strongly suggested.

Boundary condition specification followed that of the single groove model, except for total pressure inlet and static pressure outlet boundaries replacing the axial interface of the single groove model. The near stagnant flow in the upstream region allows for a total pressure to be specified at the inlet boundary, since the resulting static pressure implicit to the solution will be approximately equivalent to the total pressure, and

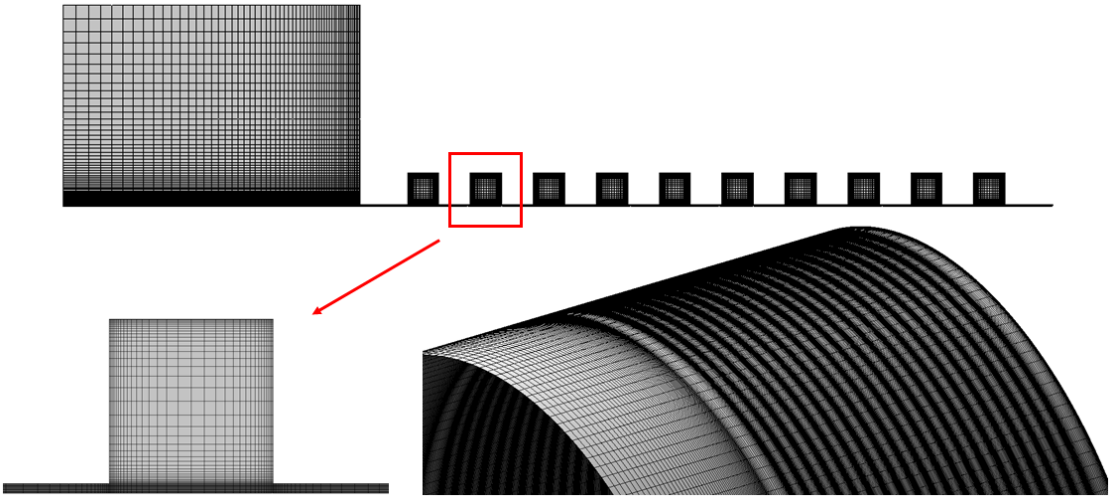

Figure A.3: Grid used for the base case setup of the full seal eccentric model. Top: axial-radial cross-section grid. Bottom left: axial-radial grid for a single groove. Bottom right: grid along the rotor surface.

ultimately to the desired seal pressure differential.

As suggested above, achieving full convergence with the full seal eccentric model was significantly more challenging than for the single groove model. Extensive testing indicated that the highest residuals were consistently found in the upstream region, likely due to the drastic differences in flow velocities and average element size between the upstream and seal regions. To mitigate some of this effect, a Local Timescale Factor was used to specify the pseudo-transient timestep. The Local Timescale Factor option in CFX applies a different timestep to each element based on the element size and the flow velocity within it. Local timescale factors between 0.001 and 75 were used to generate the results of Chapter 4. The timescale ramping methods described above were also found to assist with convergence and were applied in tandem with the Local Timescale Factor option. The CFX documentation discusses the need for the final few iterations to be run with a globally assigned timestep, such as the Auto Timescale Factor used in the single groove model. This is adopted here, where an initial simulation was run using a Local Timescale Factor to a target criteria of 1e-7 RMS and a second one for an additional 1000 iterations with a specified Auto Timescale Factor of 0.01. This two-step local-auto timescale method was applied to all cases considered in Chapter 4.

The primary quantities of interest predicted by the full seal model simulations were mass flow at the outlet boundary (leakage) and the forces on the rotor in the X (normal) and Y (tangential) directions (recall the rotor is positioned as eccentric in the +X direction). These forces directly lead to the determination of the rotordynamic coefficients. In addition to the residual convergence criteria of 1e-7 RMS, a visual examination

of the forces as a function of the iteration count was conducted for each case to assess overall simulation convergence. The forces were deemed to have converged when they no longer changed with additional iterations. Among the cases in Chapter 4, some initially reached the residual criteria without the forces fully converging and others never reached the convergence criteria despite having fully converged forces. This latter case occurred frequently and is depicted by the sample convergence history in Fig. A.4. The top plot shows the convergence of the RMS residuals, where two residual quantities do not reach the 1e-7 RMS criteria and instead plateau just above 1e-7 around iteration 1000. In the bottom plot, the forces are observed to have converged by iteration 1000 and stay converged through the remaining iterations. Such a simulation was deemed to have fully converged and the results were retained for subsequent analysis. The use of force convergence verification allows a simulation such as the one presented in Fig. A.4 to be considered valid while also ensuring additional iterations are applied if necessary, even when traditional convergence criteria have already been met. Given the difficulty in obtaining converged results for the various configurations in Chapter 4, this additional verification was critical to the generation of a full set of meaningful simulation results.

While achieving convergence was difficult for all cases with upstream or downstream regions, the difficulties associated with the axial inlet upstream and downstream region configurations were generally more challenging to overcome than for their radial configuration counterparts. It is hypothesized that this is a result of the boundary covering more physical area, where the potentially complex flow fields in the upstream and downstream regions could create significantly different flow conditions over various portions of the boundary. The successful use of the Local Timescale Factor to circumvent some convergence issues supports this hypothesis, though direct identification of the cause of convergence issues was rarely, if ever, achieved.

Simulations for the full seal model were exclusively run using the UVA High Performance Computing cluster Rivanna, generally using 20 cores in parallel. The author notes the practical limitations that exist for CFD users without easy or cost-effective access to high performance computing resources based on the high computational expense for single simulation cases. This underscores the importance of studies such as the work in Chapter 4 that enable informed decision-making early in the modeling process and help minimize redundancy. A comparison of the total number of model elements and total CPU hours required for a select set of cases is given in Table A.1. Note that only the CPU hours for the 0 whirl cases are shown, and it is assumed that the contributions of the additional whirl cases would align with the relative trends discussed

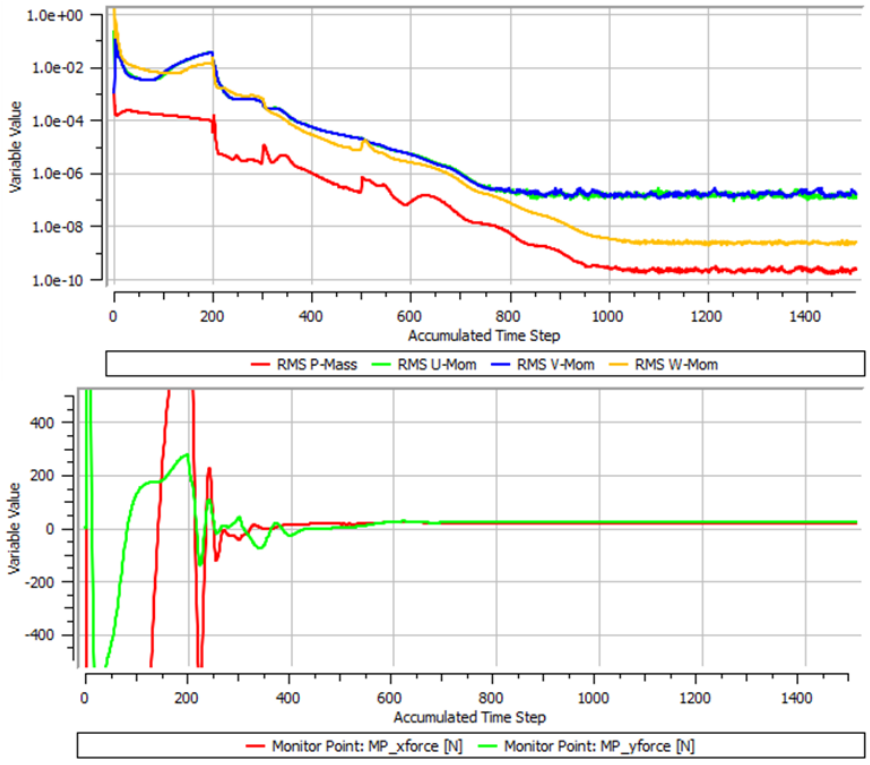

Figure A.4: Convergence history for a sample full seal case. Top: residual RMS convergence, showing values that do not reach the initial criteria of 1e-7. Bottom: convergence history of the two perpendicular force components, showing clear fully converged behavior despite not all residuals meeting the desired criteria.

here. The inclusion of additional subdomains, namely the upstream and downstream regions, increases the number of elements as expected. The total CPU hours are seen to generally increase with the number of elements and the addition of subdomains, though the correlation is not one to one. While the difference in CPU hours between the no upstream case (D) and the upstream region cases (A-C) is significant, the results in Chapter 4 confirm that an upstream region is critical to rotordynamic coefficient predictions unless significant flow information is known a priori. The difference in CPU hours between the upstream region only cases (A-C) and upstream and downstream region cases (G-H) is non-negligible, though the relative increase is fairly small. Based on the results of Chapter 4, the most accurate predictions are obtained when the most experimentally accurate model geometry is employed, including all relevant subdomains. The computational results presented here suggest that the increase in CPU hours required for additional subdomains is marginal compared to the potential improvements in prediction accuracy. This further substantiates the claim that all relevant subdomains should be included in the CFD model whenever possible.

Table A.1: Comparison of total number of elements and required CPU hours for simulations of different geometric configurations. Case labels correspond to the same cases as in Table 4.3. Representative cases with varying geometric configuration are considered here. The total CPU hours shown are for the 0 whirl cases only.

Case	Number of Elements (millions)	Total CPU Hours
Base case (A)	5.86	409.7
Radial inlet upstream (B)	5.88	346.9
Longer upstream (C)	6.23	343.9
No upstream, same BCs (D)	4.89	170.6
Radial outlet downstream (G)	6.85	502.5
Axial outlet downstream (H)	6.80	394.2

References

[1] KSB. Centrifugal pump lexicon - pump casing.

[2] San Andrés, L., 2009. Modern hydrodynamic lubrication theory, class notes - 12a: Annular pressure (damper) seals.

[3] Childs, 1993. *Turbomachinery Rotordynamics*. John Wiley & Sons, Inc., New York.

[4] Childs, D. W., Rodriguez, L. E., Cullotta, V., Al-Ghasem, A., and Graviss, M., 2006. "Rotordynamic-coefficients and static (equilibrium loci and leakage) characteristics for short, laminar-flow annular seals". *Journal of Tribology,* ***128***(2), pp. 378–387.

[5] Childs, D. W., 1983. "Finite-length solutions for rotordynamic coefficients of turbulent annular seals". *Journal of Lubrication Technology,* ***105***(3), pp. 437–444.

[6] Sultanian, B., 2018. *Gas Turbines: Internal Flow Systems Modeling*. Cambridge Aerospace Series. Cambridge University Press, ch. Labyrinth Seals, pp. 237–257.

[7] Black, H. F., 1969. "Effects of hydraulic forces in annular pressure seals on the vibrations of centrifugal pump rotors". *Journal of Mechanical Engineering Science,* ***11***(2), pp. 206–213.

[8] Yamada, Y., 1962. "Resistance of a flow through an annulus with an inner rotating cylinder". *Bulletin of JSME,* ***5***(18), pp. 302–310.

[9] Hirs, G. G., 1973. "A bulk-flow theory for turbulence in lubricant films". *Journal of Lubrication Technology,* ***95***(2), pp. 137–145.

[10] Kocur, J. A., Nicholas, J. C., and Lee, C. C., 2007. "Surveying tilting pad journal bearing and gas-labyrinth seal coefficients and their effect on rotor stability". In Proceedings of the Thirty-Sixth Turbomachinery Symposium, Texas A&M University Turbomachinery Laboratories, College Station, TX, Sept. 11-13, pp. 1–10.

[11] Migliorini, P. J., Untaroiu, A., Wood, H. G., and Allaire, P. E., 2012. "A computational fluid dynamics/bulk-flow hybrid method for determining rotordynamic coefficients of annular gas seals". *Journal of Tribology,* ***134***(2), p. 022202.

[12] San Andrés, L., Wu, T., Maeda, H., and Tomoki, O., 2018. "A computational fluid dynamics modified bulk flow analysis for circumferentially shallow grooved liquid seals". *Journal of Engineering for Gas Turbines and Power,* ***140***(1), p. 012504.

[13] Gibbons, N., Watson-Kassa, C., Goyne, C., and He, M., 2022. "Circumferentially grooved seal flow field analysis based on effective film thickness to improve bulk flow models". *Journal of Engineering for Gas Turbines and Power,* ***144***(11), p. 111021.

[14] Untaroiu, A., Hayrapetian, V., Untaroiu, C. D., Wood, H. G., Schiavello, B., and McGuire, J., 2013. "On the dynamic properties of pump liquid seals". *Journal of Fluids Engineering,* ***135***(5), p. 051104.

[15] Kim, S. H., and Ha, T. W., 2016. "Prediction of leakage and rotordynamic coefficients for the circumferential-groove-pump seal using CFD analysis". *Journal of Mechanical Science and Technology,* ***30***(5), pp. 2037–2043.

[16] Mortazavi, F., and Palazzolo, A., 2018. "Prediction of rotordynamic performance of smooth stator-grooved rotor liquid annular seals utilizing computational fluid dynamics". *Journal of Vibration and Acoustics,* ***140***(3), p. 031002.

[17] Wu, D., Jiang, X., Li, S., and Wang, L., 2016. "A new transient CFD method for determining the dynamic coefficients of liquid annular seals". *Journal of Mechanical Science and Technology,* ***30***(8), pp. 3477–3486.

[18] Li, Z., Fang, Z., and Li, J., 2020. "A comparison of static and rotordynamic characteristics for two types of liquid annular seals with parallelly grooved stator/rotor". *Journal of Engineering for Gas Turbines and Power,* ***142***(9), p. 091012.

[19] Gu, Q., Yang, J., Zhang, W., and Zhang, M., 2021. "An accelerating sweep frequency excitation method for the rotordynamic coefficients identification of annular gas seals based on computational fluid dynamics". *Journal of Engineering for Gas Turbines and Power,* ***143***(9), p. 091021.

[20] Nordmann, R., Dietzen, F. J., Janson, W., Frei, A., and Florjancic, S., 1986. Rotordynamic coefficients and leakage flow of parallel grooved seals and smooth seals. Tech. Rep. N87-22206, NASA.

[21] Iwatsubo, T., and Sheng, B. C., 1990. "Evaluation of dynamic charactersitics of parallel grooved seals by theory and experiment". In Proceedings of 3rd International Conference on Rotordynamics, Lyon, France, Sept. 10-12, pp. 313–318.

[22] Arghir, M., and Frêne, J., 2004. "A bulk-flow analysis of static and dynamic characteristics of eccentric circumferentially-grooved liquid annular seals". *Journal of Tribology,* ***126***(2), pp. 316–325.

[23] Florjancic, S., 1990. "Annular seals of high energy centrifugal pumps: A new theory and full scale measurement of rotordynamic coefficients and hydraulic friction factors coefficients and hydraulic friction factors". Ph.D. Dissertation, Swiss Federal Institute of Technology, Zurich, Switzerland.

[24] Marquette, O. R., and Childs, D. W., 1996. "An extended three-control-volume theory for circumferentially-grooved liquid seals". *Journal of Tribology,* ***118***, pp. 276–285.

[25] Wu, T., and San Andrés, L., 2019. "Pump grooved seals: A computational fluid dynamics approach to improve bulk-flow model predictions". *Journal of Engineering for Gas Turbines and Power,* ***141***(10), p. 101005.

[26] Rhode, D. L., Demko, J. A., Traegner, U. K., Morrison, G. L., and Sobolik, S. R., 1986. "Prediction of incompressible flow in labyrinth seals". *Journal of Fluids Engineering,* ***108***(1), pp. 19–25.

[27] Demko, J. A., Morrison, G. L., and Rhode, D. L., 1988. "The prediction and measurement of incompressible flow in a labyrinth seal". In AIAA 26th Aerospace Sciences Meeting, AIAA, Reno, NV, Jan. 11-14, pp. AIAA–88–0190 1–8.

[28] Morrison, G. L., Johnson, M. C., and Tatterson, G. B., 1991. "3-d laser anemometer measurements in a labyrinth seal". *Journal of Engineering for Gas Turbines and Power,* ***113***(1), pp. 119–125.

[29] Marquette, O. R., Childs, D. W., and Phillips, S. G., 1997. "Theory versus experiment for leakage and rotordynamic coefficients of circumferentially-grooved liquid annular seals with l/d of 0.45". In Proceedings of the ASME Fluids Engineering Division Summer Meeting, ASME, Vancouver, Canada, June 22-26, pp. FEDSM97–3333 1–16.

[30] Menter, F. R., 1994. "Two-equation eddy-viscosity turbulence models for engineering applications". *AIAA Journal,* ***32***(8), pp. 1598–1605.

[31] Morgan, N. R., Wood, H. G., and Untaroiu, A., 2016. "Design of experiments to investigate geometric effects on fluid leakage rate in a balance drum seal". *Journal of Engineering for Gas Turbines and Power,* ***138***(7), p. 072506.

[32] Wu, T., Andrés, L. S., and Lu, X., 2022. "Computational fluid dynamics analysis of the influence of gas content on the rotordynamic force coefficients for a circumferentially grooved annular seal for multiple phase pumps". *Journal of Tribology,* ***144***(11), p. 111803.

[33] Li, F., Zhai, L., Cui, B., Guo, J., and Chen, G., 2021. "Investigation of the dynamic characteristics of an eccentric annular seal on the basis of a transient CFD method with three whirl models". *Journal of Marine Science and Engineering,* ***9***(11), p. 1290.

[34] Wyssmann, H. R., Pham, T. C., and Jenny, R. J., 1984. "Prediction of stiffness and damping coefficients for centrifugal compressor labyrinth seals". *Journal of Engineering for Gas Turbines and Power,* ***106***(4), pp. 920–926.

[35] Han, L., Wang, Y., Liu, K., Ban, Z., Qin, B., Liu, H., and Dai, M., 2022. "Theoretical leakage equations towards liquid-phase flow in the straight-through labyrinth seal". *Journal of Tribology,* ***144***(3), p. 031802.

[36] Frêne, J., Arghir, M., and Constantinescu, V., 2006. "Combined thin-film and navier–stokes analysis in high reynolds number lubrication". *Tribology International,* ***39***(8), pp. 734–747.

[37] Wu, T., and San Andrés, L., 2019. "Gas labyrinth seals: On the effect of clearance and operating conditions on wall friction factors – a CFD investigation". *Tribology International,* ***131***, pp. 363–376.

[38] Yang, J., and San Andrés, L., 2019. "On the influence of the entrance section on the rotordynamic performance of a pump seal with uniform clearance: A sharp edge versus a round inlet". *Journal of Engineering for Gas Turbines and Power,* ***141***(3), p. 031029.

[39] Nagai, K., Kaneko, S., Taura, H., and Watanabe, Y., 2018. "Numerical and experimental analyses of static characteristics for liquid annular seals with helical grooves in seal stator". *Journal of Tribology,* ***140***(3), p. 032201.

[40] Constantinescu, V. N., and Galetuse, S., 1976. "Pressure drop due to inertia forces in step bearings". *Journal of Lubrication Technology,* ***98***(1), pp. 167–174.

[41] Iwatsubo, T., Sheng, B. C., and Ono, M., 1990. "Experiment of static and dynamic characteristics of spiral grooved seals". In Proceedings of the sixth workshop on rotordynamic instability problems in high-performance turbomachinery, NASA, Lewis Research Center, Washington, DC, pp. 223–233.

[42] ANSYS, Inc., 2021. CFX 2021 R1 Documentation.

[43] Untaroiu, A., Untaroiu, C. D., Wood, H. G., and Allaire, P. E., 2012. "Numerical modeling of fluid-induced rotordynamic forces in seals with large aspect ratios". *Journal of Engineering for Gas Turbines and Power,* ***135***(1), p. 012501.

[44] Pugachev, A. O., Kleinhans, U., and Gaszner, M., 2012. "Prediction of rotordynamic coefficients for short labyrinth gas seals using computational fluid dynamics". *Journal of Engineering for Gas Turbines and Power,* ***134***(6), p. 062501.

[45] Snyder, T., and Santos, I., 2021. "Rotordynamic force estimation of turbulent, annular seals using OpenFOAM®". *Journal of the Brazilian Society of Mechanical Sciences and Engineering,* ***43***, p. 119.

[46] Moore, J. J., 2003. "Three-dimensional CFD rotordynamic analysis of gas labyrinth seals". *Journal of Vibration and Acoustics,* ***125***(4), pp. 427–433.

[47] Wagner, N. G., Steff, K., Gausmann, R., and Schmidt, M., 2009. "Investigations on the dynamic coefficients of impeller eye labyrinth seals". In Proceedings of the Thirty-Eighth Turbomachinery Symposium, Texas A&M University Turbomachinery Laboratories, College Station, TX, Sept. 14-17, pp. 53–70.

[48] Tsukuda, T., Hirano, T., Watson, C., Morgan, N. R., Weaver, B. K., and Wood, H. G., 2018. "A numerical investigation of the effect of inlet preswirl ratio on rotordynamic characteristics of labyrinth seal". *Journal of Engineering for Gas Turbines and Power,* ***140***(8), p. 082506.

[49] Thorat, M. R., and Hardin, J. R., 2020. "Rotordynamic characteristics prediction for hole-pattern seals using computational fluid dynamics". *Journal of Engineering for Gas Turbines and Power,* ***142***(2), p. 021004.

[50] Waschka, W., Wittig, S., and Kim, S., 1992. "Influence of high rotational speeds on the heat transfer and discharge coefficients in labyrinth seals". *Journal of Turbomachinery,* ***114***(2), pp. 462–468.

[51] Subramanian, S., Sekhar, A., and Prasad, B., 2016. "Rotordynamic characteristics of rotating labyrinth gas turbine seal with centrifugal growth". *Tribology International,* ***97***, pp. 349–359.

[52] Subramanian, S., Sekhar, A., and Prasad, B., 2017. "Rotordynamic characterization of rotating labyrinth gas turbine seals with radial growth: Combined centrifugal and thermal effects". *International Journal of Mechanical Sciences,* ***123***, pp. 1–19.

[53] Athavale, M. M., Hendricks, R. C., and Steinetz, B. M., 1995. Numerical simulation of flow in a whirling annular seal and comparison with experiments. Tech. Rep. NASA-TM-106961, NASA.

[54] Zhang, K., Jiang, X., Li, S., Huang, B., Yang, S., Wu, P., and Wu, D., 2020. "Transient CFD simulation on dynamic characteristics of annular seal under large eccentricities and disturbances". *Energies,* ***13***(16), p. 4056.

[55] Ikemoto, A., Inoue, T., Sakamoto, K., and Uchiumi, M., 2018. "Nonlinear analysis of rotordynamic fluid forces in the annular plain seal by using extended perturbation analysis of the bulk-flow theory (influence of whirling amplitude in the case with concentric circular whirl)". *Journal of Tribology,* ***140***(4), p. 041708.

[56] Yamada, K., Ikemoto, A., Inoue, T., and Uchiumi, M., 2019. "Nonlinear analysis of rotordynamic fluid forces in the annular plain seal by using extended bulk-flow analysis: Influence of static eccentricity and whirling amplitude". *Journal of Engineering for Gas Turbines and Power,* ***141***(2), p. 021017.

[57] Xia, P., Liu, Z., Yu, X., and Zhao, J., 2018. "A transient bulk flow model with circular whirl motion for rotordynamic coefficients of annular seals". *Chinese Journal of Aeronautics,* ***31***(5), pp. 1085–1094.

[58] Launder, B. E., and Spalding, D. B., 1974. "The numerical computation of turbulent flows". *Computer Methods in Applied Mechanics and Engineering,* ***3***, pp. 269–289.

[59] Balasubramanian, R., Barrows, S., and Chen, J., 2008. "Investigation of shear-stress transport turbulence model for turbomachinery applications". In 46th AIAA Aerospace Sciences Meeting and Exhibit, AIAA, Reno, NV, Jan. 7-10, pp. AIAA2008–566 1–18.

[60] Cebeci, T., 2004. *Turbulence Models and Their Application*. Horizons Publishing, Long Beach, California.

[61] Marquette, O. R., Childs, D. W., and Andres, L. S., 1997. "Eccentricity effects on the rotordynamic coefficients of plain annular seals: Theory versus experiment". *Journal of Tribology,* ***119***(3), pp. 443–447.

[62] Roache, P. J., 1994. "Perspective: A method for uniform reporting of grid refinement studies". *Journal of Fluids Engineering,* ***116***(3), pp. 405–413.

[63] Pugachev, A. O., Ravikovich, Y. A., and Savin, L. A., 2015. "Flow structure in a short chamber of a labyrinth seal with a backward-facing step". *Computers & Fluids,* ***114***, pp. 39–47.

[64] Hirano, T., Guo, Z., and Kirk, R. G., 2005. "Application of computational fluid dynamics analysis for rotating machinery—part II: Labyrinth seal analysis". *Journal of Engineering for Gas Turbines and Power,* ***127***(4), pp. 820–826.

[65] Lomakin, A. A., 1958. "Calculation of the critical speed and the conditions to ensure dynamic stability of the rotors in high pressure hydraulic machines, taking account of the forces in the seals (in russian)". *Energomashinostroenie,* ***14***(4), pp. 1–5.

[66] Storteig, E., 2000. "Dynamic characteristics and leakage performance of liquid annular seals in centrifugal pumps". Ph.D. Dissertation, Norwegian University of Science and Technology, Trondheim, Norway.

[67] Young, W. C., and Budynas, R. G., 2002. *Roark's Formulas for Stress and Strain*. McGraw Hill, New York.

[68] Wu, T., and San Andrés, L., 2020. "Gas labyrinth seals: Improved prediction of leakage in gas labyrinth seals using an updated kinetic energy carry-over coefficient". *Journal of Engineering for Gas Turbines and Power,* ***142***(12), p. 121012.

[69] Kuwamura, Y., Matsumoto, K., Uehara, H., Ooyama, H., Tanaka, Y., and Nishimoto, S., 2014. "Experimental and numerical investigations on basic characteristics of high-performance abradable-aero hybrid seal". In Proceedings of the ASME Turbo Expo, Volume 1B: Marine; Microturbines, Turbochargers and Small Turbomachines; Steam Turbines, ASME, Dusseldorf, Germany, June 16-20, pp. GT2014–26812 1–14.

[70] Szymański, A., Wróblewski, W., Bochon, K., Majkut, M., Strozik, M., and Marugi, K., 2020. "Experimental validation of optimised straight-through labyrinth seals with various land structures". *International Journal of Heat and Mass Transfer,* ***158***, p. 119930.